CDF/doc/electron/cdfr/2899
Version 1.00
December 27, 1994

Determination of CDF Inner Detector Materials Using Conversion Electrons

A. B. Wicklund

Abstract

We use a sample of 210,000 photon conversion candidates from the Run 1a inclusive electron sample to "xray" the CDF detector. We rely on known materials, namely the CTC inner support can and the innermost CTC wires, to provide a baseline calibration. We compare these calibrations with the rates for Dalitz pair production and conversions in the SVX cable bundles and the Be-beampipe. The final result is that the amount of material, averaged over θ, Z(vertex), and CEM towers 0-8, integrated to the center of the CTC, is $0.0813 \pm 0.0039\ X_0$.

(1) Introduction

In situ analysis of the amount of material in the CDF detector is neded for accurate calibration of the barrel calorimeter. For the 1989 W-mass measurement, the effects of material were determined by analysis of the shape of the E/p spectrum for W $\rightarrow$ e ν decays .[1] This analysis has been repeated with better statistics in the run Ia W-mass measurement ,[2] and the results indicate that there is more material in the CDF inner detector than is accounted for in the CDF geometry data base. An independent analysis of the amount of material can be done using the observed conversion-electron rates in the inclusive electron sample, provided that "known" materials in CDF can be used as an absolute reference for calibration. This report summarizes an analysis of conversion rates, with the expectation that some of the methodology will prove useful in future CEM calibrations.

We assume that the *relative* rates for photon conversions in CDF are proportional to the amounts of material, expressed in X_0 . The equivalent radiator thickness for the inner support wall of the CTC is known, thanks to recent work by R. Kadel[3] and J. Hylen. Likewise, the amount of material in the CTC wires is well known.[4] Thus, in principle, we can determine the equivalent radiator traversed by electrons or photons, by comparing the conversion yield (as a function of X,Y,Z) with the yield in the CTC can or wires. Backgrounds from Dalitz pairs and random track overlaps ("fake conversions") must be subtracted, and possible variations in conversion-finding efficiency and electron trigger efficiency, as a function of the conversion point, need to be taken into account. We present results based on the CTC can and wire calibrations, and we compare these with observed Dalitz-decay rates and conversion rates in the beampipe and the SVX cables.

(2) **Event Selection**

We select inclusive electrons in the 6 and 9 GeV samples, restricted to towers 0-8, having a partner positron track candidate that satisfies

- abs(Sep) $\leq 0.5cm$
- abs($\Delta Cot(\theta)$) ≤ 0.15

where "Sep" is the $R\phi$ separation at the point of conversion (the point at which the two helices are parallel in ϕ), and $\Delta Cot(\theta)$ is the angle separation in the Z-view. This sample contains real conversions and fake conversion background. The cuts on the high-p_T trigger electron are described in the appendix. Ideally, the electron trigger efficiency drops out in the comparison of *relative* conversion rates, and so we choose the trigger-electron cuts to optimize the purity of the electron sample. The efficiency for finding the low-p_T partner positron can depend on (R,Z) of the conversion point. To minimize such dependence, we make no calorimetric (p_T -dependent) cuts on the partner positron, but we do use the calorimeter response to study fake backgrounds. In order to optimize position resolution, we require $p_T \leq$4 GeV/c for the partner. In addition, we require both the trigger and partner tracks to have hits in three or more axial and two or more stereo superlayers; this cut removes 2.6% of candidates, but the Sep and $\Delta Cot(\theta)$ distributions indicate that the failures are mostly background (a small fraction are conversions in the outer CTC SL's.)

In order to subtract fake backgrounds, we use signal and control regions in the Sep and $\Delta Cot(\theta)$ cuts. Figure 1 compares the $\Delta Cot(\theta)$ distributions (a) for candidates in which the partner positron is minimum ionizing in the CES (eg most likely a hadron), and (b) for the bulk sample of conversions. The lower histogram in fig.(1a) is obtained by further cutting on -.5$\leq$ Sep $\leq$-.3 cm; the antiselection on both CES and Sep gives a "pure background" sample. The lower histogram is normalized in the region abs($\Delta Cot(\theta)$)$\geq$.06. Figure 2 shows the analogous plots in the Sep variable. Note that Sep is a signed quantity: it is positive if the two helices are non-overlapping, negative if they overlap. Since the fakes consist mainly of two primary tracks coming from the beam spot, Sep $\leq$0 is the more likely configuration for fakes. For the bulk conversion sample (fig. 2b), Sep is symmetric about zero, except for small offsets caused by track reconstruction biases. Figures (3) and (4) show $\Delta Cot(\theta)$ and Sep distributions, this time comparing an unphysical region, -9$\leq$R$\leq$-3 cm, with the VTX/CTC-can region, 21$\leq$R$\leq$33 cm. Here, R is defined as the distance from (X,Y)=(0,0) to the conversion point; the sign is positive (negative) if the radius vector is parallel (antiparallel) to the parent photon direction. The background estimate for the negative-R region is taken from figs.(1) and (2), normalized to the region abs($\Delta Cot(\theta)$)$\geq$.06. Figures 3(c,d,e,f) and 4(c,d,e,f) show $\Delta Cot(\theta)$ and Sep distributions for intermediate slices in R. The conversion signals are very clean (except for the unphysical R$\leq$-3 region..) We adopt the cuts

- abs(Sep) $\leq$ 0.3 cm,
- abs($\Delta Cot(\theta)$)$\leq$ .03

to define the signal region. We subtract backgrounds using the region

- abs(Sep) $\leq$ 0.3 cm,
- .06 $\leq$ abs($\Delta Cot(\theta)$) $\leq$ .15

The background distribution in $\Delta Cot(\theta)$ is not quite flat; averaged over the partner positron p_T , we find that the background rate should be defined by:

- N(signal) = N(signal-region) - N(background-region) $\times 0.43 \pm .03$

We perform this subtraction on all quoted rates.

(3) Radial Distributions

Figure (5) shows the R distribution for 209,000 "signal" candidates; also shown in the lower trace is the background estimate. Evidently the conversions are very clean, and various material structures are visible. Figure (6) shows a blowup of the R distribution for fake background; again, in order to get a nearly "pure background" sample, we have required the partner to be minimum ionizing in the CES. The fake distribution is approximately symmetric about R=0, and cuts off at R=$\pm$30 cm, with a tail extending beyond R=+30. In the actual background subtraction, we do not cut on CES, and consequently tend to oversubtract (ie., there are real conversions in the background sample.) In the final analysis, we tried loosening the cuts used to define the signal and background regions, and verified that the conversion rates increased by a few percent, independent of R; for example, with abs(Sep)$\leq$.4 cm and abs($\Delta Cot(\theta)$)$\leq$.06, the background-subtracted rates increased by 6$\pm$1% everywhere.

The main objective of this study is to calibrate the conversion rate with a "known" radiator, for which the CTC can is a leading candidate. Richard Kadel's material assay[3] gives

- X_0 (CTC can) = 0.0126 $\pm$ 0.0006.

The problem, evident in fig.(5a), is achieving good enough R resolution to resolve the CTC can signal. An elegant solution to this problem was developed by Pat Lukens.[5] We follow his procedure here, albeit using different codes. We pull the e^+ and e^- helices to satisfy two constraints:

- (1) $Sep = 0$.
- (2) dϕ=0; dϕ is the angle between the photon momentum vector and the vector $\vec{R}$ pointing from the SVX beam spot to the conversion point.

To carry out these fits, we construct a nominal error matrix for the helix parameters for each track, taking into account estimated setting errors[6] and average multiple scattering, both inside the CTC and in the CTC inner can; we do not include multiple scattering at smaller R, so our resolution calculations are applicable only for conversions with $R \geq 27$ cm. We fit the track pairs, satisfying the constraints via Lagrange multipliers. Figure (7) shows the predicted resolutions for conversions in the CTC can, as functions of the partner positron p_T , for (a) no 2C fit, (b) 2C fit, (c) 2C fit with multiple scattering in the CTC can turned off, and (d) 2C fit with all multiple scattering turned off. In this simple analysis, multiple scattering dominates the resolution, and the 2C fit is predicted to yield about $\pm$4mm resolution on R over the 0-4 GeV/c p_T range. We remark that our error matrix formulation is wrong in principle, for the following reason: in the original fits used to determine helix parameters, multiple scattering is ignored. That means that, even if the error matrix defined above is the "true" error matrix, it is not the error matrix that describes helix parameters that we get from, eg., TRKS banks. In practice, we have verified that the results are not sensitive to the choice of error matrix, though the predicted resolutions certainly are.

Figure (8) shows the R distributions in the CTC can region before and after the 2C fits, (a) for $p_T \leq .5$ GeV/c partners, and (b) for $p_T \geq 2$ GeV/c partners. As indicated in fig.(7), the fits should not improve the R resolution at low p_T , and for $p_T \leq 0.5$ GeV/c the 2C fit is virtually identical to the unfitted R distribution. For the high p_T region, however, the 2C fit gives impressive improvement in resolution. Furthermore, the unfitted $p_T \geq 2$ GeV/c distribution is systematically shifted to smaller values of R. This implies that the errors are not Gaussian to begin with: the helices are systematically distorted. We speculate that this could be caused by hit sharing in the inner CTC superlayers, which would pull the e^+ and e^- tracks closer together, and thereby force both Sep and R to be shifted to negative values. Hit sharing would preferentially affect high-p_T tracks. Correlated with the shift in R, the negative shift in Sep is clearly seen in fig.(4c). Figure (9) shows the mean shift in Sep as a function of p_T , for e^+ and e^- triggers, in the VTX/CTC-can region. The shift is a strong function of p_T , and causes significant skewing in the Sep distribution.

It is important to understand whether the final, fitted resolution on R is "as good as it can be." We check this by comparing predicted and observed resolutions on R (after 2C fit) and on Sep and $d\phi$ (before 2C fit.) A Gaussian fit to the CTC can profile gives an average resolution of $\sigma(R) = 4.14$mm. (see below.) By comparison, the predicted resolution on R, averaged over all fitted conversions in the CTC can region, is $\sigma(R) = 3.53$mm. To compare the Sep resolution with the predictions for the same sample, we first empirically remove the systematic p_T -dependent offset in Sep (cf., fig.(9)); we then obtain an rms. width for the normalized variable, $Sep/\sigma(Sep)$, of

1.20. We obtain a similar result for the pointing constraint variable, $d\phi$, and conclude that the predicted resolutions are $\sim$16 % smaller than the observed resolutions on R, Sep, and $d\phi$. To show that the $d\phi$ distributions make sense, fig.(10) shows $d\phi$ with two choices for the primary vertex, namely the SVX beam spot (correct choice) and (X,Y=0,0) (wrong choice). The SVX beam spot improves the pointing resolution from 3.4 to 2.2 mrad. We conclude that our fits and projected errors are not unreasonable, and therefore that it is unlikely that we can achieve much further improvement in the R resolution.

Figure (11) shows the global R distribution after the 2C fits, with fake background shown as the lower trace. Structures are clearly visible corresponding to Dalitz pairs (R=0), and SVX,VTX, and CTC can conversions. Figure (12) shows a blowup of the SVX region, with arrows pointing to the average locations of the silicon planes. Structures such as the CTC can (and wires) and Dalitz pairs provide convenient calibrations because they are uniform in Z; for example, the CTC can material should go as $1/\sin(\theta)$, and the Dalitz decay probability should be independent of θ. On the other hand, the rest of the material has a complex dependence on Z and R, illustrated in fig.(13), which shows the Z dependence for selected slices in R. Dalitz pairs at the origin (13a) mirror the Zvertex distribution; the CTC can (13f) shows a smooth Z distribution, broader than for Dalitz pairs; the various SVX and VTX structures (13b,c,d,e) are strongly modulated in Z. Figure (14) shows a comparison of the distribution in $1/\sin(\theta)$ for Dalitz pairs and conversions in the can; the latter should be enhanced, relative to the Dalitz pairs, by a factor $1/\sin(\theta)$. The curve superimposed on the Dalitz points is obtained by weighting the can events by the factor, $\sin(\theta)$. The agreement is good and shows that the Z dependence in the can makes sense. Note that both the Dalitz pairs and can conversions provide a direct measurement of the initial angular distribution of the photons. This is needed to obtain the true value of X_0 , integrated over path, as a function of θ and Zvertex.

(4) **Calibration using CTC Can**

It is evident (fig. 8 or 11) that the separation between the CTC can and the outer material in the VTX is still not very crisp. This is primarily due to SVX cables that run between the outer VTX cage and the CTC can. Figure (15) shows the azimuthal distribution of the fitted conversion points for three slices in R in the VTX-CTC region. The azimuth is defined here as

$$\phi_{vtx} = \tan^{-1}(\text{ Y,X}) \ (\text{Z} \geq 0)$$
$$\phi_{vtx} = \tan^{-1}(\text{ Y,-X}) \ (\text{Z} \leq 0),$$

in order to simplify the distribution of materials in the east and west VTX halves.[5] The outer part of the VTX (24.5≤R≤26.8 cm) shows many structures in ϕ_{vtx} due to VTX and SVX cables, plumbing tubes, etc. The inner half of the CTC can (26.8≤R≤27.8

cm) shows the four SVX cable bundles plus the can materials. The outer half of the CTC can region (27.8≤R≤28.8 cm) shows only the material in the can itself. The structure in the latter region has a periodicity of 24, and is associated with the Phi-cracks between the wedges. The Phi-cracks, together with our fiducial cuts at the CES plane, cause a periodic shadowing of the high p_T trigger electron. On a finer scale, this structure is further modulated because the trigger e^+ and e^- are bent differently in the magnetic field. Note that if we try to look for any specific structure that is fixed in ϕ, like the SVX cables or the CTC wires, we need to correct for this Phi-crack modulation in trigger efficiency. For objects adjacent to the CTC can, such as the SVX cables or the innermost CTC wires, we use the azimuthal distribution in the outer half of the can to measure the efficiency empirically.

In order to improve the CTC can profiles, we antiselect on the ϕ regions corresponding to the SVX cables. Figure (16) shows the R distributions in the selected (a) and antiselected (b) regions in ϕ_{vtx}. Using the outer half of the CTC can, we determine that the cuts in ϕ_{vtx}, which subtend a total of 52 deg., retain 85.2±0.2% of the CTC can conversions. The conversion peak from the CTC can is quite clean after the ϕ_{vtx} selection.

To get the number of conversions in the CTC can itself, we use the ϕ_{vtx}-selected region, and we subtract residual backgrounds from the VTX/SVX-cables at small R and from the CTC wires and gas at large R. To get the shape of the VTX background at small R, we first subtract the R distribution in fig.(16a) from that in fig.(16b), scaled by geometric acceptance. This subtraction gives the R-distribution for the SVX cables alone in the ϕ_{vtx} antiselected sample; it is shown as the lower histogram in fig.(16b). Next, we assume that the same background *shape* describes any residual VTX/SVX-cable backgrounds that lie close to the CTC can in the ϕ_{vtx}-selected sample. That is, we assume that there can be materials very close to R=27.8 cm in the ϕ_{vtx}-selected sample, but the shape of the R distribution is dominated by resolution. Thus, we normalize the SVX-cable background function, shown in fig.(16b), to the number of events in the ϕ_{vtx}-selected sample in the region 26.5≤R≤26.8 cm. We do not attempt to describe the additional VTX-related backgrounds in R≤26.5 cm. This background estimate is shown as the lower histogram in fig.(16a). We model the large-R backgrounds from the CTC wires and gas using a monte carlo described below; this is included in the lower histogram in fig.(16a). Figure (17) shows the background-subtracted distribution for the ϕ_{vtx}-selected sample, with single-Gaussian fit superimposed. Since the large-R CTC wire and gas background is "known", the subtraction on the large-R side is absolute, and we use it to establish the rate for a small non-Gaussian tail. By symmetry, we fold this tail to obtain the number of CTC-can events at small R, R≤26.5 cm. Numerically, we estimate that the tails in $R \geq 30$ and $R \leq 26$ are a 0.5 % correction. We assign a 50 % uncertainty to the non-Gaussian tails and to the VTX/SVX-cable background, and obtain

$$\text{N(CTC-can)}=39904 \pm 850 \text{ events},$$

after correcting for the 85.2 % acceptance for the ϕ_{vtx} selection. This gives a calibration scale factor of

$$\mathrm{N(conversions)}/X_o = 10^4 \times [317 \pm 2(stat) \pm 8(bg) \pm 15(cal.)]$$

where the calibration error is the uncertainty on the CTC can thickness.[3]

(5) SVX Cable calibration

For completeness, we obtain a similar calibration using the SVX cables. In Lukens' analysis, these cables are modelled as four equivalent radiators of 0.0480 X_0 each subtending 7.713°.[5] To subtract backgrounds, we use the regions $90 - 105°, 270 - 285°$ in ϕ_{vtx}, for R≤26.8 cm, and we average over the non-cable regions for 26.8≤R≤27.8 cm. We assume 100 % uncertainty on the backgrounds for R≤26.8 cm. The calibration we obtain,

$$\mathrm{N(conversions)}/X_o = 10^4 \times [250 \pm 34],$$

appears to be lower than that for the CTC can, but the SVX cable signals are not as clean and we have no estimate for systematic uncertainty on the SVX-cable X_0 -thickness.

(6) CTC Wire calibration

The CTC wires provide a clean known radiator. We assume that each wire can be replaced by an equivalent thin layer, given by

$$t_{eff}(X_o) = [\frac{\pi {R_w}^2}{2\pi R}] \times N \times \frac{\rho}{X_o} \times [1 - \frac{dL}{L}] \tag{1}$$

where R_w is the wire radius, R is the radial location of the wire, X_o is the radiation length for the wire material, ρ is the wire density, dL/L is the elongation due to tensioning, and N is the periodicity for the SL ($N = 30$ for SL0.) We assume the following wire parameters for the stainless steel and gold-tungsten materials.[7]

- ρ(SS304) = 8.02 gm/cm^3
- X_o(SS304) = 13.92 gm/cm^3 (19 % Cr, 10% Ni, 71% Fe)
- Y(SS304) = 19.3 10^{11} $dyne/gm^2$
- dL/L(SS304) = 0.00088 (average, for nominal tensions.)
- ρ/X_o(SS304)= 0.5761 $/cm$
- ρ/X_o(Au-W) = 2.855 $/cm$

We construct a monte-carlo model to simulate the production of conversions in the CTC wires and gas. For $Ar - C_2H_6$ gas we assume

- $\rho/X_o(Ar - C_2H_6) = 0.0603\ 10^{-3}/cm$

The monte carlo generates conversions in the CTC can, gas and wires, along with fake backgrounds, assuming the nominal material calibrations for these sources, and nominal resolutions. The non-Gaussian tail observed in the CTC can conversions is modelled by adding a second Gaussian in R, comprising 6.4% of the sample, with resolution σ(R)=$\pm$1.2 cm.

To describe the geometry of the wire planes, we divide each of the 30 SL0 cells into four planes- one sense, one field, and two shaper planes- and impose 30-fold symmetry in ϕ. Each plane has 31 wire positions, each separated by 5mm along the plane; each plane is rotated by 45° with respect to an outward radial vector. The 16'th (central) wire position is located at R_o=34.54, 34.64, and 34.74 cm for the sense, shaper, and field planes respectively. The four planes are evenly spaced in ϕ, as defined by the azimuth of the 16'th wire position, with spacing $d\phi$=$2\pi/120$. We describe the geometry of each plane as follows:

1	2	3	4	5	6		16		26	27	28	29	30	31	-wire number
A	B	B	C	D	C	....	C	....	C	D	C	B	B	A	(Sense Plane)
A	B	B	E	E	E	....	E	....	E	E	E	B	B	A	(Field Plane)
A						....		....						A	(Shaper Plane)

where the wire types are as follows:

- A= 152.25μm radius SS304
- B= 127.00μm radius SS304
- C= 70.00μm radius SS304
- D= 20.00μm radius Au-W
- E= 89.00μm radius SS304

With this geometry, the innermost sense wire (type-D, position-5), is located at R=30.90 cm.

We expect the CTC wire conversions to occur in the four 45^o planes. We define an azimuthal angle, ψ, as the azimuth of the 16'th wire position in each of these planes. In general, any conversion occurring at location (R,ϕ) can be mapped onto a unique 45^o plane in the CTC, and can be assigned an azimuth, ψ, corresponding to the azimuth of the 16'th wire location in that plane. With good resolution, we expect to see four discrete peaks in ψ, from conversions in the wire planes, and a continuum from conversions in the gas. The angle ψ is given by

$$R_o/\sqrt{2} = R \times \sin\left[3\pi/4 - \psi + \phi\right] \tag{2}$$

where (R,ϕ) is the conversion point and R_o is the radial position of wire 16. Figure (18) shows the ψ distribution for conversions with $29.5 \leq R \leq 41.0$ cm. The two peaks correspond to the sense and field planes, and the valleys in between to the shaper planes. The solid histogram is the Monte Carlo prediction with nominal resolution on R and ϕ. The resolution in ψ is dominated by that in R. We choose four central values in ψ, equally spaced by $d\psi = 2\pi/120$, and cut on $abs[\psi - \psi_o] \leq .035$ for each of the four planes. Cutting on $d\psi$ is equivalent to cutting on a region in R for each value of ϕ. Figure (19) shows the distributions of the measured conversion azimuth, ϕ, relative to the center of each wire plane (ϕ=0 at R=R_o), for the different slices in ψ. The sense, field and shaper wires show up clearly with some backgrounds from fakes and gas conversions. The pileup at $\phi \leq -0.20$ reflects the tail of the CTC can (the events are cut on R$\geq$28 cm.) Figure (20) shows the same distributions from the monte carlo. The wire structures are similar in the monte carlo and the data, except that outer wires (positive ϕ) have fewer counts in the data than the monte carlo (see below.) With the $d\psi = 0.035$ cut, the four regions in ψ partially overlap. This is necessary to get high efficiency, given the ψ resolution, but it causes the tails of the sense/field wires to show up, shifted in ϕ, in the shaper planes, and vice-versa (such structures are present in the data in fig.19c,d., and in the monte carlo in fig. 20c,d.) Figures 21 and 22 show a blowup of the innermost wires in the data and monte carlo, respectively; the shaper plane distribution is presented as an average over both shaper planes. The first guard wire (wire-1, type-A) should give the same conversion probability in each plane. After background subtraction, we count

N=179$\pm$14 (first sense guard wire)

N=184$\pm$14 (first field guard wire)

N=156$\pm$10 (first shaper guard wire)

The shaper rate comes out 1.8 σ low compared with the sense/field planes.

We use the first three guard wires in the field and sense planes, and the first guard wires in the two shaper planes, to obtain the conversion calibration. We assume that these wires are so close to the CTC can that any R-dependence in the conversion finding efficiency should be common for the can and the wires. To compute the calibration, we need two efficiency corrections: (1) the effect of the 15^o wedge Phi-crack shadowing; (2) the efficiency of the cut on $d\psi$ used to define the four wire planes. To measure the wedge Phi-crack effect, we examine the overall ϕ distribution in the outer half of the CTC can ($28.0 \leq \phi \leq 28.6$ cm). Figure (23) shows this distribution, modulo($2\pi/30$), together with arrows that denote the effective locations of the inner guard wires. We count events within $\pm$3 mrad. of the wire locations, and compare these rates with those expected from the average rate for all events. Weighted by the relative thicknesses of the eight guard wires, we observe 3502 $\pm$ 59 events in the wire regions, where we expect 3526 $\pm$ 27. We conclude that the efficiency associated with the wedge Phi-crack shadowing is 99$\pm$2% in the calibration wire regions, compared with the CTC can average. This correction just reflects the alignment of the wires relative to the cracks; this "efficiency", a priori, could have been greater than unity if the calibration wires lined up differently with the wedges.

In order to determine the remaining efficiency corrections associated with the $d\psi$ cut and background subtractions, we counted wire conversions in the monte carlo, using the same algorithms as for the data.With the $\pm 0.035 d\psi$ cut, we count 1320$\pm$20 conversions out of 1441 generated in the calibration wires, and we estimate the efficiency to be 91.6$\pm$1.4 %. Relaxing the $d\psi$ cut to $abs(d\psi) \leq 0.040$, we obtain a higher efficiency, 1386$\pm$22/1441= 96.2$\pm$1.5 %. These monte carlo rates are normalized to the rates expected from the CTC can calibration. In the data, we count the following conversion rates:

Plane	Number	$X_o \times 10^{-3}$	Conversions/X_o $\times 10^4$
Sense	448$\pm$24	0.1586	282$\pm$15
Field	490$\pm$24	0.1586	309$\pm$15
Shaper	312$\pm$20	0.1340	233$\pm$15
Total	1250$\pm$40	0.4512	277$\pm$9

Corrected for efficiency, the conversion rate in the data is N=1378$\pm$52, very close to the monte carlo rate generated (N_{MC}=1441.) If we apply the looser cut,abs($d\psi$) $\leq$ 0.04, the conversion yield in the data increases from 1250$\pm$40 to 1306$\pm$41; corrected for the (higher) monte carlo efficiency, the corrected rate with loose $d\psi$ cuts is N=1371$\pm$52, again close to the generated monte carlo rate. We conclude that the data and monte carlo track each other with respect to cuts, and the efficiency corrected wire calibration is:

$$\text{N(conversions)}/X_o = 10^4 \times [305 \pm 12] \text{ (CTC-wires)}$$

This agrees well with the CTC can calibration.

As noted above, the monte carlo rates are higher than the data for the wires at larger R; this can be seen in the comparison of figs.(19) and (20), and in the comparison of monte carlo and data in fig.(18), which shows an average over SL0. Figure (24) shows a global comparison of the R distributions in data and monte carlo from the CTC can through SL2. Figure (25) shows a blowup of this distribution in SL0 alone. The histogram represents the monte carlo simulation; the solid smooth curve is the monte carlo without the non-Gaussian tail added to the R distribution. Note that we have not tried to model the non-Gaussian tails precisely because they do not affect the CTC can or wire calibrations significantly. Figure (26) shows the ratio of data to monte carlo versus R in SL0. This plot suggests that the conversion-finding efficiency drops almost linearly with R. The efficiency near the calibration wires (29.7$\leq$R$\leq$30.3 cm.) appears to be greater than unity; this is because we have not modelled the non-Gaussian tail from the CTC can perfectly. We conclude that, without a real model for the conversion-finding efficiency at large R, we cannot sensibly make use of the CTC wires beyond the inner guard region. Figure (27) shows the integral distribution of events with R$\geq$31 cm. The simulation (top histogram) predicts an approximately linear increase with R; the data (bottom histogram) plateau beyond R=60. As a test, we plot the same curve for all conversion candidates in the original sample, with no requirements on the number of SL's used in the CTC fit, and no cuts on Sep or $\Delta Cot(\theta)$, normalized to the events in 31 $\leq$ R $\leq$ 33 cm.; this is shown as the dashed curve in fig.(27). Both samples, the pure conversions and the uncut pair candidates, show the same plateau at the same level. We note that the p_T distribution for the trigger electrons does not show any strong R dependence, while the p_T distribution for the soft partners shows a gradual loss of efficiency at low p_T with increasing R. As discussed below, from the p_T spectral shapes, it is unlikely that the inefficiency at large R is significantly affected by offline track reconstruction losses.

The major source of inefficiency at large R is likely to be the CFT trigger loss, due to the absence of prompt and delayed CTC hits in SL0,2.. We postulate that the efficiency plateau in fig. 27 is a CFT effect, and it is clear that the plateau at R=60 cm matches smoothly with the linear R-dependence of the efficiency in SL0. In principle, we could test the CFT hypothesis using level-2 "volunteer" triggers that do not require a CFT track. In practice, the statistics for such an analysis are rather limited, and we have not done it.

As a further test of the simulation, we show a blowup of the R distribution around wire(1) for the four wire planes in fig.(28); we show the same comparison for wire(31) in fig.(29). Here we have defined wire(1,31) by cutting on $\pm$3 mrad. in ϕ. The wires are in the correct place, and the main discrepancy between simulation (histogram) and data (points) is the low counting rate for the data in wire(31).

(7) **Dalitz Pairs and Be-beampipe**

Figure (30) shows a blowup of the R distributions near the origin; there is a clear peak centered at R=0 coming from Dalitz decays. In order to improve the resolution, we use SVX-fitted tracks only in fig. (30a), while fig. (30b) shows the distribution for the full sample, using just CTC fits. In fig.(30) we use only the Sep=0 constraint and not the pointing constraint. Also, we define "R=0" using the SVX beam spots. Empirically, before the 1C fits, the Sep resolution is demonstrably much better for the SVX-fitted pairs ($\pm$.01)cm than for the CTC pairs ($\pm$.10 cm.). After the Sep=0 constraint, the R resolutions are in fact rather similar for figs. (30a) and (30b), although the SVX ladders (indicated by arrows) are better delineated in (30a). In fig.(30) the backgrounds are plotted as the lower traces. The Be-beampipe (0.00144$\pm$.00022 X_o at R=1.905) is visible as a tiny shoulder in (30a). To better illuminate the beampipe, fig. (30c) shows the R distributions for pairs with abs(Z)$\geq$35 cm. at the conversion point; with the SVX background thus eliminated, the beampipe structure is apparent. The R-distributions appear to extend to R<<0, with the tails only partially explained by the fake backgrounds (lower traces in fig.(30).) Figure (30d) shows the full sample from fig.(30b) after background subtraction, on a logarithmic scale. The data are not Gaussian distributed for R<-1 cm, but this is expected for Dalitz decays, due to the fact that the e^+e^- opening angle distribution is broader for Dalitz decays than for external conversions. The curve in fig.(30d) is from a Dalitz-decay monte carlo, described below. In the following analysis, we count Dalitz pairs by counting the subtracted rate in -6 $\leq$ R $\leq$ 0, and folding this about R=0.

If all conversions were due to π^0 and η production, then the equivalent external radiator would be given by:

$$t_{eq.}(X_o) = \frac{\pi^0, \eta \rightarrow \gamma e^+ e^-}{2(\pi^0, \eta \rightarrow \gamma\gamma)} \times \frac{9}{7} \times \frac{1}{\langle \sin^{-1}(\theta) \rangle}$$

The branching fraction is 0.0060, and the $\sin(\theta)$ factor is measured to be 0.850 (cf. fig.(14)), so the combined equivalent radiator is

$$t_{eq.}(X_o) = 0.00656$$

for Dalitz pairs. To be precise, this definition of $t_{eq.}$ is chosen so that we can make a direct comparison between the Dalitz rates and the CTC can rates; the $\sin(\theta)$ factor takes into account the difference in θ dependence between the Dalitz pairs and the CTC conversions, as in fig.(14). We count the Dalitz pairs (folded about R=0) using (a) all CTC-fitted Dalitz pairs, and (b) SVX-fitted pairs, corrected for SVX efficiency. To correct for SVX efficiency, we simply measure the fraction of fake conversions, in -6$\leq$R$\leq$0, that satisfy the SVX cuts; we assume these are really prompt pairs produced at the origin. The two methods yield

N(Dalitz)=13251 $\pm$ 240(stat) $\pm$370(BG) (SVX-only)
N(Dalitz)=12953 $\pm$ 228(stat) $\pm$640(BG) (All CTC tracks)

Using the SVX-fitted rate, we obtain

$$\text{N(conversions)}/X_o = 10^4 \times [202 \pm 7] \text{ (Dalitz)},$$

well below the calibration value obtained from the CTC can and wires.

We have evaluated several possible sources of this discrepancy, namely:

- Not all photons are accounted for by π^0, η decays; a substantial fraction can be attributed to QCD prompt photon production.
- Differences in the kinematics of Dalitz decay and Bethe-Heitler pair production could result in different efficiencies.
- Not all Dalitz decays occur at R=0; secondary K_s decays could result in an effective loss of real Dalitz pairs.
- There could be a systematic offset in the fitted values of R, so that the folding about R=0 underestimates the total rate.

First we address the QCD prompt photon production. We use the isolation distributions to separate this source of (isolated) e^+e^- pairs from the (nonisolated) π^0, η decays .[8] As shown in [8], we can use the sample of fake conversions to get the shape of the isolation distribution for non-isolated (π^0, η) pairs, and W electrons for isolated (QCD-prompt) pairs. From the observed isolation distribution for external conversions at large R, we estimate that 22% of the background-subtracted sample used in the present analysis is QCD-prompt. Thus, if the Dalitz pairs at R=0 came only from π^0, η decays, then the Dalitz-pair calibration given above would have to be increased by a factor 1/.78, and this would remove much of the discrepancy between Dalitz pairs and the CTC can. However, we expect that QCD-prompt photons undergo internal conversions to e^+e^- pairs at some level. The probability for internal conversion,C, is given in lowest order by [9]

$$C = \frac{2\alpha}{3\pi} \ln \frac{M_{max}}{2m_e}$$

Numerically, with our cuts on $\Delta Cot(\theta)$, C is expected to be rather close to the corresponding Dalitz decay probability ($C \simeq C_{Dalitz} = 0.0060$). To the extent that C is the same for all photons, including QCD-prompt and π^0, η decay, the Dalitz calibration given above would receive no correction.

Figure (31a) displays the separation of QCD-prompt photons. As an illustration, we select an enriched sample by requiring $p_T \geq 10GeV/c$ for the trigger electron and $E/p \leq 1.06$ (to suppress π^0 decays, where the second photon contributes to E/p.) The lower histogram is the isolation distribution for fake conversions, normalized to $E_{iso} \geq 8GeV$. The QCD prompt peak is evident at small E_{iso}. In fig.(31b), the histograms show the same comparison for the full conversion sample, for 6≤R≤30 cm. The points show the E_{iso} distribution for the R=0 Dalitz pair candidates, normalized in $E_{iso} \geq 8GeV$. The prompt photon excess at small E_{iso} is very nearly the same for the R=0 Dalitz pairs as for the large-R conversions. From the isolation distributions, comparing the background-subtracted e^+e^- pairs with the fake backgrounds, we estimate the following relative rates for QCD-prompt and non-prompt pairs:

$$\frac{prompt}{non-prompt} = 0.245 \pm .027 \text{ (R=0)}$$
$$\frac{prompt}{non-prompt} = 0.289 \pm .012 \text{ (6} \leq \text{ R} \leq \text{30)}$$

From the ratio of ratios,

$$\frac{\frac{prompt}{non-prompt}(R{=}0)}{\frac{prompt}{non-prompt}(R{\geq}6)} = 0.85 \pm 0.11,$$

the factor $C = 0.85 \times C_{Dalitz}$ could be interpreted as the "effective" internal conversion factor, including the efficiency of our cuts on Sep and $\Delta Cot(\theta)$. We will use this factor directly in the analysis of kinematical effects. The important point is that C is in fact comparable to C_{Dalitz}, as expected, and so QCD prompt photon production does not by itself explain the low rate observed for R=0 prompt pairs.

Next we address the kinematical difference between Bethe-Heitler pair production and Dalitz decay. First, the sharing of energy betwen the e^+ and e^- is more asymmetric for the Bethe-Heitler process than for Dalitz decays. This can modify the p_T spectra and affect the trigger efficiency. Second, the opening angle distribution is broader for Dalitz decay and internal conversions, because the photon is virtual for these processes, whereas the conversion photon is real and massless in the Bethe-Heitler process. This can affect the efficiency of the $\Delta Cot(\theta)$and Sep cuts. We consider these different effects in turn.

We follow Rossi's treatment for the Bethe-Heitler conversions ,[10] and leading-order QED for the Dalitz pairs .[11] We first generate a power law spectrum of π^0's that matches the observed conversion data. We let each π^0 decay into $\gamma\gamma$ and then into $e^+e^-\gamma$. We let the photons from the first process convert with 100% probability with the Bethe-Heitler sharing distribution; we follow the e^+, e^- from the second process, generated by QED, and compare the spectra of the high and low p_T electrons for both processes. Figure (32a) shows the high p_T spectra for the Bethe-Heitler (histogram) and Dalitz (points) processes, with a $p_T \geq 300$ MeV/c cut on the low p_T partner. Figure (32b) shows the same comparison for the low p_T spectra for the two processes, with a cut $p_T \geq 8$ GeV/c on the high p_T trigger electron. In the simulation we required $p_T(\pi^0)$ $\geq$8GeV/c, since we are mainly interested in high energy conversion photons. Aside from the fact that the Bethe-Heitler pairs show a slightly softer spectrum (as expected) for the low p_T partner (fig.(31b)), the spectral shapes for the two processes are quite similar. Comparing rates for trigger $p_T \geq 8$ GeV/c and partner $0.2 \leq p_T \leq 4$ GeV/c, we estimate that the Dalitz pairs should be enhanced, relative to Bethe-Heitler, by a factor 1.03 $\pm$ 0.01.

Next we consider the effects of the broader opening angle distribution for Dalitz pairs. We use the same simulation as above for π^0 and η production, and the same p_T cuts on trigger and partner electrons. We reconstruct Sep, $\Delta Cot(\theta)$and R for these events, and smear these by the nominal resolution observed for the large-R conversions in the data; with this smearing alone, the Bethe-Heitler pairs have 97.7 % efficiency in the monte carlo, higher than for the Dalitz pairs. Because of the broader opening angles, some of the Dalitz pairs end up in the "background" control sample, and would be subtracted from the signal according to our procedures for external conversions. We do this subtraction for monte carlo events, and then count the number of subtracted Dalitz pairs in the region -6$\leq$R$\leq$0. We obtain the following efficiencies for π^0 and η Dalitz decays, relative to the 97.7% efficiency for external conversions:

$$\varepsilon[\pi^0] = 0.963 \pm 0.002$$
$$\varepsilon[\eta] = 0.767 \pm 0.002$$

We have not done the full calculation for internal conversions from QCD prompt photon production. However, it is reasonable to assume that these conversions should have efficiencies more like the η decays, since the $M(e^+e^-)$ pair mass is not cut off by M_{π^0}. We assume that the mix of primary particles is given by 22% QCD prompt photons and 78 % π^0, η; we assume that the η fraction in the π^0, η sample is given by $F_\eta = \frac{\eta}{\pi^0+\eta} = 0.50 \pm 0.25$. Then, given the $\eta \to \gamma\gamma$ branching ratio of 0.388, the relative efficiency for the π^0, η subsample is 0.908 $\pm$ 0.040, for F_η = 0.50 $\pm$ 0.25. The overall efficiency for QCD-prompt photons, relative to the π^0, η Dalitz pairs, is given above as 0.85$\pm$0.11. Thus, the overall efficiency of the Dalitz pair plus QCD-internal conversion sample is given by:

$$\varepsilon[\mathrm{R{=}0\ pairs}]=[0.908 \pm 0.040] \times [0.78 + 0.22 \times (0.85 \pm 0.11)] = 0.878 \pm 0.038,$$

Note that the relative efficiency of the QCD-prompt sample, 0.85$\times$0.908=0.77, is indeed close to that of the η sample. Figure (30d) shows the monte carlo prediction for F_η=0.5, for the subtracted R-distribution. The non-Gaussian tails observed in the data are reasonably well described by the Dalitz monte carlo, and are due mainly to the tails in the η Dalitz pairs and the QCD-photon internal conversions.

Figure (32a) addresses the third concern listed above: the possibility that some Dalitz decays occur away from R=0, in particular because of the contributions from $K_s \to \pi^0\pi^0$. From dE/dx measurements on high p_T charged tracks in the electron sample, we can estimate the ratio of K^+:π^+ rates ($\sim$ 0.21), and hence the ratio of $K_s \to \pi^0\pi^0$: π^0 rates ($\sim$0.07). Thus, we generate K_s decays and allow the π^0 daughters from these decays to undergo Dalitz decays with 100% probability. The resulting rate is very low, mainly because the π^0's from K_s decay are softer on average than the primary π^0's; this rate is shown as the dashed curve in fig.(32a). Numerically, we estimate a net loss of approximately 1.7% of π^0 Dalitz decays from the R<0 region, due to K_s production, or 1.0 $\pm$ 0.5% loss of all Dalitz decays, given our assumptions on the mix of QCD-prompt, π^0 and η Dalitz decays.

Combining the kinematical and K_s corrections, we obtain a Dalitz calibration factor of:

$$\mathrm{N(conversions)}/X_o = 10^4 \times [226 \pm 8 \pm 10] \text{ (folded-Dalitz)},$$

where the systematic errors correspond to F_η=0.5$\pm$0.25. We will refer to this as the "folded-Dalitz" result.

As shown in the next section, R-dependent efficiency corrections account for about half of the 29% discrepancy between our Dalitz calibration and the CTC-can calibration. The remaining possible problem is the fact that we are forced to assume perfect symmetry about R=0 in counting the Dalitz pairs. A systematic shift of 2 mm. in R, for example, would change the Dalitz rates by approximately 20%. Thus, we consider an alternative method that avoids this problem. As shown in fig.(30c), with a cut on abs(Z_{vert}) > 35 cm., the combined Dalitz pair and beampipe conversions are rather cleanly isolated. The beampipe material is known, so we can obtain a combined calibration using events in the region -6<R<+6 cm, for abs(Z_{vert}) > 35 cm.

Figure (33) shows two R distributions (fake-subtracted) for this cut in Z_{vert}, in which the events are weighted by sin(θ). Figure(33a) is for a selection ϕ=199$\pm$17 deg., where the beampipe has an alloy seam and beampipe conversions are enhanced; the beampipe contribution appears to be Gaussian over a background. Figure (33b) shows the distribution with this seam region removed; the histogram is for all background subtracted events, and the points show the Dalitz subtracted events, where the Dalitz subtraction is accomplished by folding the R<0 events. We assume that the events with abs(R)<3 cm are a mix of Dalitz and beampipe conversions, and that the events with R<-3 cm are the Dalitz tail. After Dalitz subtraction, there is a significant excess of events in R>+3 cm., which we attribute to residual material in the detector. We ignore the R>3 cm. events and fold the R<-3 cm region to count the events in +3<R<+6 cm. Since we are not folding about R=0, we are minimally sensitive to systematic shifts in R. Using this ansatz, we count the Dalitz and beampipe events in -6<R< 6 cm., cut on Z_{vert} and ϕ. We measure the efficiency of the Z_{vert} and ϕ cuts to be 0.1304±.0029, using the event rates in the outer half of the CTC can (28<R<30 cm.), weighted by sin(θ). The combined equivalent radiator for the Dalitz plus beampipe events is given by:

$$t_{eq}[\text{Dalitz+beampipe}]=0.00656 \times 0.896 + 0.00144 = 0.00731 \pm .00022 X_o,$$

where the factor 0.896 is the product of the Dalitz pair efficiency factors given above. We count 2246±62 weighted events in the Dalitz plus beampipe sample, and obtain the calibration:

$$N/X_o = 10^4 \times [277 \pm 16] = \frac{[2246 \pm 62]}{[0.00731 \times 0.1304 \times 0.850]} \text{ (Dalitz+ beampipe)}$$

We will refer to this as the "Dalitz pair plus beampipe" calibration. Although it is difficult to separate cleanly the beampipe from the Dalitz events in fig(33b), we estimate the beampipe contribution to be 499±101 events, or 22 ±4 % of the beampipe plus Dalitz sample. Based on the relative equivalent radiators, we would expect this fraction to be 19.7±2.9%. If we had simply counted Dalitz rates in R<0 and folded about R=0, then the Dalitz rate estimate in this sample would have been lower by 13%; this corresponds to a systematic shift of about +1 mm. in the R distribution.

(8) **Efficiency Corrections**

As noted in the CTC-wire calibration analysis, there is a demonstrable falloff in the conversion-finding efficiency for R≥31 cm., most likely due to the CFT trigger requirement. In this section we examine the evidence for efficiency variations with R over the inner detector region, 0≤R ≤30 cm. We emphasize that we do not need to determine the *absolute* conversion-finding efficiency, only the *relative* efficiency variations with R.

We expect that relative variations of efficiency with R should be reflected in variations of the observed momentum spectra for both trigger electrons and low-p_T partners. For example, the following effects could in principle lead to variations of efficiency and p_T spectra with R:

- Track reconstruction efficiency for low p_T tracks could decrease with R because of the increase in the impact parameter.

- Track reconstruction efficiency for low p_T tracks could increase with R, because the track helix can intersect more CTC SL's.

- Trigger efficiency could increase with R, because at large R there is an enhanced probability for getting both particles in the same CEM wedge, and hence getting higher E_T from the same parent photon.

- Trigger efficiency (including level-3 selection) could decrease with R (larger E/p for events with both tracks in same wedge, lower CFT efficiency due to larger impact parameter, etc.)

These are examples of possible effects, not an exhaustive list.

In order to separate trigger efficiency and track reconstruction effects, we first classify the conversions as "N=1" (partner positron in separate wedge) and "N=2" (both trigger and partner particles in same wedge.) As an example, we "normalize" to the p_T distributions observed in the SVX, 2≤R≤7 cm., and compare that with the distributions at other values of R, for example 27 ≤ R ≤ 29 cm. (CTC can.) In the "R=R_{SVX}" sample, we start with a certain mix of N=1 and N=2 conversions. We ask, if the same mix of conversions were produced at R=R_{CTC}, what should the N=1 and N=2 spectra look like in the "R=R_{CTC}" sample? To answer this, we take each identified conversion in the "R=R_{SVX}" sample, and move its conversion vertex to R=R_{CTC}; we then propagate the tracks to the CEM and classify the propagated conversion as N=1 or N=2. The following outcomes are possible:

- (1) N=1 at R=R_{SVX} remains N=1 after propagation to R=R_{CTC},= $N_{11}(R_{svx}, R_{ctc})$

- (2) N=1 at R=R_{SVX} becomes N=2 after propagation to R=R_{CTC}, = $N_{12}(R_{svx}, R_{ctc})$

- (3) N=2 at R=R_{SVX} remains N=2 after propagation to R=R_{CTC}, = $N_{22}(R_{svx}, R_{ctc})$.

Note that, with $R_{ctc} \geq R_{svx}$, the fourth possibility is excluded, ie. $N_{21}(R_{svx}, R_{ctc}) = 0$. We can now compare the observed N=1, N=2 rates in the CTC can, $N_{1,2}(R_{ctc})$, with the expected rates, based on extrapolation of the observed distributions, $N_{1,2}(R_{svx})$:

$$N_1(R_{ctc}) = K \times N_{11}(R_{svx}, R_{ctc})$$
$$N_2(R_{ctc}) = K \times [N_{22}(R_{svx}, R_{ctc}) + \alpha N_{12}(R_{svx}, R_{ctc})]$$

where K should be the ratio of material thicknesses at the two R values, and α is a correction for the difference in trigger efficiency for the N=1 and N=2 cases. In selecting events for comparison in the different R-regions, we must impose the abs(X)<21.5 cm. cut for the propagated conversions. In particular, we must impose this cut in a reciprocal fashion: an event produced at R_{svx} must satisfy the cut after propagation to R_{ctc}; and an event produced at R_{ctc}, used for rate comparison, must satisfy the cut after propagation back to R_{svx}. We have used monte carlo to verify that the comparison of distributions is valid after making these reciprocal cuts. In principle, α will be a function of the momenta of both trigger and partner electrons. If the tracking efficiency is independent of R, then the momentum spectra at R=R_{ctc} should be predicted by the above equations, with a single scaling factor, K. We choose the overall scale factor, K, by normalizing the observed N=1 rates with partner $p_T \geq 0.5$ GeV/c Figure (34) shows a comparison of the observed trigger p_T spectra for the trigger electrons at R=R_{ctc} (solid points), for N=2 (34a) and N=1 (34b), together with the predicted rates based on propagation from R=R_{svx} (histograms.) The bottom histogram in fig. (34a) shows the contribution to the predicted N=2 rates from the $N_{12}(R_{svx}, R_{ctc})$ term above. We see that the observed and predicted N=1 rates agree very well, while the observed N=2 rates are higher than the predicted rates, for trigger p_T below 10 GeV/c. This is because the trigger efficiency is higher for the N=2 pairs, and so the predicted contribution from the $N_{12}(R_{svx}, R_{ctc})$ rate must be corrected by a large α parameter. Figure(35) shows the N=1 partner p_T spectra for trigger p_T values above and below 10 GeV/c, again comparing observed rates at R=R_{ctc} (solid points) with predicted rates (histograms). Again, the agreement is nearly perfect for the N=1 pairs. Figure 36 shows the same comparison for N=2 pairs; here the bottom plot corresponds to that in fig. (34), ie. the contribution from the $N_{12}(R_{svx}, R_{ctc})$ rate alone. For trigger p_T greater than 10 GeV/c (36a), the agreement is fairly good, but for trigger p_T below 10 GeV/c (36b), the observed rates are much higher than predicted. Figure (37) shows a comparison of N=2 rates, this time with the $N_{22}(R_{svx}, R_{ctc})$ contribution subtracted from the observed rates; the points are the subtracted N=2 rates, and the histograms are the predicted rates from the $N_{12}(R_{svx}, R_{ctc})$ term alone. This comparison shows that the shapes of these spectra are rather similar, but a large α correction is needed for trigger p_T <10 GeV/c .

We conclude that the trigger and partner p_T spectra are identical for the N=1 events, taking into account the effects of propagating from R=R_{svx} to R=R_{ctc}. However, the trigger efficiency for N=2 pairs is much higher than for N=1 pairs, especially at low values of the trigger p_T ; consequently, because the N=2 configuration is geometrically favored at large R values, the observed N=2 rates at R=R_{ctc} are substantially higher than what we would get from a simple extrapolation from R=R_{svx}. We have examined these distributions separately for the level-2 6 GeV and 9 GeV triggers, and the conclusions are the same as stated here.

For completeness, we have carried out the same spectral comparisons for different slices in R. In particular, figs. 38 and 39 show the trigger p_T and partner p_T comparisons, respectively, in the slice $42 \leq$ R ≤ 51 cm, where the overall reconstruction efficiency is low by a factor of two (cf. fig. 24.) We see evidence for a cutoff in the N=1 partner p_T spectra (fig. 39a,b) at around 0.6 GeV/c in the observed rates, presumably due to the fact that the low p_T tracks have large impact parameter at large R. However, this is a small effect, and we see that the spectral shapes are otherwise in fairly good agreement with the predicted shapes, modulo the N=2 trigger bias effect. Thus, it seems unlikely that the reconstruction efficiency has a major impact on the conversion rates, even at very large R values. The loss of efficiency for R $\geq$ 30 cm. is probably due mainly to the CFT requirement, since it is largely independent of the trigger or partner p_T values.

Finally, we define the relative efficiency as a function of R by normalizing to the N=1 rates with partner $p_T \geq$0.5 GeV/c; the normalization is given by the ratio of observed N=1 rates to predicted N=1 rates, using the R=R_{svx} slice propagated to the other R-slices. The efficiency for R=R_i in slice i, relative to R=R_{svx} is then defined as the total observed rate divided by the expected rate,given the K-factor for slice i. Figure 40 shows this relative efficiency as a function of R. We assume the efficiency is a smooth function of R. For R$\geq$ 18 cm., we assume the linear variation indicated by the dashed curve in fig. 40; for external conversions with R $\leq$ 18 cm., we assume a relative efficiency of unity (solid line in fig. 40.) For Dalitz pairs (defined by 2 $\times$ the R $\leq$0 rate), we assume a relative efficiency of 0.965 $\pm$ .027.

(9) Determination of Total Radiator Thickness

We count the total number of conversions in the region 0$\leq$R$\leq$31 cm., after subtraction of Dalitz pairs and fake backgrounds. We correct the rates according to the relative efficiency as a function of R, as determined in the previous section; we normalize so that the relative efficiency is unity at the CTC can radius. We form the ratio of this integrated conversion rate to the CTC-can rate, and express the total material thickness as:

$$X_t = \frac{N_{tot}}{N_{ctc}} X_{ctc} = \frac{\int n(\theta) X(\theta) d\theta}{\int n(\theta) \frac{1}{\sin(\theta)} X_{ctc} d\theta} \times X_{ctc} \times A(\theta),$$

where X_{ctc}=0.0126, $X(\theta)$ is the total thickness,and $A(\theta)$ is a correction for attenuation; A is given approximately by

$$A(\theta) = \frac{\frac{9}{7}[1-\exp(-\frac{7}{9}X_{tot})]}{X_{ctc}\exp(-\frac{7}{9}[X_{tot}-X_{ctc}/2])}$$

Averaged over θ, the attenuation correction factor is $A = 1.023$. With this definition, if all the material thickness varied as $X(\theta) = X_0 \times \frac{1}{\sin(\theta)}$, then X_t would be the material thickness measured perpendicular to the beam line, ie., analogous to X_{ctc}=0.0126. For comparison with the material assay from the $W \to e\nu$ E/p analysis, we have

$$X_t = \frac{X_W}{\langle \frac{1}{\sin(\theta)} \rangle},$$

where X_W is the total angle averaged material thickness seen by the W electrons. Figure (41) shows the variation of X_t with $\sin(\theta)$ for two cuts on Z_{vert}, abs(Z) $\leq$ 60 cm (41a) and abs(Z) $\leq$ 25 cm (41b). We compare $\cot(\theta) \geq 0$ (circles) and $\cot(\theta) \leq 0$

(diamonds). We see that the Z_{vert} cuts make rather little difference (numerically, the cut Z $\leq$ 25 cm. increases X_t by a factor 1.0225 $\pm$.0087, averaged over angles.) Also, there is very little residual dependence on $\sin(\theta)$ for this definition of X_t. The values shown in fig. 41 are for external conversions for R $\leq$ 31 cm., and the errors are statistical only. Averaged over angles, with abs(Z) $\leq$60 cm, we have

$$X_t = 0.06024 \pm 0.00043 \text{ (stat)} \pm 0.00325 \text{ (calib.)}$$
$$X_W(\text{pred}) = 0.07087 \pm 0.00051 \text{ (stat)} \pm 0.00382 \text{ (calib.)}$$

If we add half of the CTC material to X_W(pred), weighted by the $\frac{1}{\sin(\theta)}$ factor, we obtain

$$X_W \text{ (pred)} = 0.0813 \pm 0.0039,$$

which may be compared with the value X_W(meas)=0.089 $\pm$ 0.009 reported in the W-mass E/p analysis, and also the value X_W= 0.064 estimated from the CDF geometry database [2] .

Figure (42) shows a summary of the material thicknesses obtained for abs(Z)$\leq$ 60 cm., angle averaged, for the various calibrations described above (CTC can and wires, folded-Dalitz pairs, Dalitz pairs plus beampipe, SVX cables, and E/p method.) For the two Dalitz rates, we have added the uncertainty in the relative acceptance to the error bar and assumed F_η=0.5 $\pm$ 0.25. The points are shown as transverse thicknesses, identified as X_t above; to convert to total path length (eg. X_W values), these have to be multiplied by the factor 1/0.850. To include half the CTC material, the X_W values must be increased by 0.0104, the X_t values by 0.00884. Note that every estimate gives significantly more material than predicted by the CDF data base. The SVX cable and folded-Dalitz pair calibrations predict even more material than the CTC can or wire calibrations.

In conclusion, we have presented estimates of the material thickness in the inner CDF detector based on conversion rates. These estimates exceed corresponding values from the CDF data base, but are consistent, within errors, with the E/p calibration used for the CDF W-mass analysis. We show that it is necessary to take into account small R-dependent corrections to the conversion-finding efficiency. We find that the CTC can and wire rates are in good agreement with each other, and with the combined Dalitz pair plus beampipe rates measured with Z_{vert} >35 cm. We observe that the total Dalitz pair rate, obtained by folding about R=0, is systematically low (consistent with greater detector thickness than predicted by the CTC can calibration), but we show that this could be explained by a small systematic shift in the fitted values of R.

Acknowledgments

We have already called attention to the work done by R. Kadel and J. Hylen on the CTC-wall thickness, and by P. Lukens on fitting procedures. The idea of calibrating on CTC wires was suggested by H. Keutelian. Many others have looked into the CDF material calibration, or have offerred useful suggestions, including D. Saltzberg, A.

Goshaw, L. Nodulman, K. Ragan, Y.K. Kim, M. Binkley, P. Berge, and A. Mukherjee. H. Carter, B. Flaugher, and J. Skarha provided specifications on the beampipe. Finally, a parallel analysis has been carried out by W. Ashmanskas, which improves on some of the results presented in this paper.

Appendix: trigger electron cuts

The following cuts were applied to the trigger electron samples, based on "BPAD" datasets with 615 tracking:

- abs(Z_{vert}) $\leq$ 60 cm.
- abs($Z_{el} - Z_{vert}$) $\leq$ 6 cm.
- abs(X_{ces}) $\leq$ 21.5 cm.
- 9$\leq$ Z_{ces} $\leq$ 217.4 cm.
- $N_{tower} \leq 8$
- $\chi^2 \leq 10$ (both X and Z views in CES.)
- abs(dX) $\leq$ 1.5 cm.
- abs(dZsin(θ)) $\leq$ 2.5 cm.
- Lshr(2-tower) $\leq$ 0.2, Lshr(3-tower) $\leq$ 0.5
- Had/Em(3-tower) $\leq$ 0.04
- Wire pulse height(CES) $\geq 0.3 \times p^*$, normalized CES 7-channel pulse height.
- $E/p \leq$3; "p" includes both conversion tracks if they share the same wedge.
- p_T(trigger)$\geq$ 5GeV/c

References

1. A. B. Wicklund, "E/p Calibration from Data", CDF Note 1233, 1990.
2. CDF collaboration, "Measurement of the W Mass", CDF Note 2864, 1994.
3. R. Kadel, "On the thickness of the CTC inner support cylinder", CDF Note 2804, 1994.
4. F. Bedeschi et al., Nucl. Instr.Meth.A268, 50, 1988; the guard wire diameter decsription is given incorrectly here. Our description is based on communication with A. Mukherjee.
5. P. T. Lukens, "A technique for photon conversion detection", CDF Note 2797, 1994.
6. We assumed CTC setting errors of 400 μm (SL0), and 300 μm (SL2,4,6,8) in the constrained fits, following communications with P. Berge.
7. "CRC Handbook of Chemistry and Physics", R.C. Weast,ed., 68'th edition, 1987-88.
8. A.B. Wicklund and F. Ukegawa,"Separation of QCD prompt-γ and π^0 production in the conversion electron sample", CDF Note 2080, 1993.
9. C. Albajar et al. (UA1 Collab.), Phys. Lett. 209b,397,1988.
10. B. Rossi, "High Energy Particles",Prentice-Hall, 1952.
11. K.O.Mikaelian and J. Smith, Phys. Rev. D5,1763, 1972.

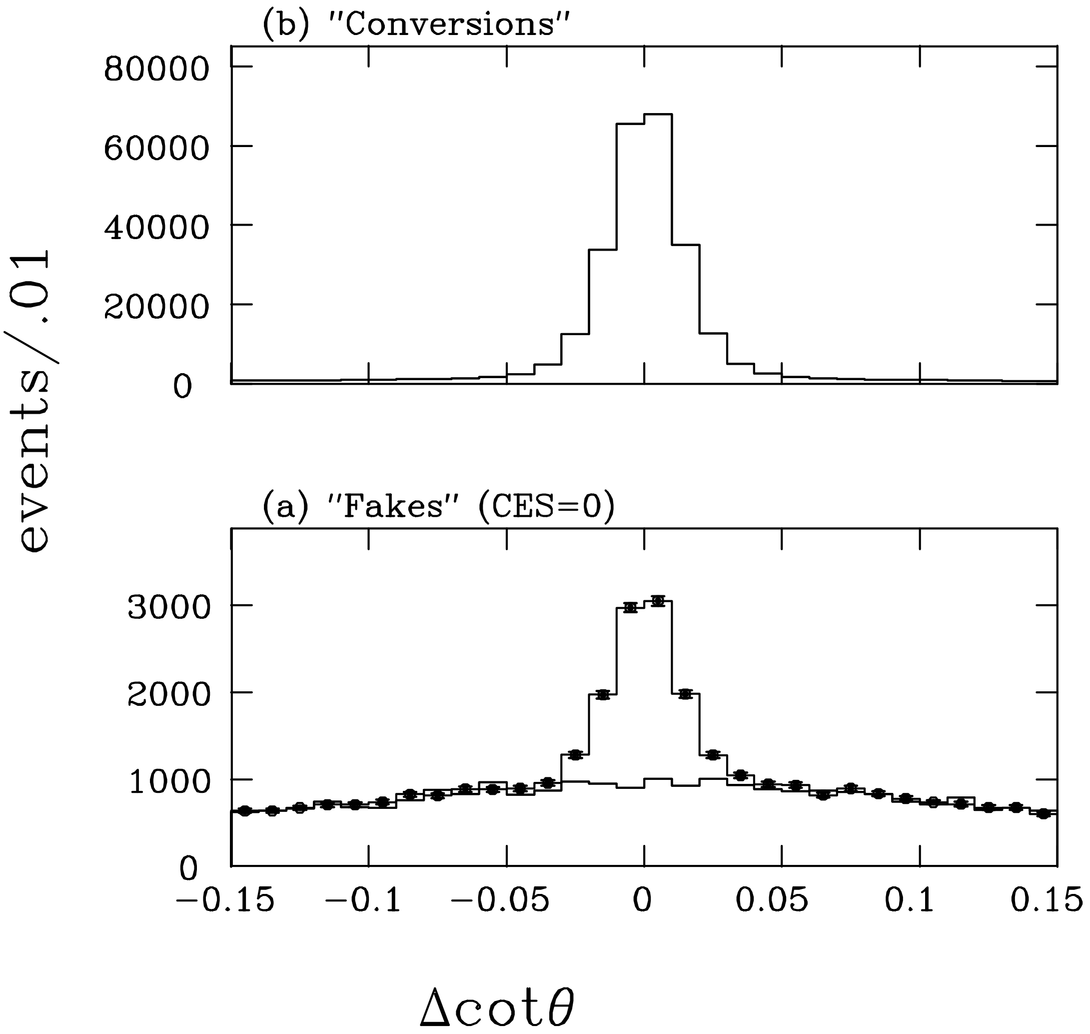

Figure(1): $\Delta \cot(\theta)$ distributions for "fakes" (a) and good conversions (b);the lower histogram in (a) is for pairs that fail the *Sep* cut and have CES pulse height consistent with zero.

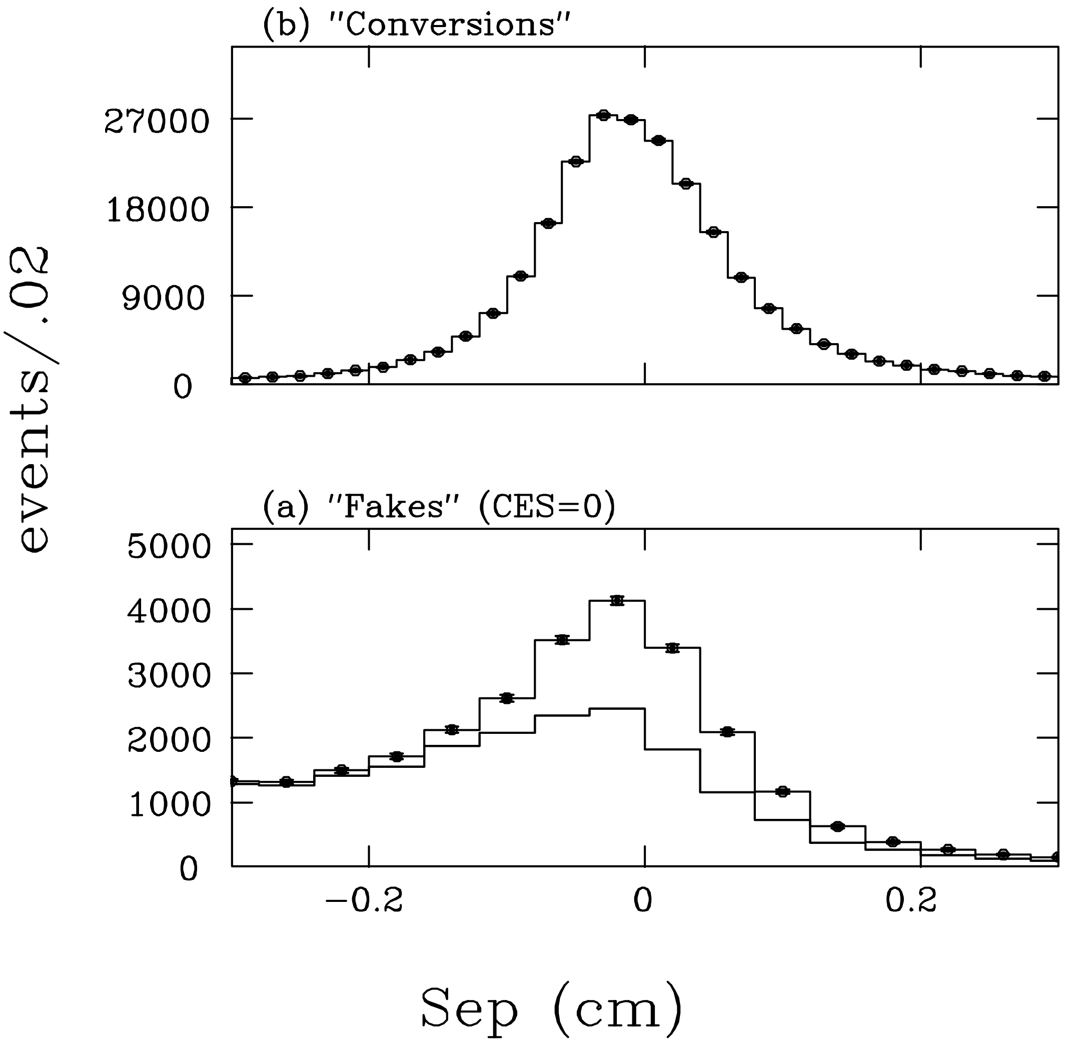

Figure(2): Sep distributions for "fakes" (a) and good conversions (b); the lower histogram in (a) is for pairs that fail the $\Delta Cot(\theta)$cut and have CES=0.

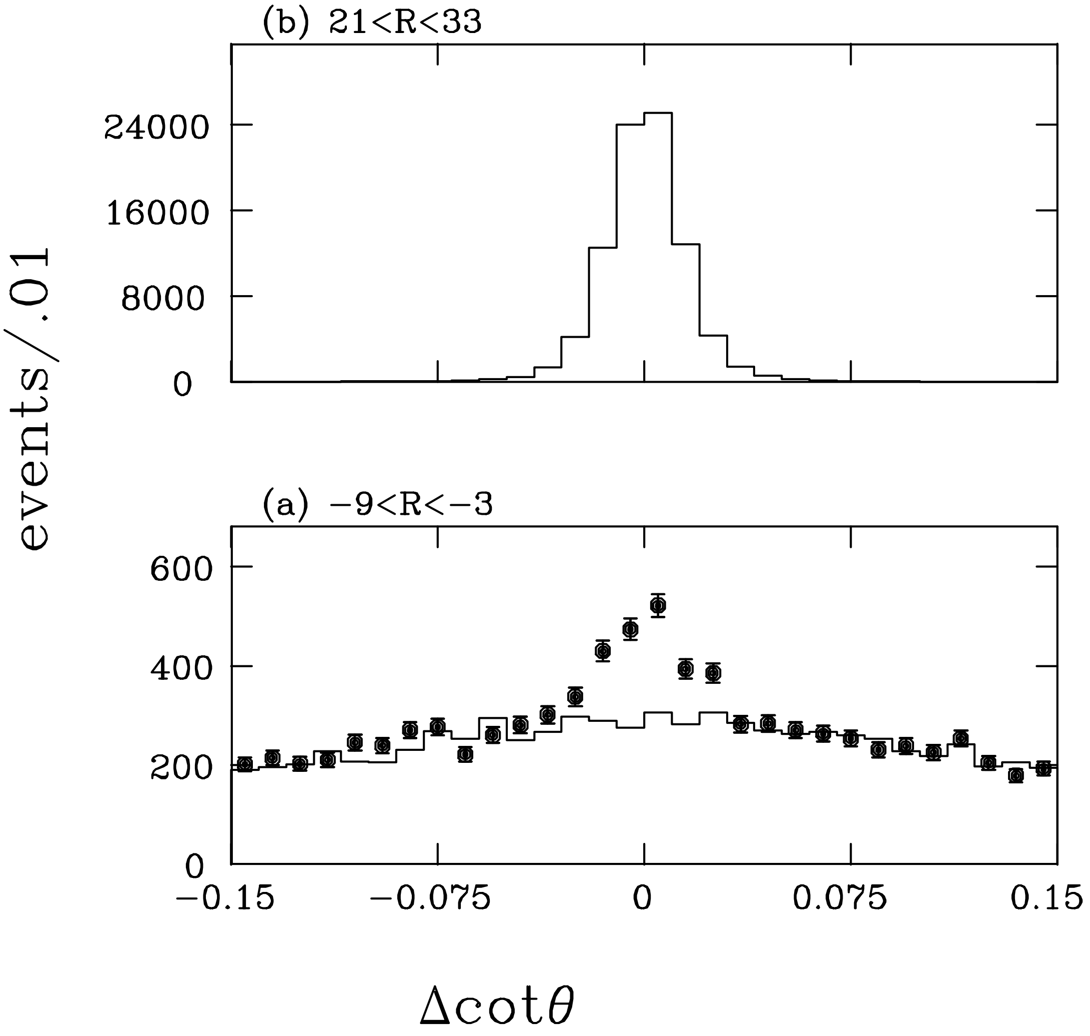

Figure(3): $\Delta\cot(\theta)$ distributions for different slices in R. The lower histogram in (a) is for pairs that fail the *Sep* cut and have CES=0.

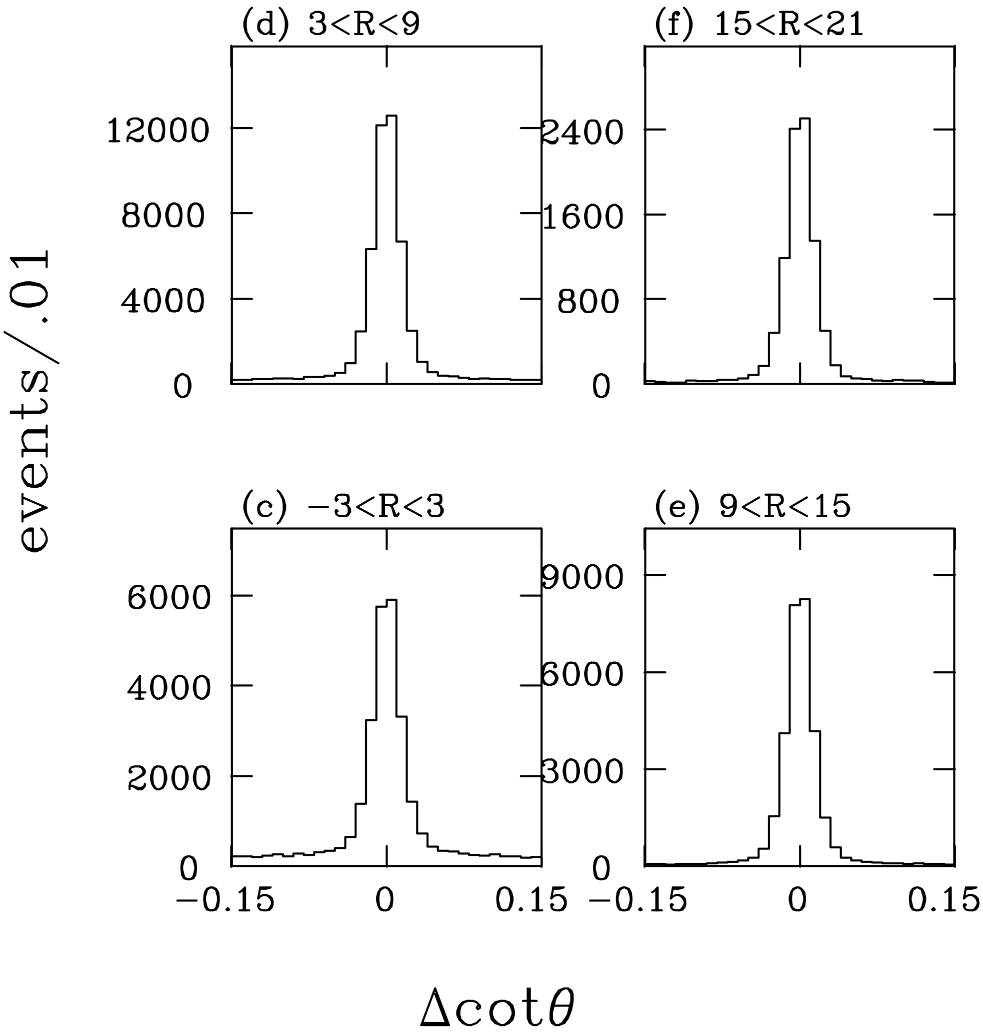

Figure(3) (c-e),$\Delta\cot(\theta)$ distributions for different slices in R.

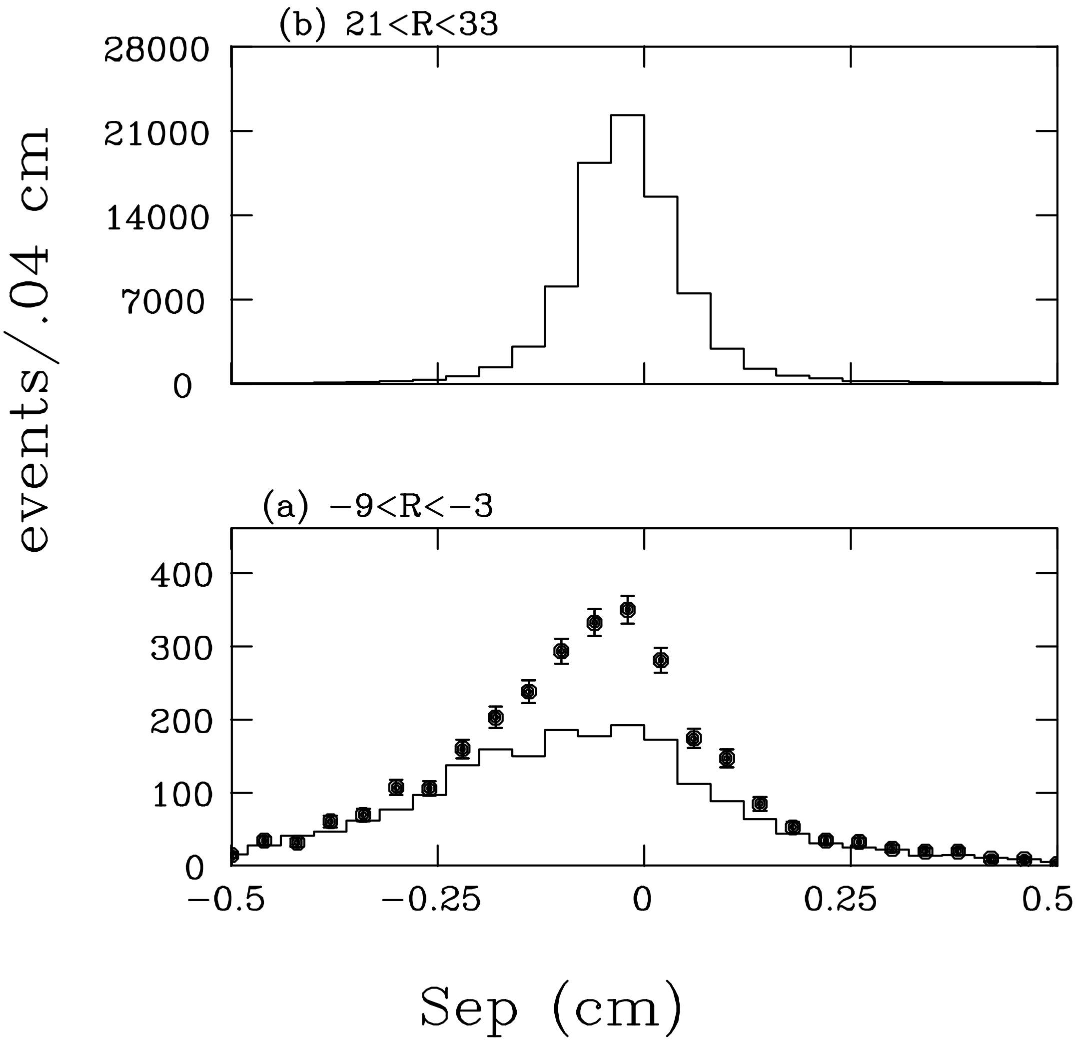

Figure(4): Sep distributions for different slices in R. The lower histogram in (a) is for pairs failing the $\Delta Cot(\theta)$cut.

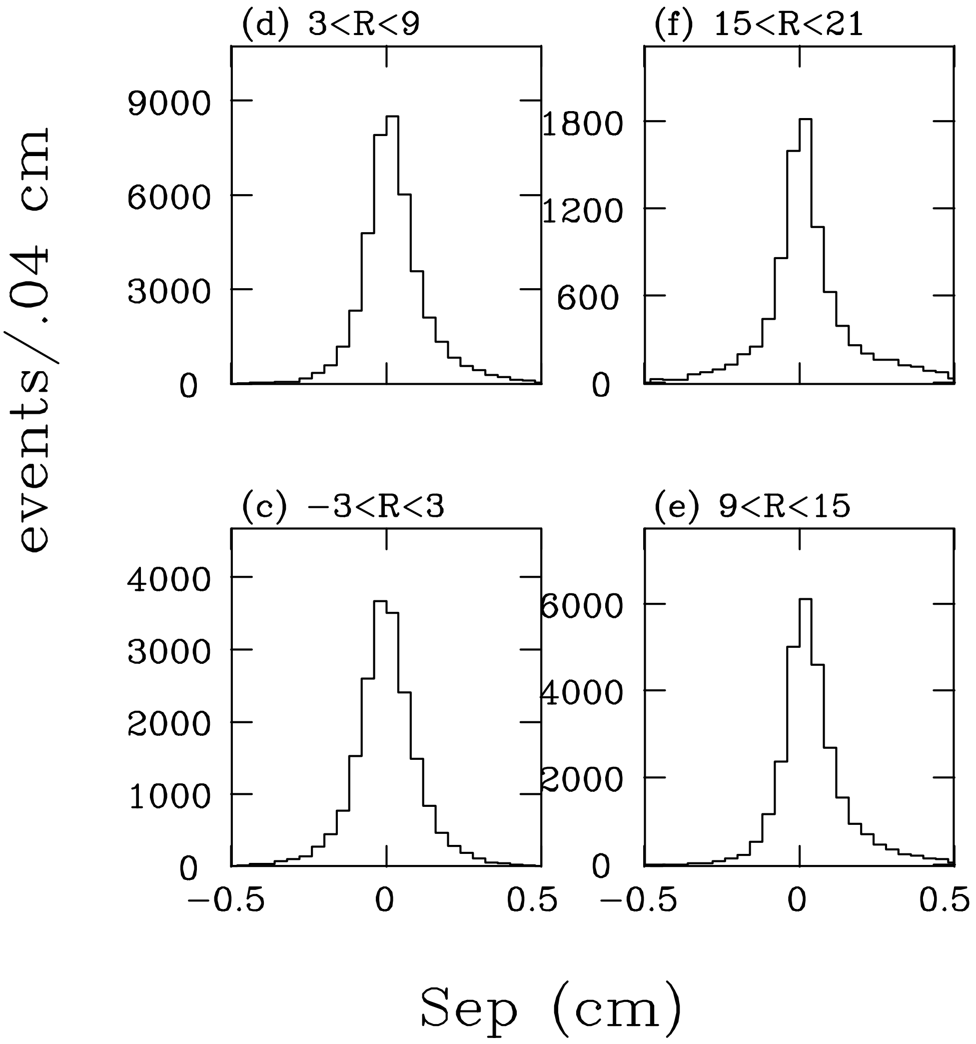

Figure(4) (c-e), *Sep* distributions for different slices in R.

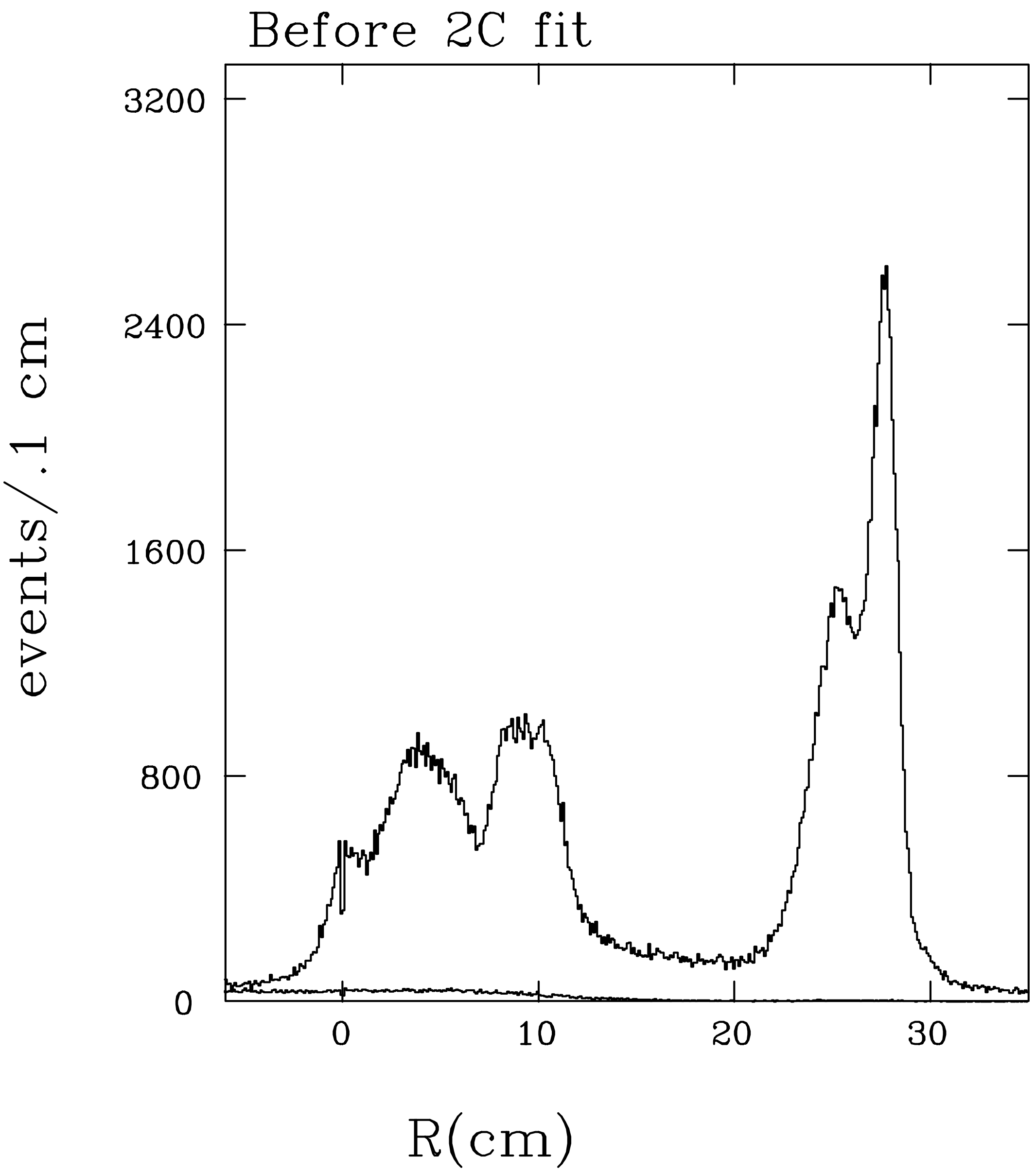

Figure(5): R-distribution using raw, measured R-values; the lower trace is the fake conversion background estimate.

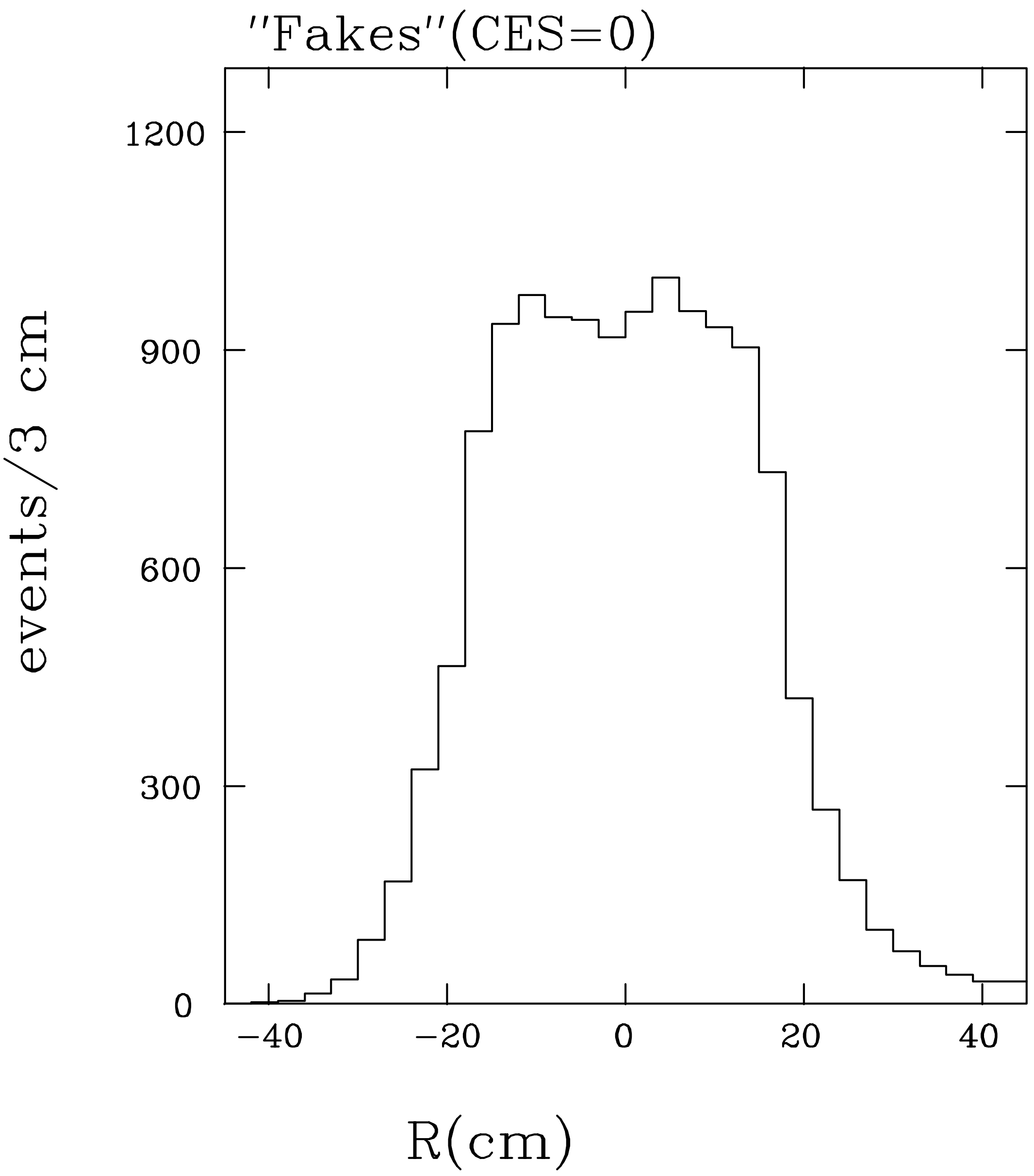

Figure(6): R-distribution for fake conversions, defined by abs(Sep) $\leq$ 0.5 cm, abs($\delta\cot(\theta)$) $\geq$ .06, and CES/p* $\leq$ 0.05.

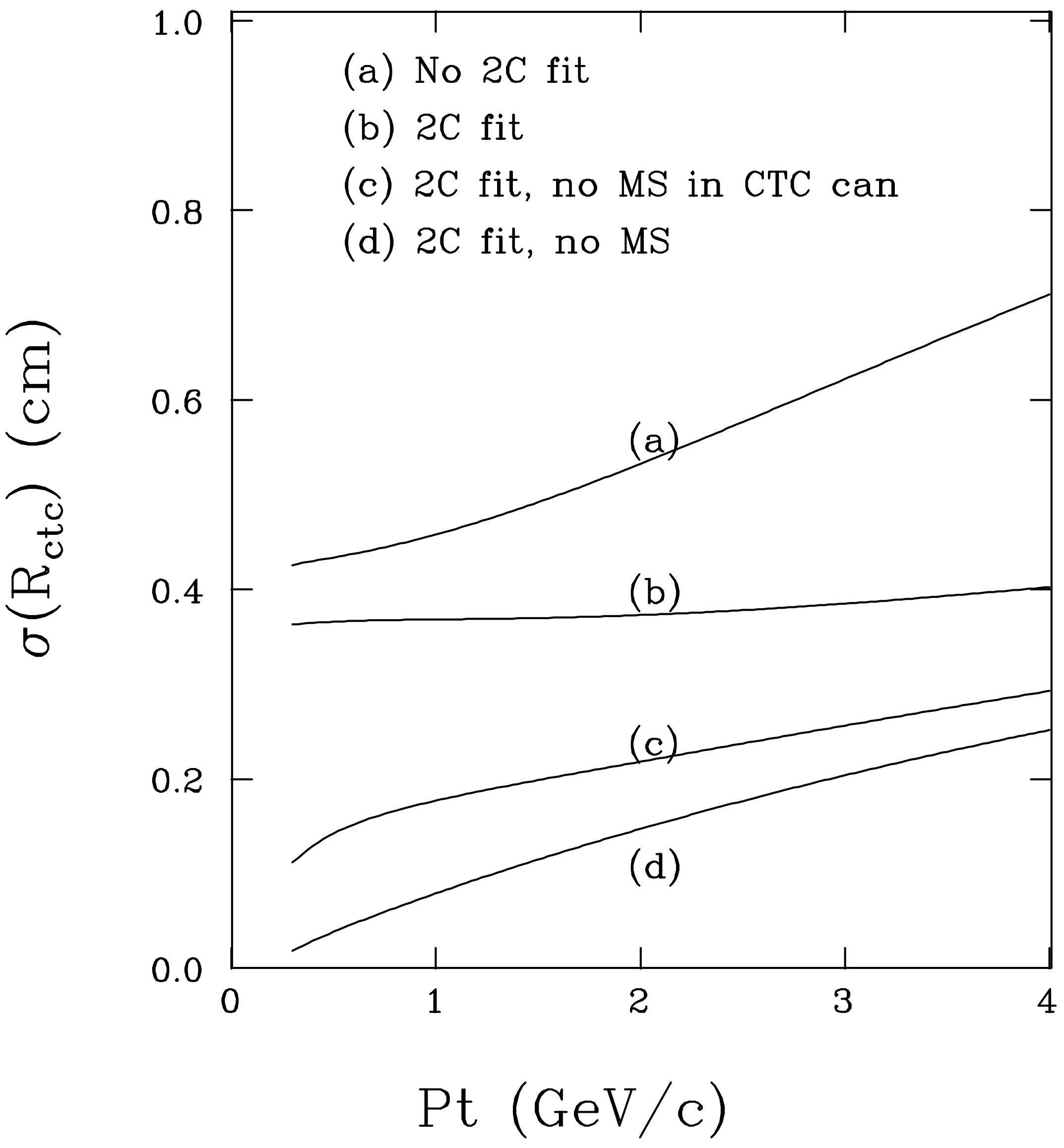

Figure(7): predicted R resolutions versus p_T(partner), comparing effects of 2C fit and multiple scattering assumptions.

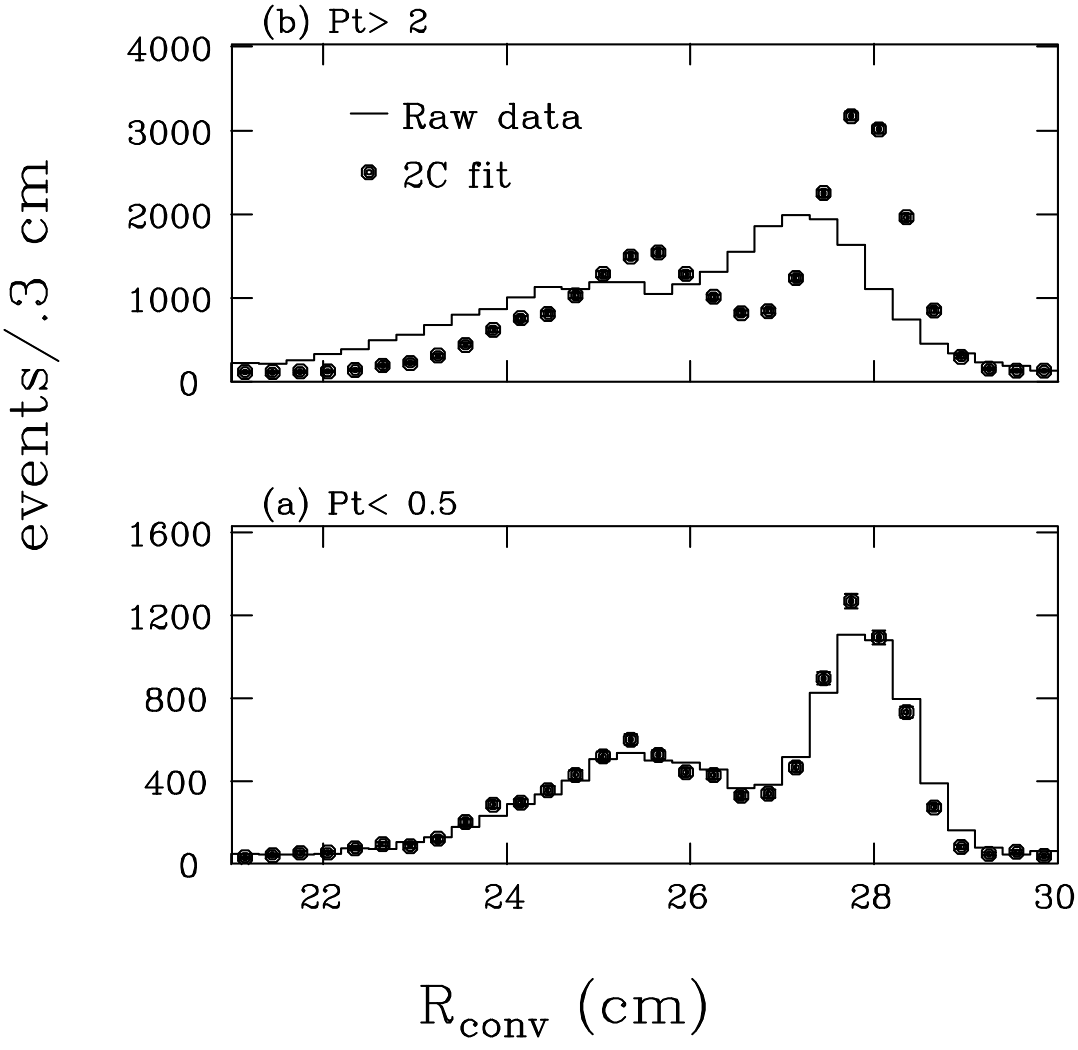

Figure(8): R-distributions before (histogram) and after (points) 2C-fits, for two slices in p_T.

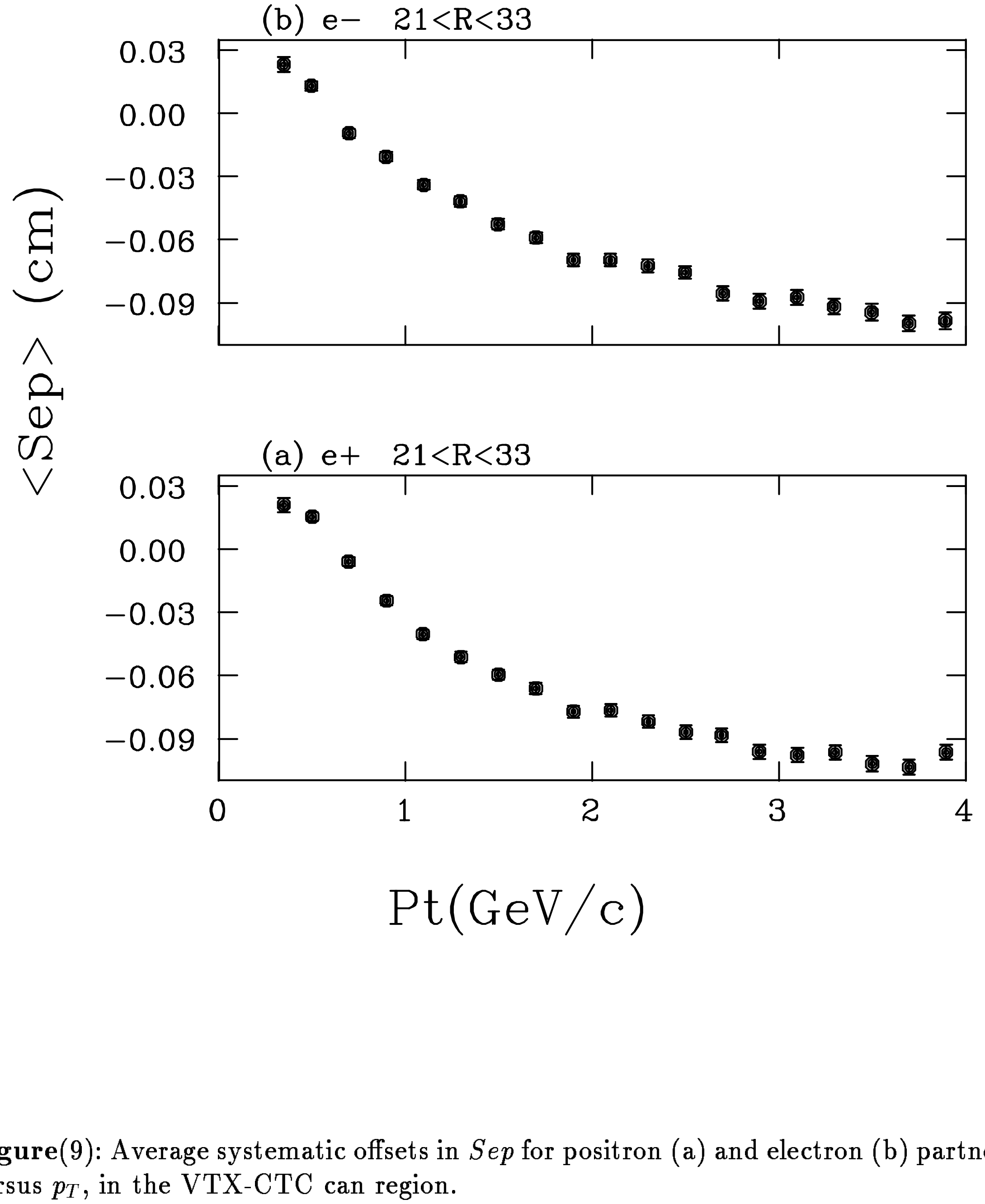

Figure(9): Average systematic offsets in *Sep* for positron (a) and electron (b) partners, versus p_T, in the VTX-CTC can region.

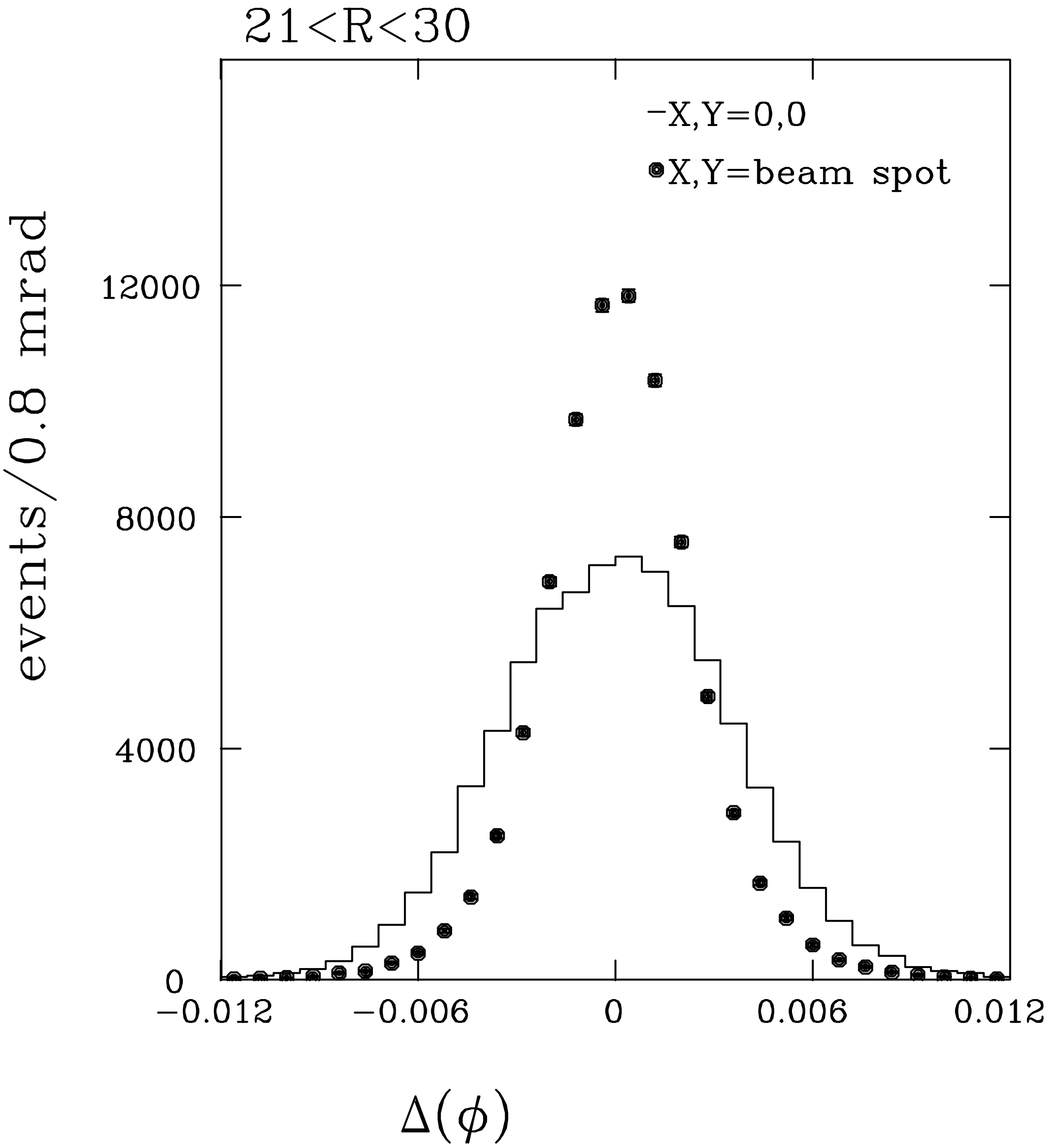

Figure(10): Azimuthal difference between measured conversion photon direction, and direction of radial vector from the origin to the conversion point, for $21 \leq R \leq 30$ cm.; the histogram and solid points are for origins at (0,0) and the SVX beam spot, respectively.

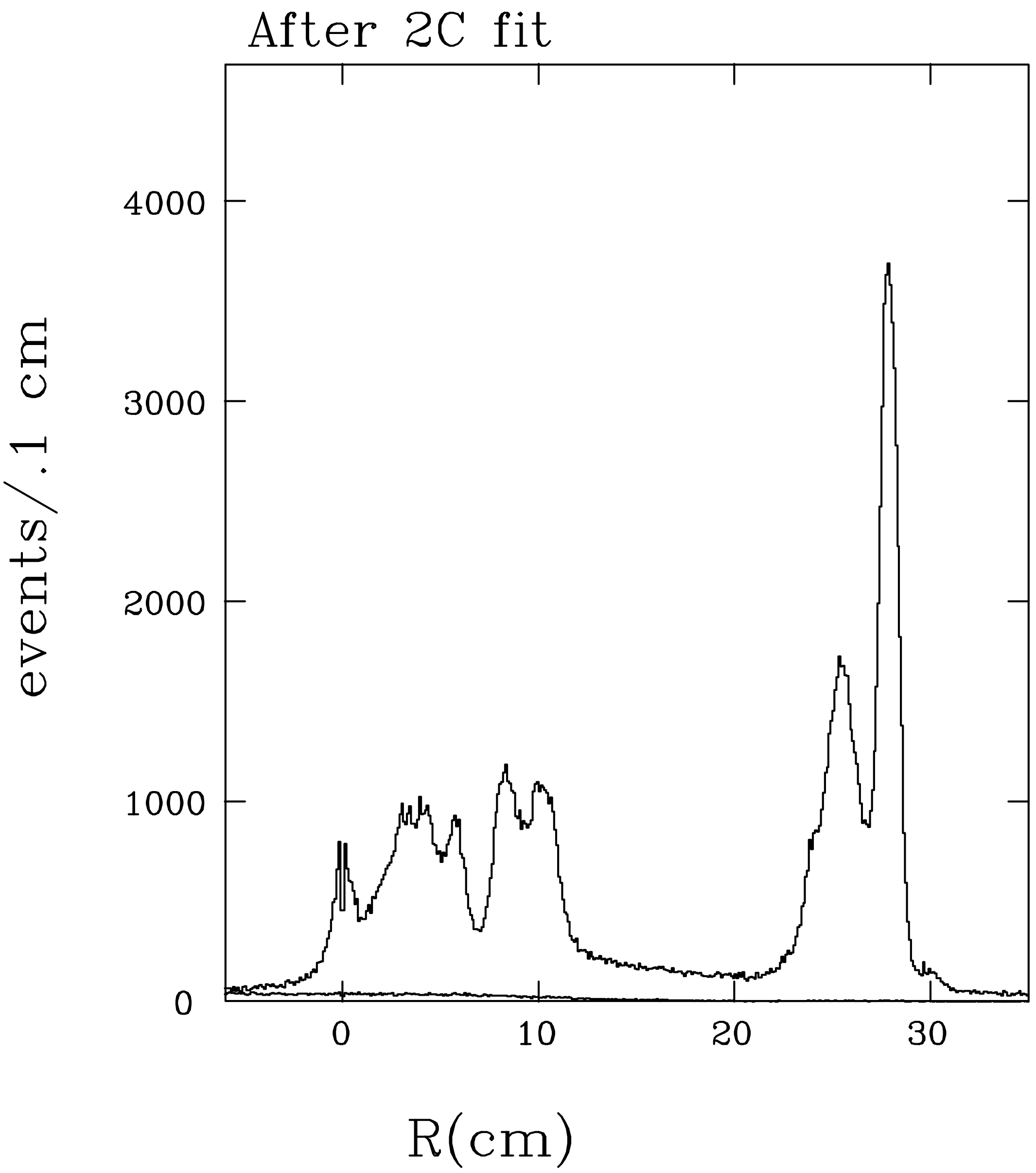

Figure(11): R-distribution after 2C fit; the lower trace shows the estimated fake background rate.

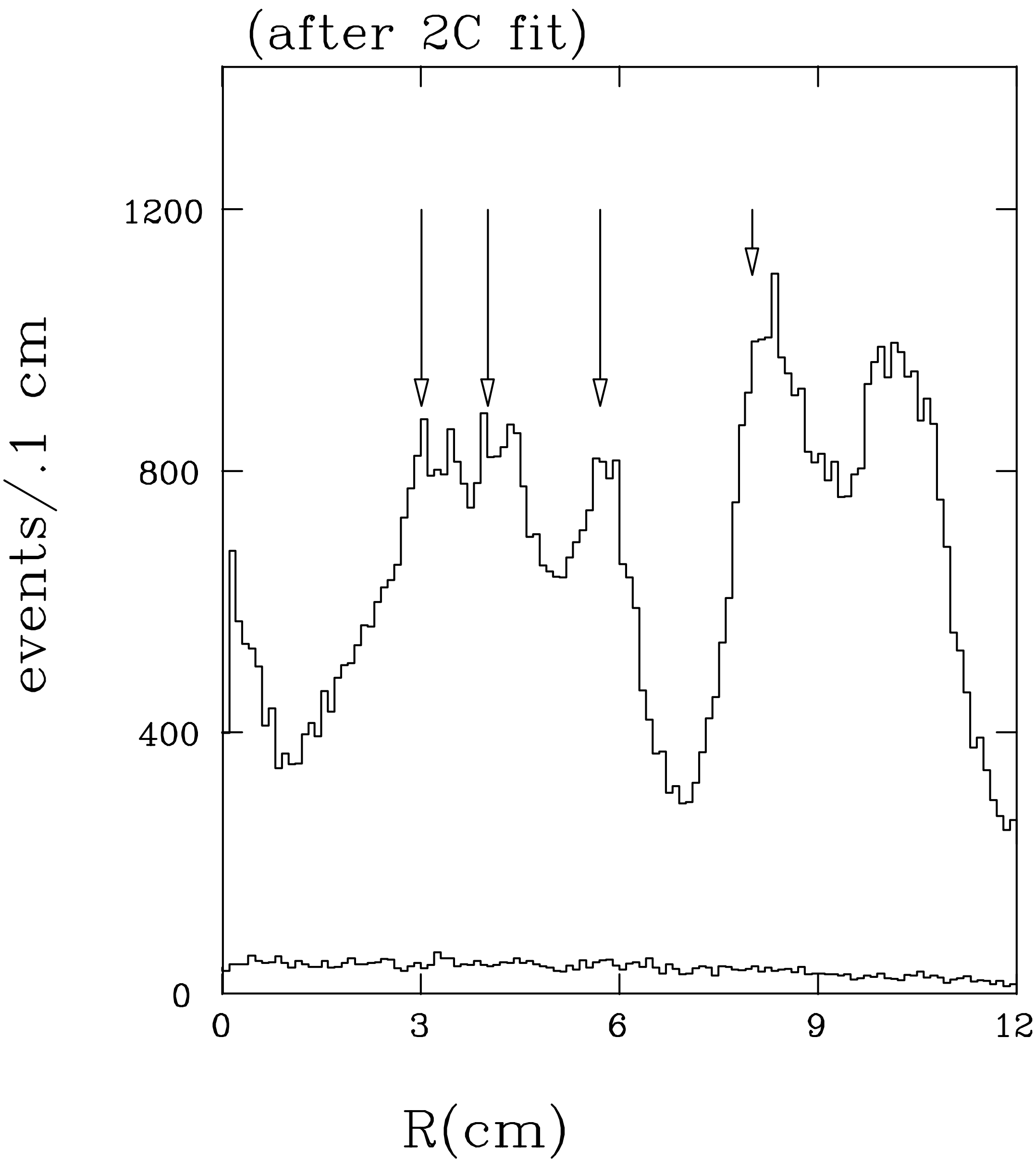

Figure(12): Blowup of R distribution in the SVX region; arrows indicate average locations of SVX ladders.

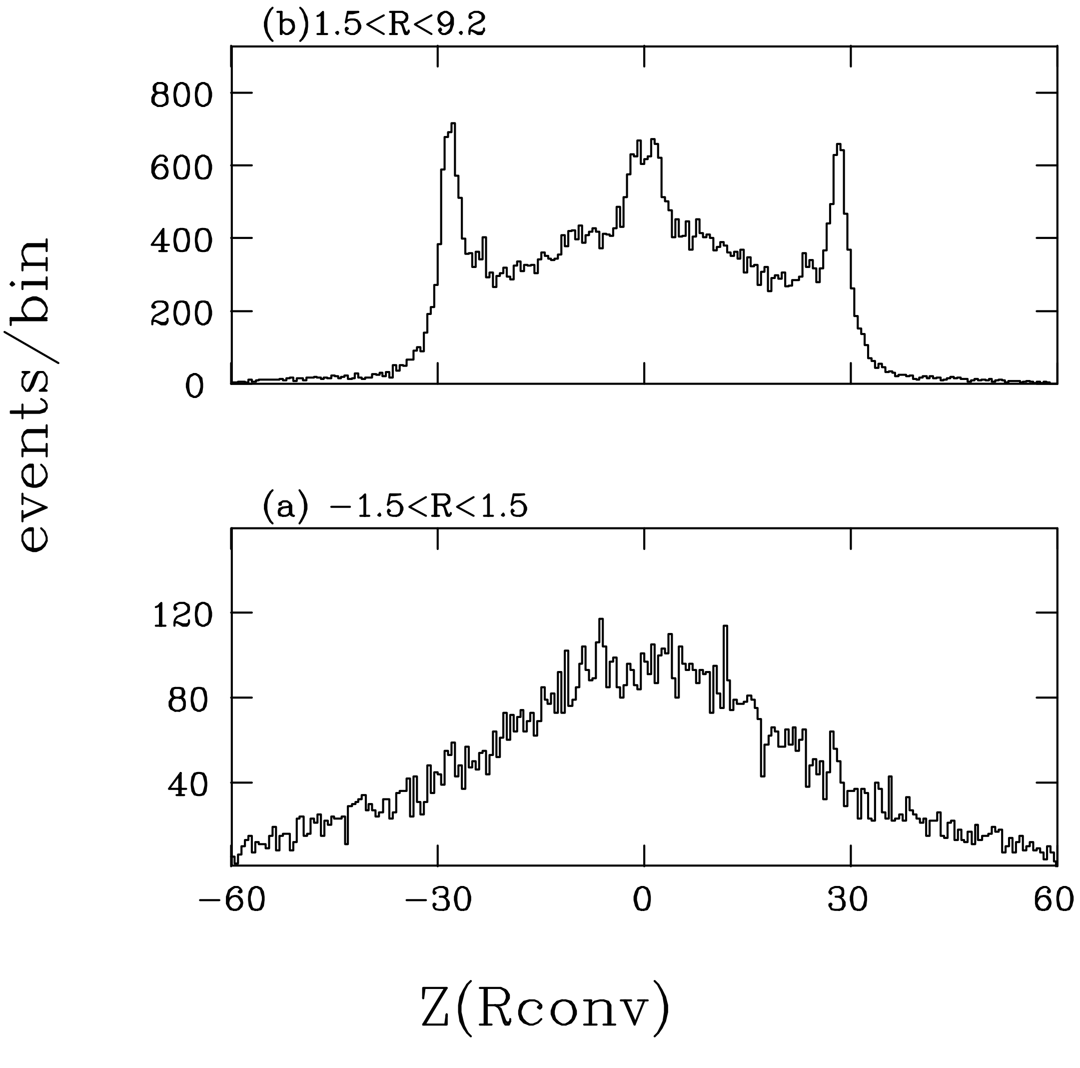

Figure(13): Distribution of (fitted) Z at the conversion point, sliced in R.

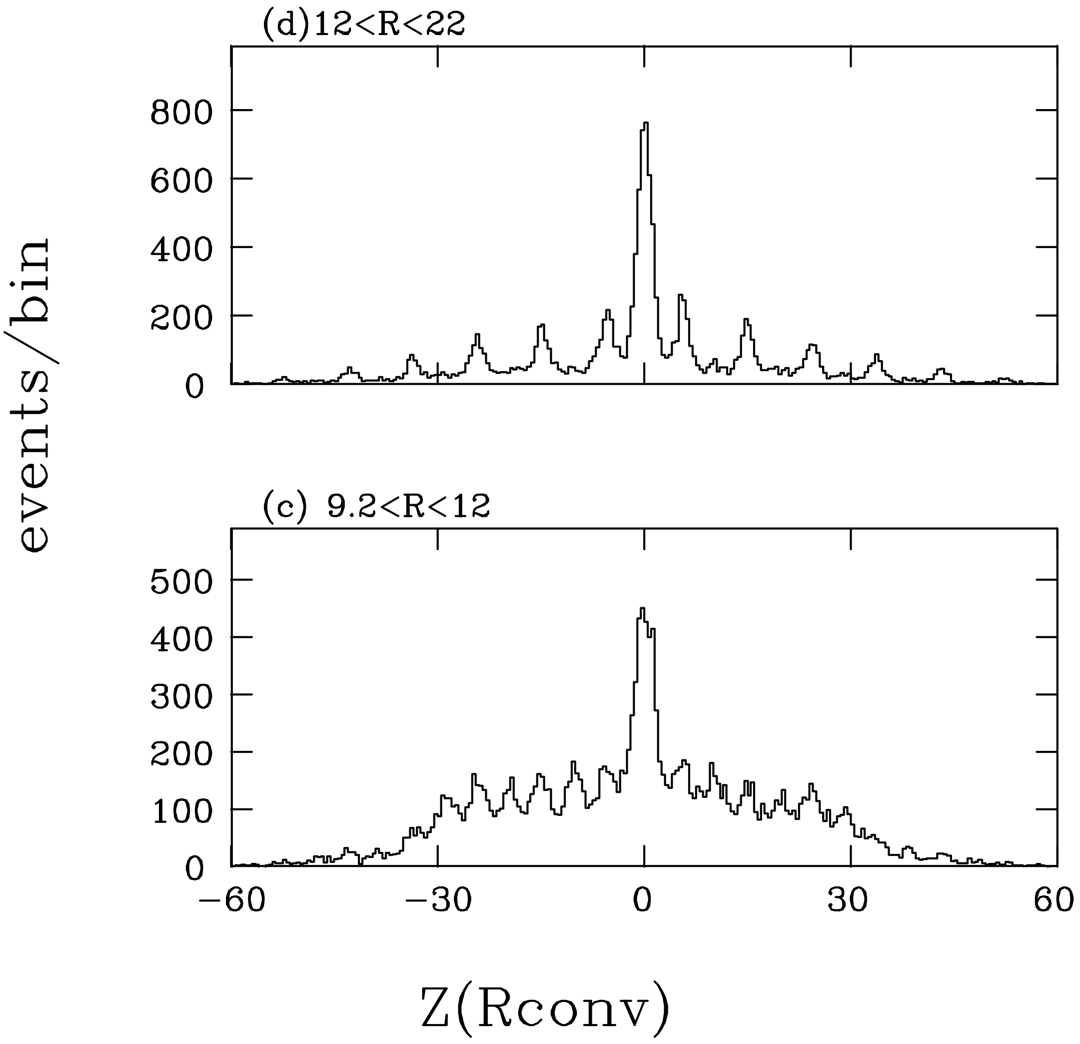

Figure(13) (c,d), Z-distributions sliced in R.

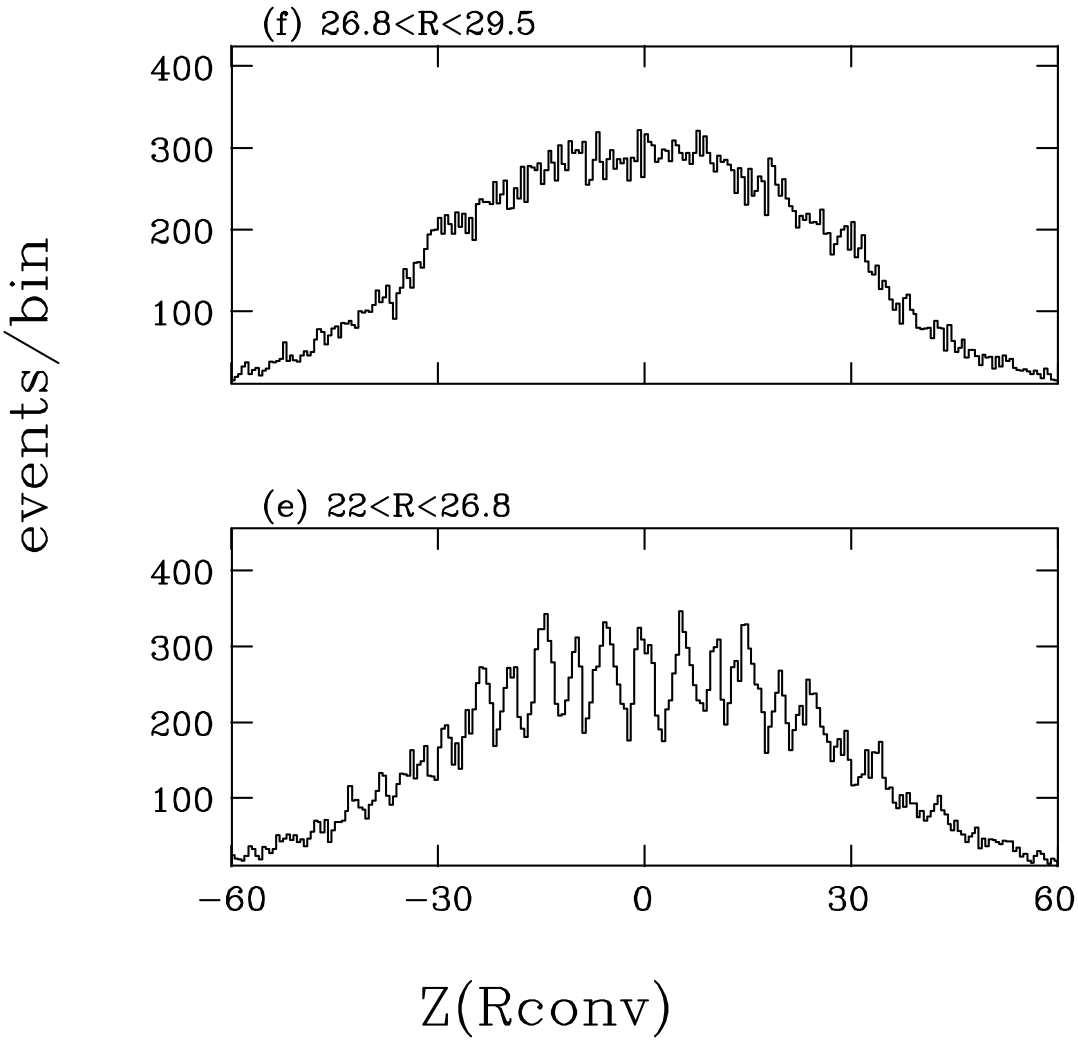

Figure(13) (e,f), Z-distributions sliced in R.

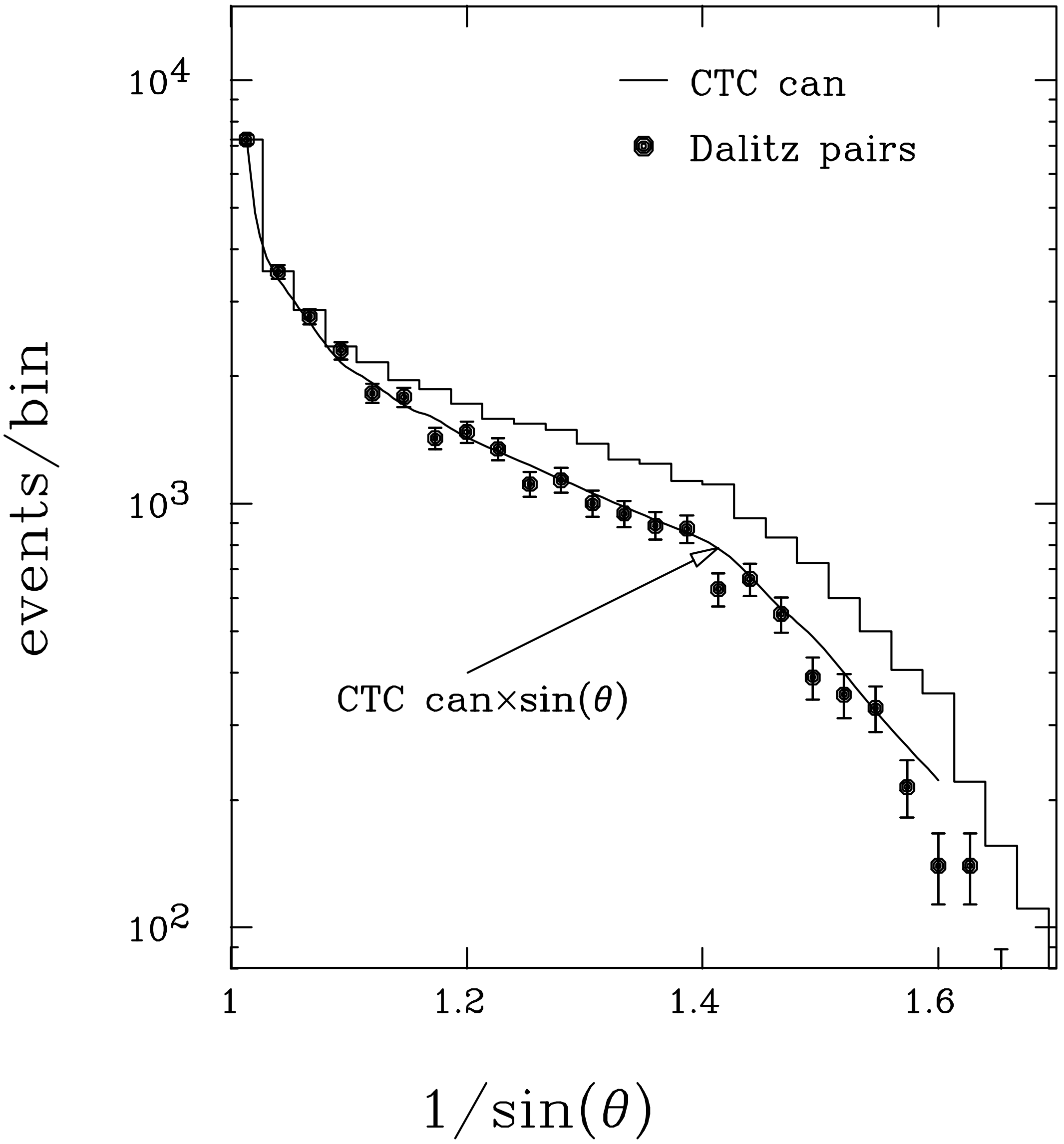

Figure(14): Distribution in $1/\sin(\theta)$ for events in the CTC can region(histogram) and at R=0 (points); the smooth curve is the top histogram weighted by $\sin(\theta)$. Both distributions are normalized in the first bin.

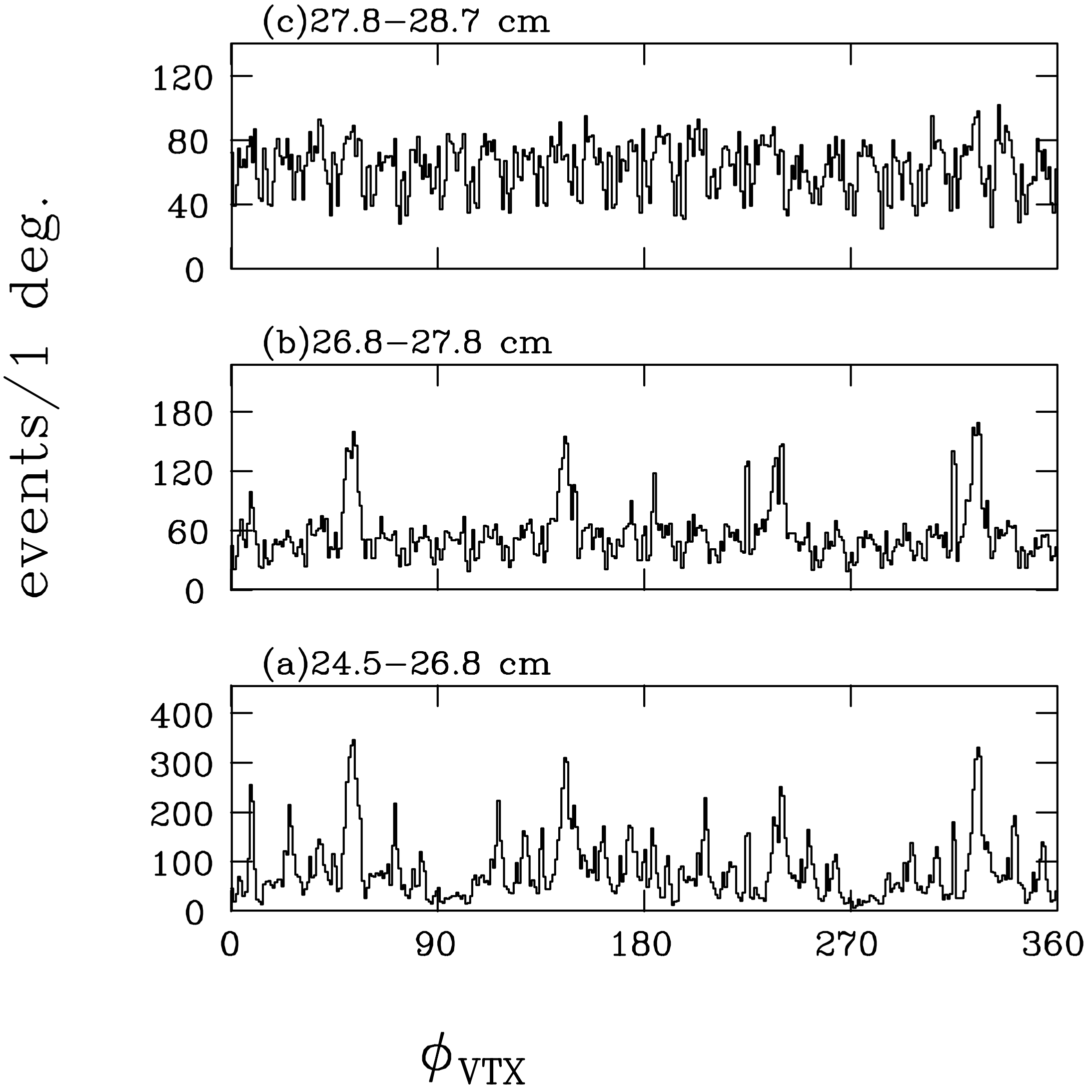

Figure(15): ϕ_{vtx} distribution for three R slices in the VTX- CTC can region; ϕ_{vtx} is mirror-reflected for Z $\leq$0, as explained in text.

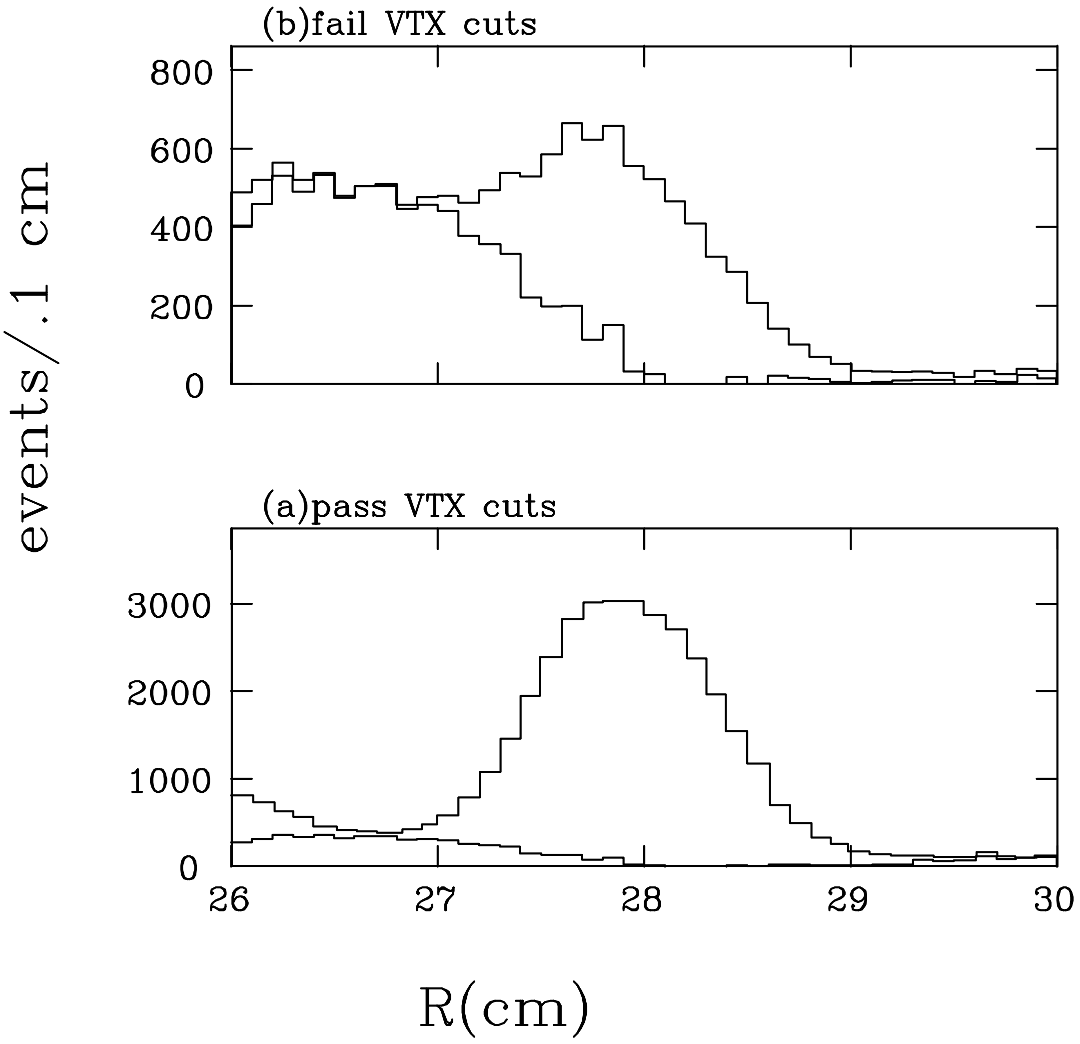

Figure(16): R distributions in VTX-CTC can region passing (a) and failing (b) SVX-cable cuts in ϕ; the lower histograms are estimates of background shape contributions near the CTC can.

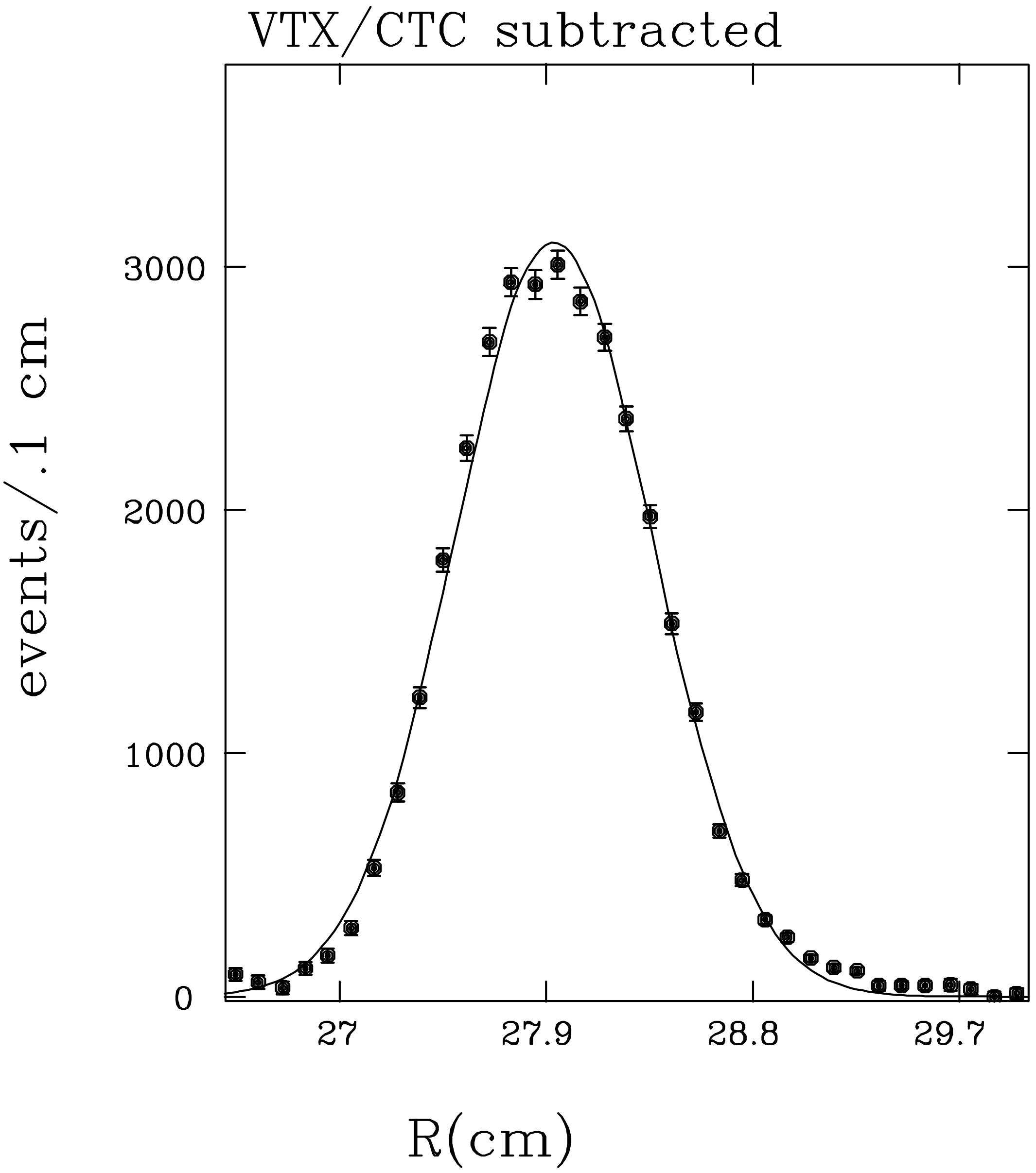

Figure(17): Background-subtracted CTC can signal, for events passing SVX-cable cuts in ϕ, with Gaussian fit.

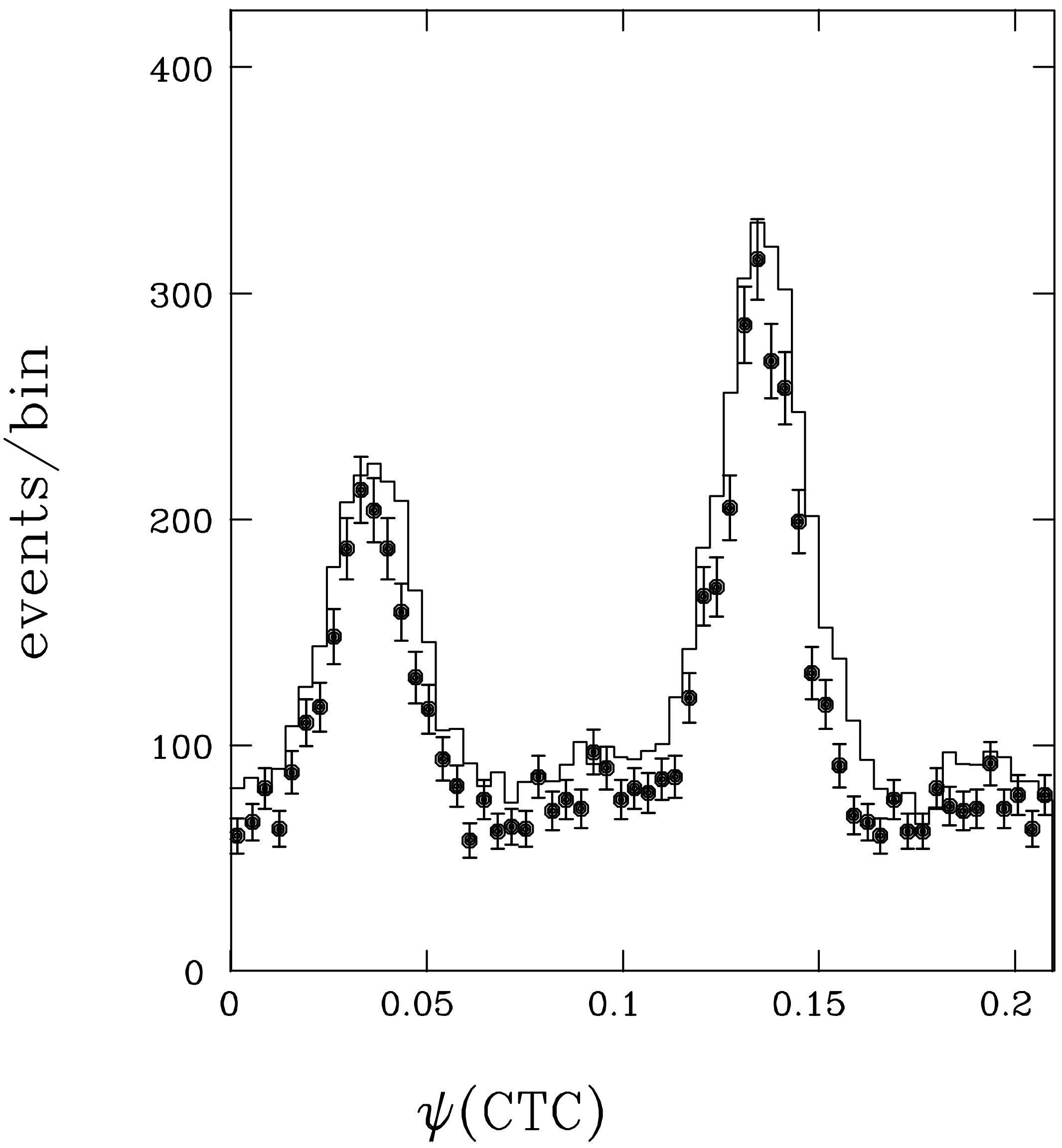

Figure(18): Distribution in the angle ψ for data (points) and monte-carlo (histogram).

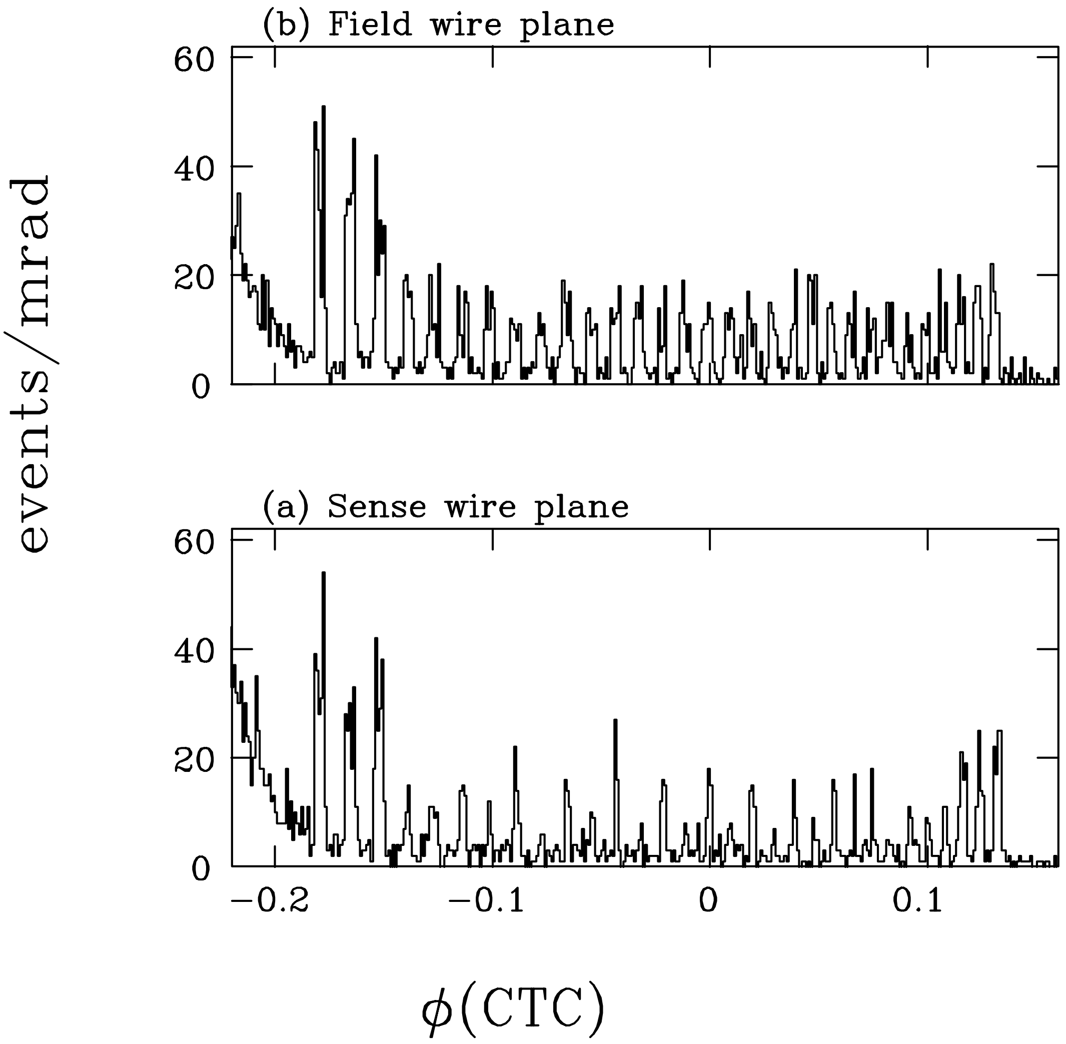

Figure(19) (a,b): ϕ distributions for SL0 conversions satisfying abs($\Delta\psi$) $\leq$0.035 with respect to the sense (a) and field (b) planes.

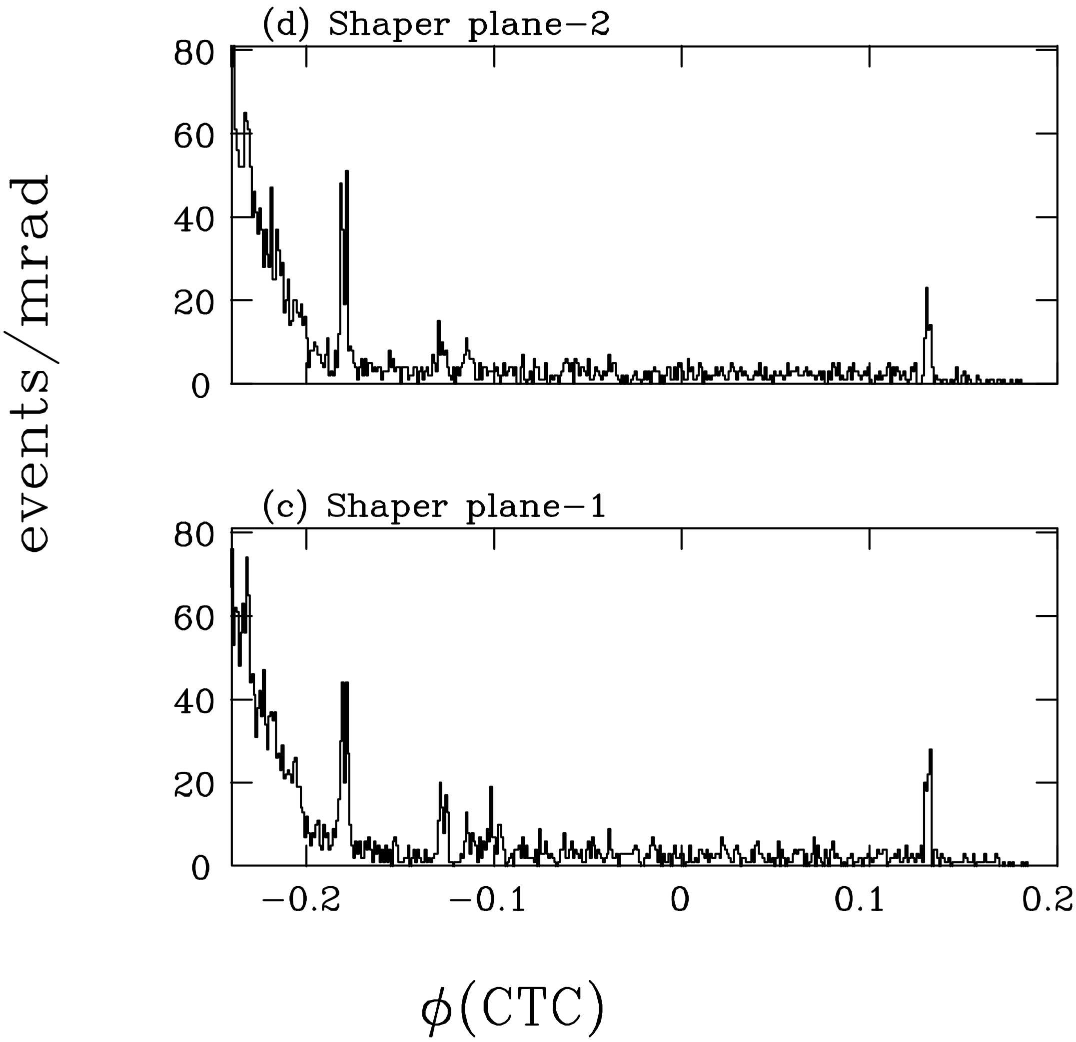

Figure(19)(c,d): ϕ distributions for SL0 conversions in the two shaper wire planes.

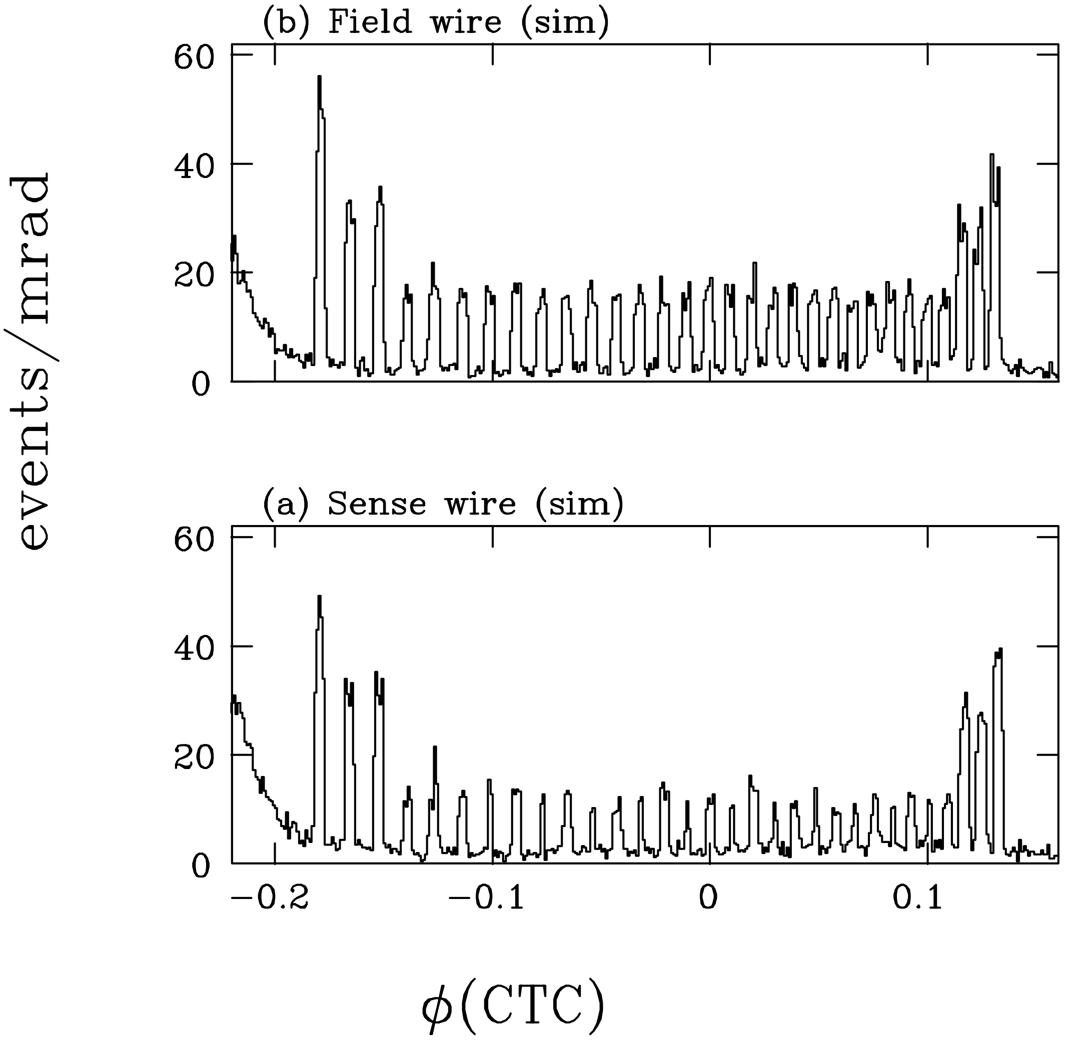

Figure(20)(a,b): ϕ distributions for monte carlo events satisfying sense (a) and field (b) wire plane ψ cuts.

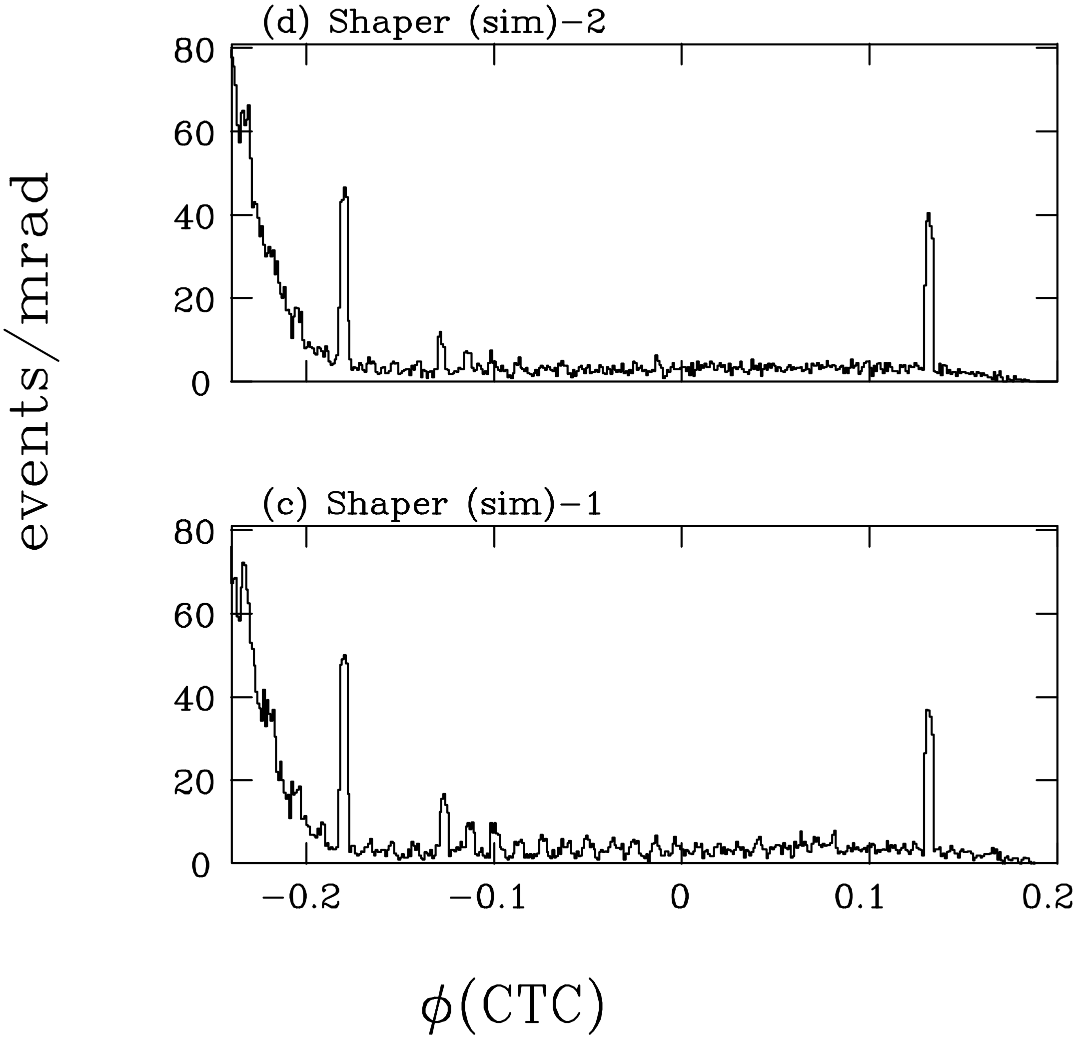

Figure(20)(c,d): ϕ distributions for monte carlo events satisfying ψ cuts for the two shaper planes.

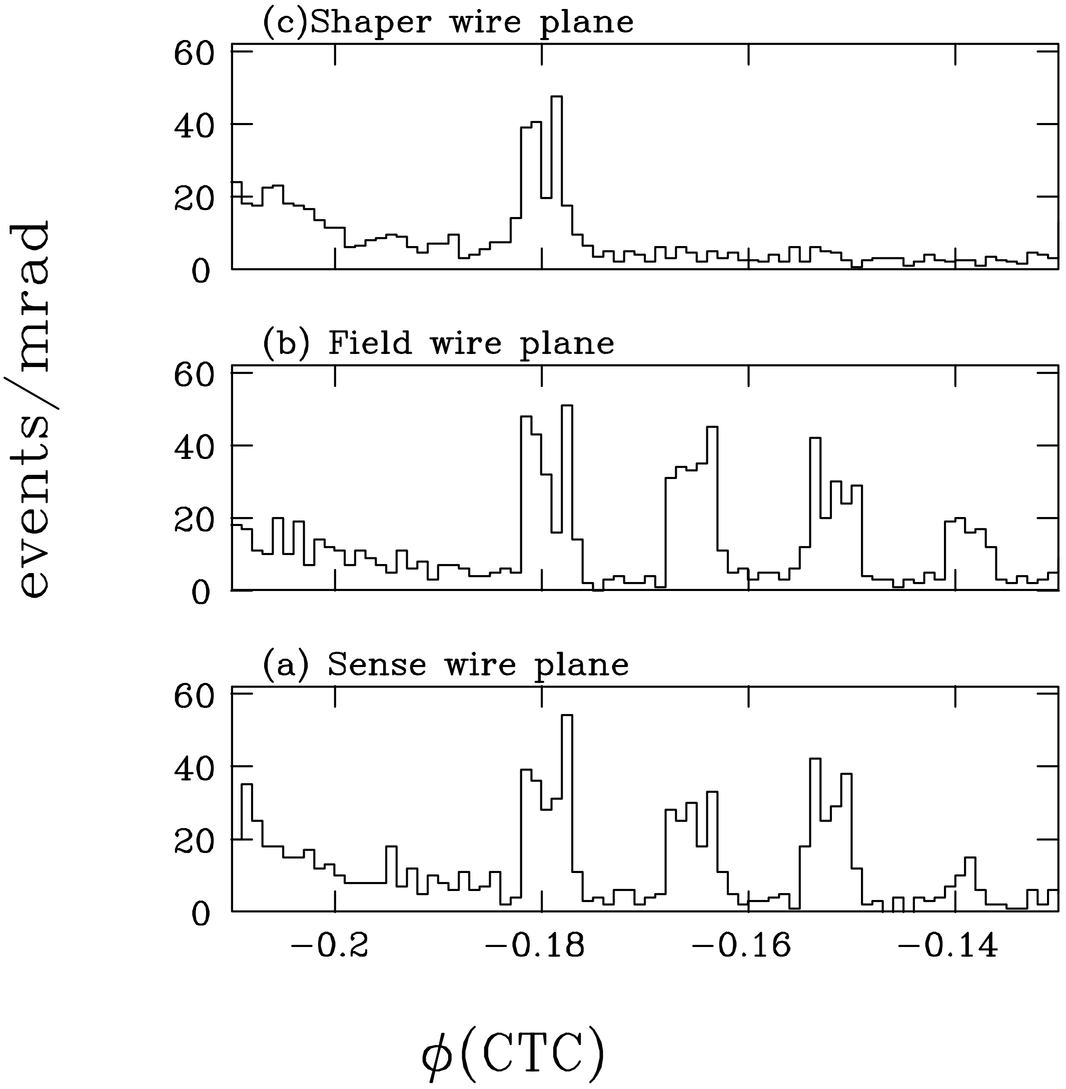

Figure(21): Blowup of ϕ distributions in the inner guard wires for sense (a), field (b), and shaper (c) planes.

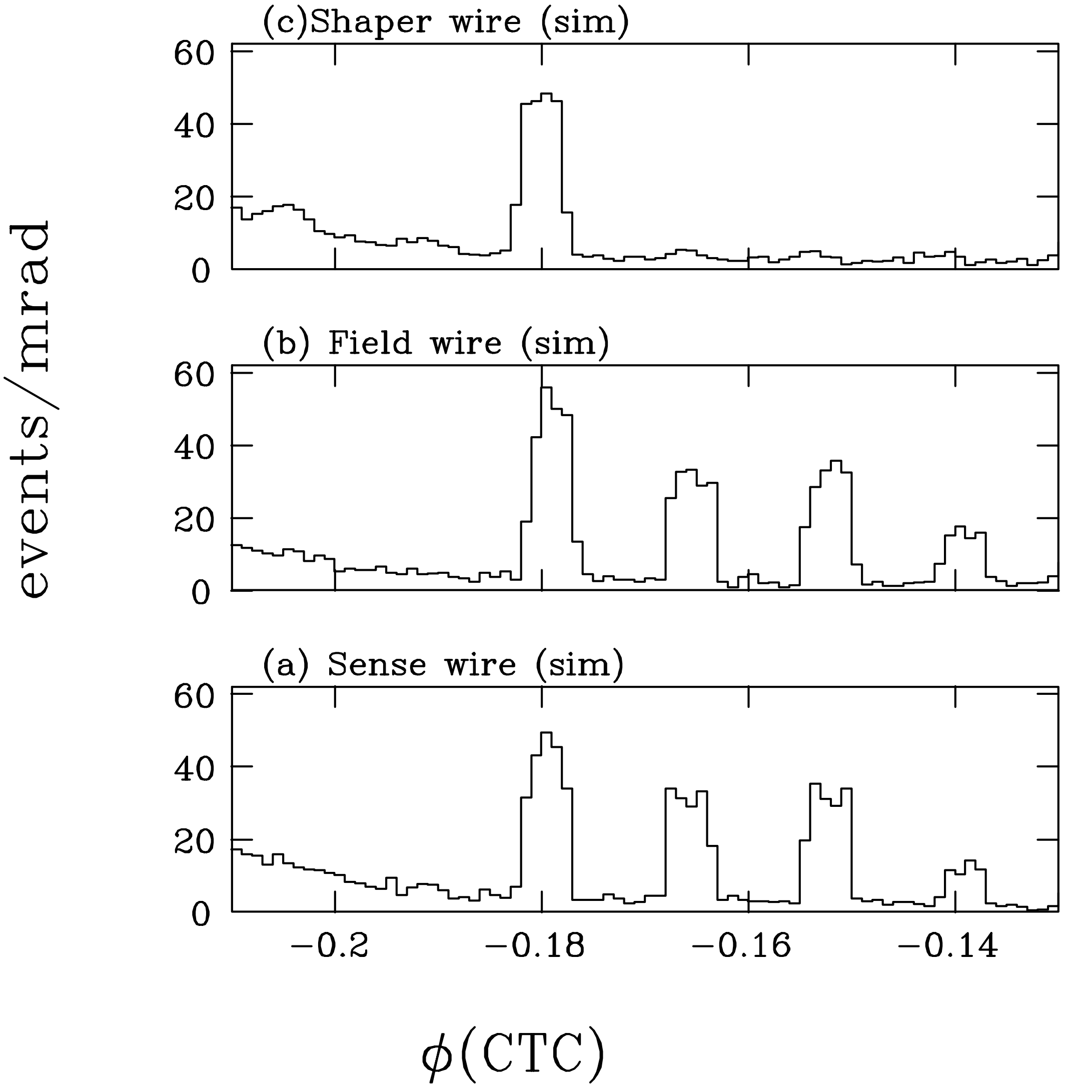

Figure(22): Blowup of ϕ distributions in the inner guard wires for monte carlo simulated conversions.

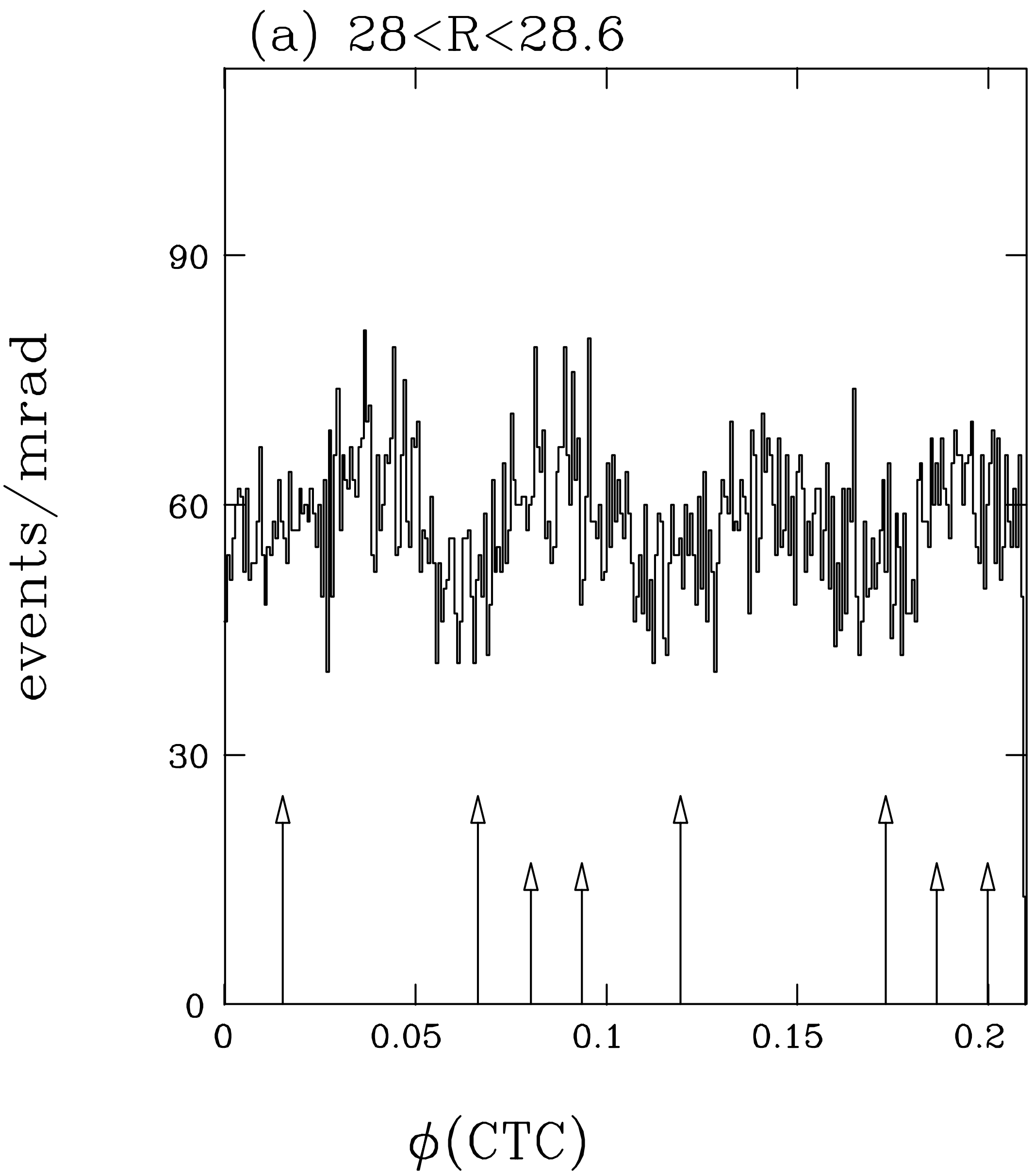

Figure(23): ϕ distribution for conversions in the CTC can, 28 $\leq$R $\leq$ 28.6 cm. ϕ is folded to project onto a single cell in SL0, ie. mod($2\pi/30$). The arrows indicate locations of inner three guard wires used for calibration; the arrow heights reflect the relative amounts of material in each wire.

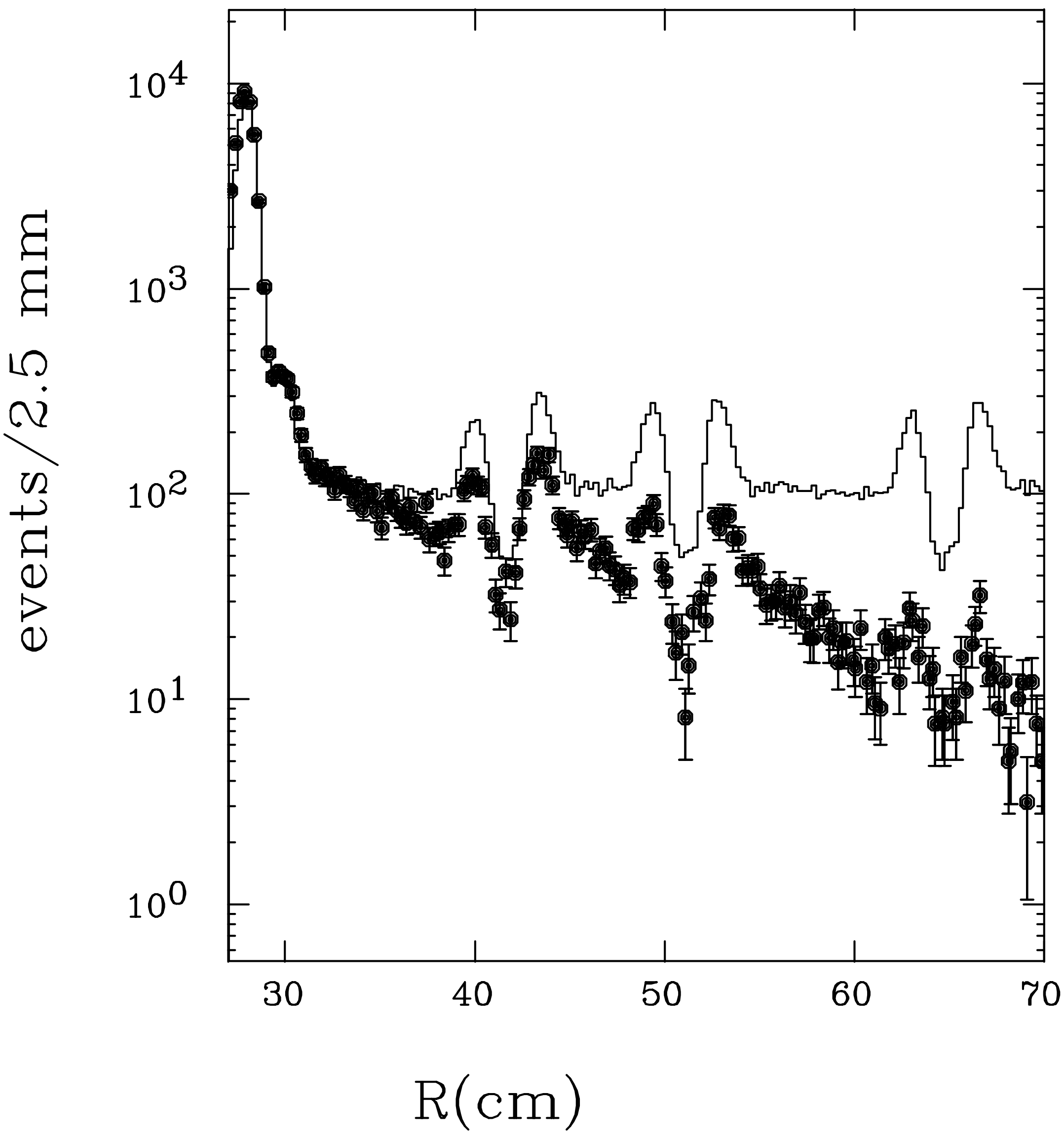

Figure(24): R-distributions for data (points) and monte carlo (histogram) in the first four SL's.

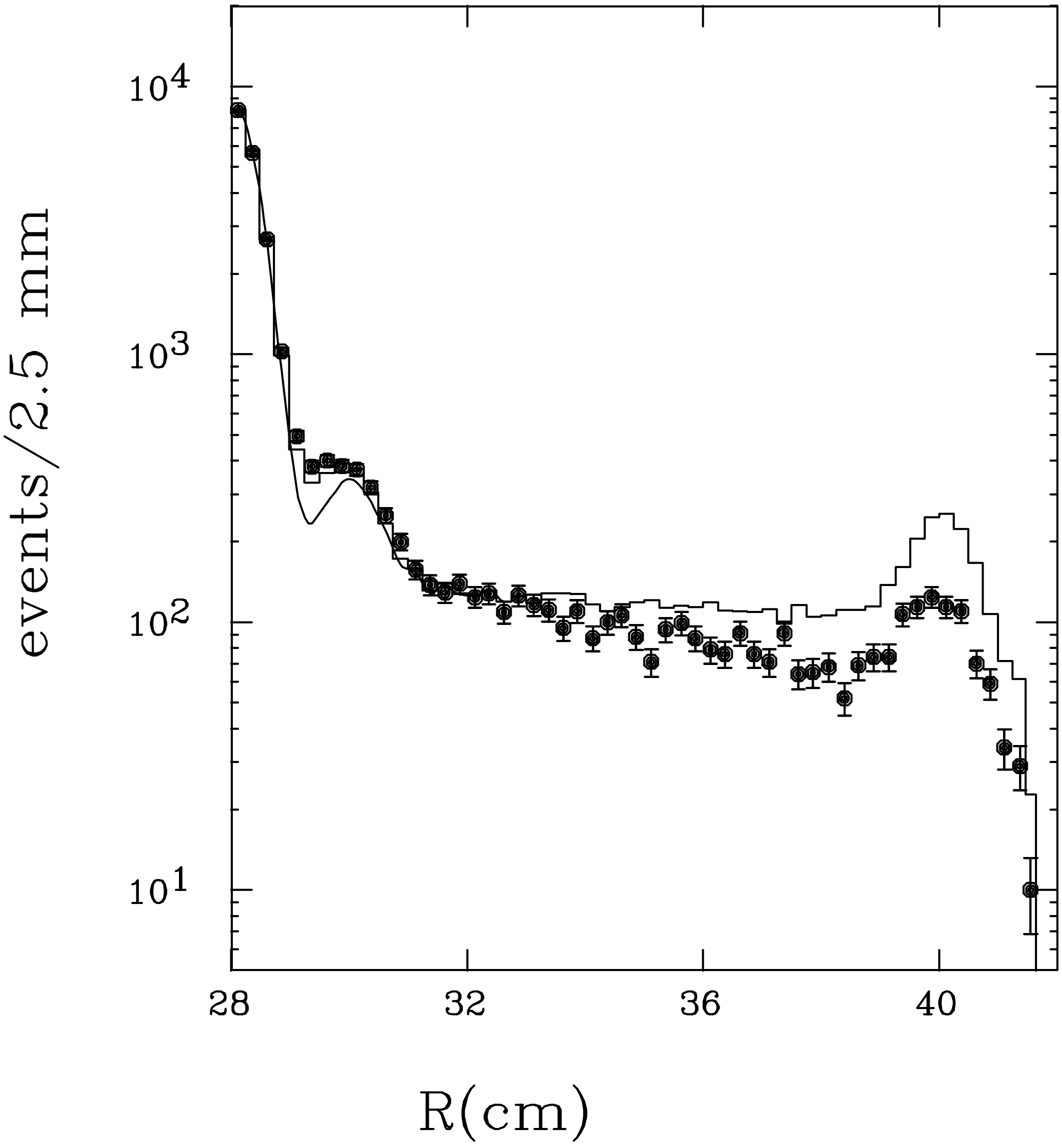

Figure(25): R-distribution for data (points) and monte carlo (histogram) in SL0. The solid curve is the monte carlo without the non-Gaussian tail added to the CTC-can R-resolution.

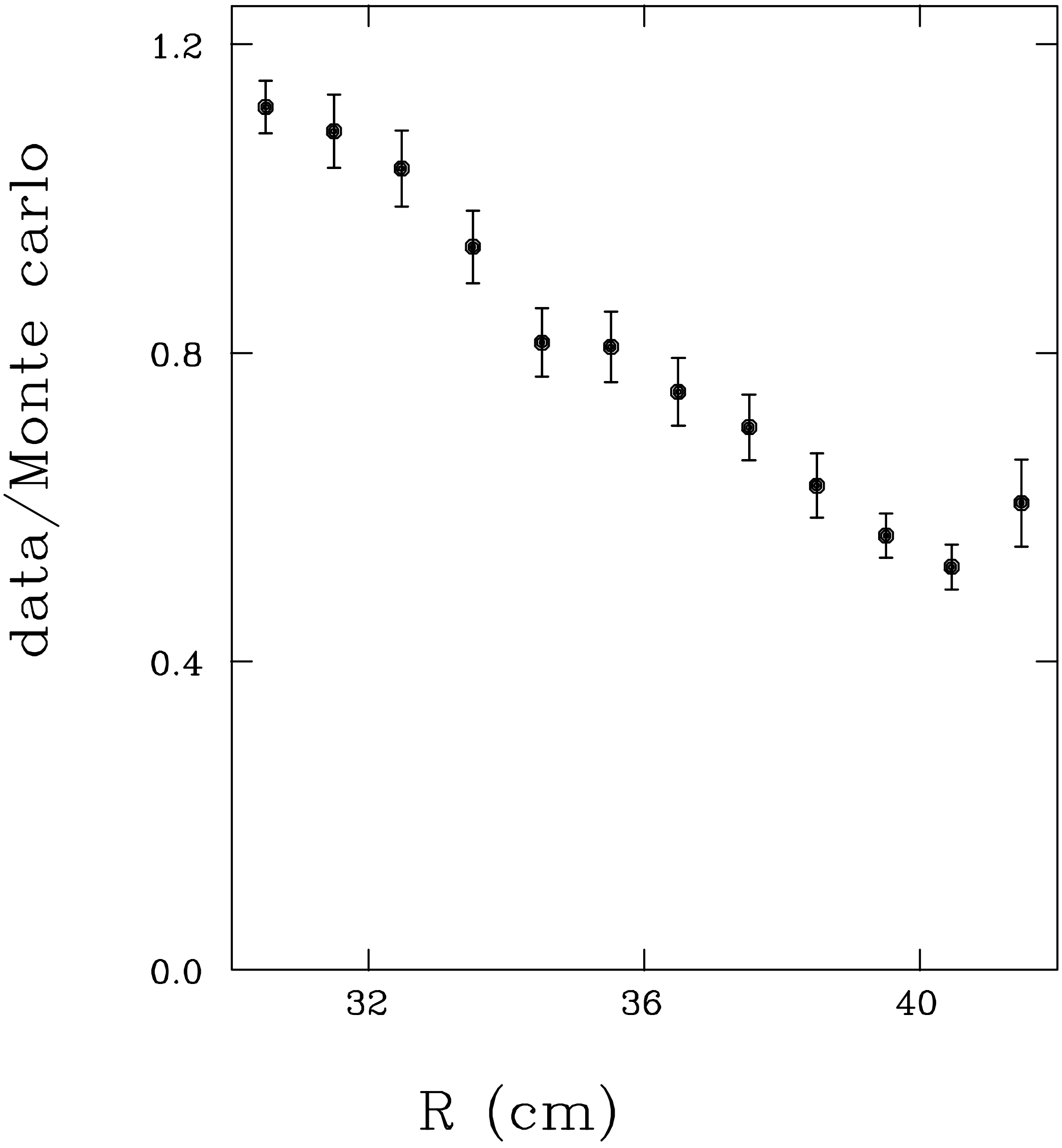

Figure(26): Conversion-finding efficiency as a function of R in SL0; efficiency is defined as the ratio of data to monte carlo rates.

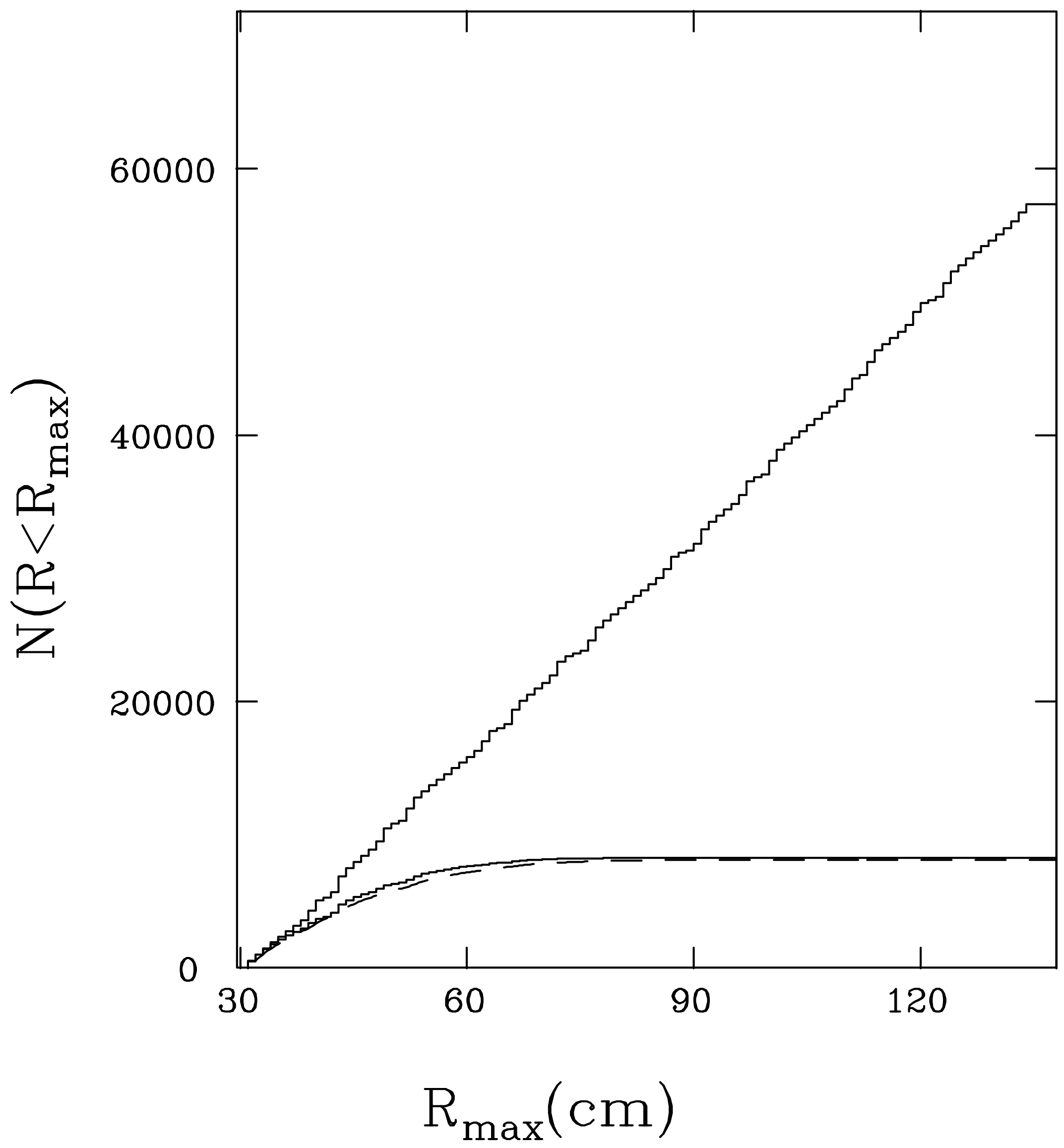

Figure(27): Integral from R=31 to R_{max} for monte carlo simulation (top histogram) and data (bottom solid histogram). Also shown is the same distribution for all conversion candidates before cuts on Sep, $\Delta Cot(\theta)$, and CTC occupancy (dashed curve).

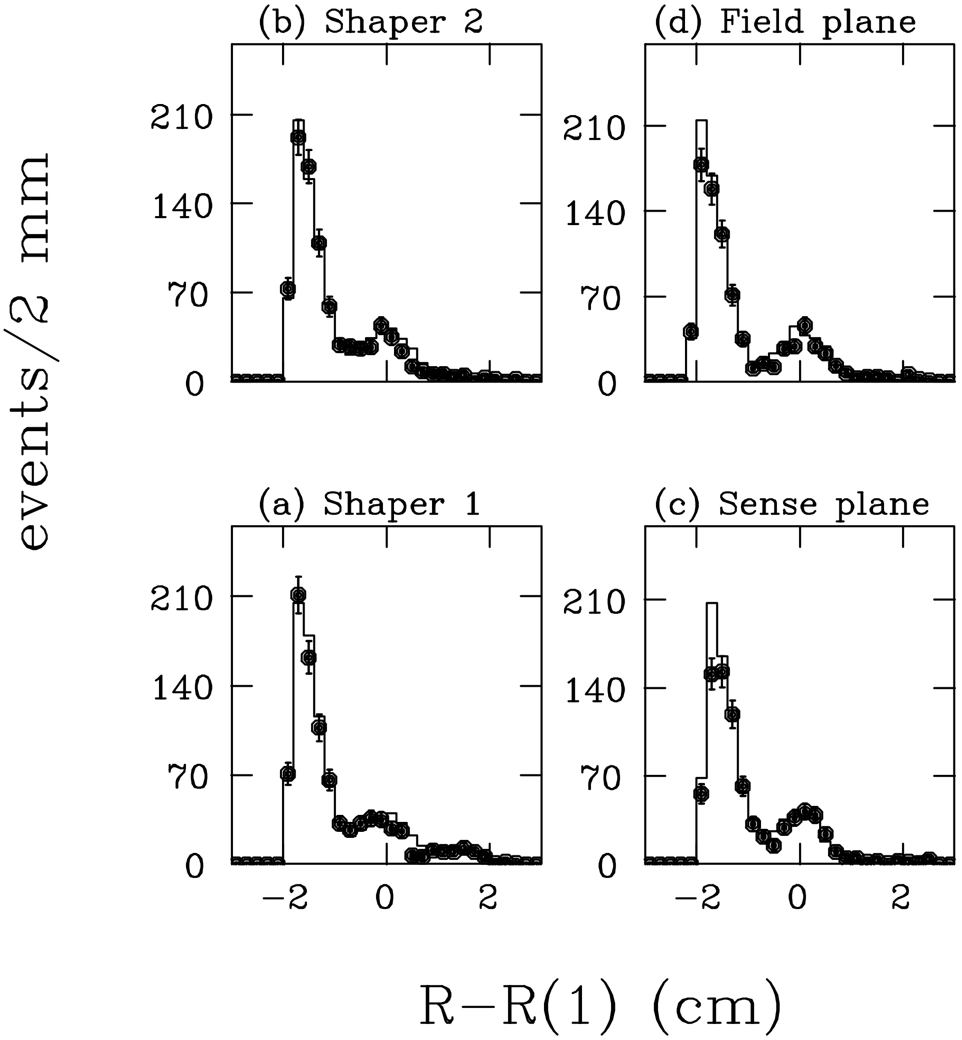

Figure(28): Comparison of data (points) and monte carlo (histogram) distributions in R-R(1), for conversions satisfying a $\pm$ 3 mrad. cut on $\Delta\phi$ for guard wire-1 in the sense, field, and shaper planes.

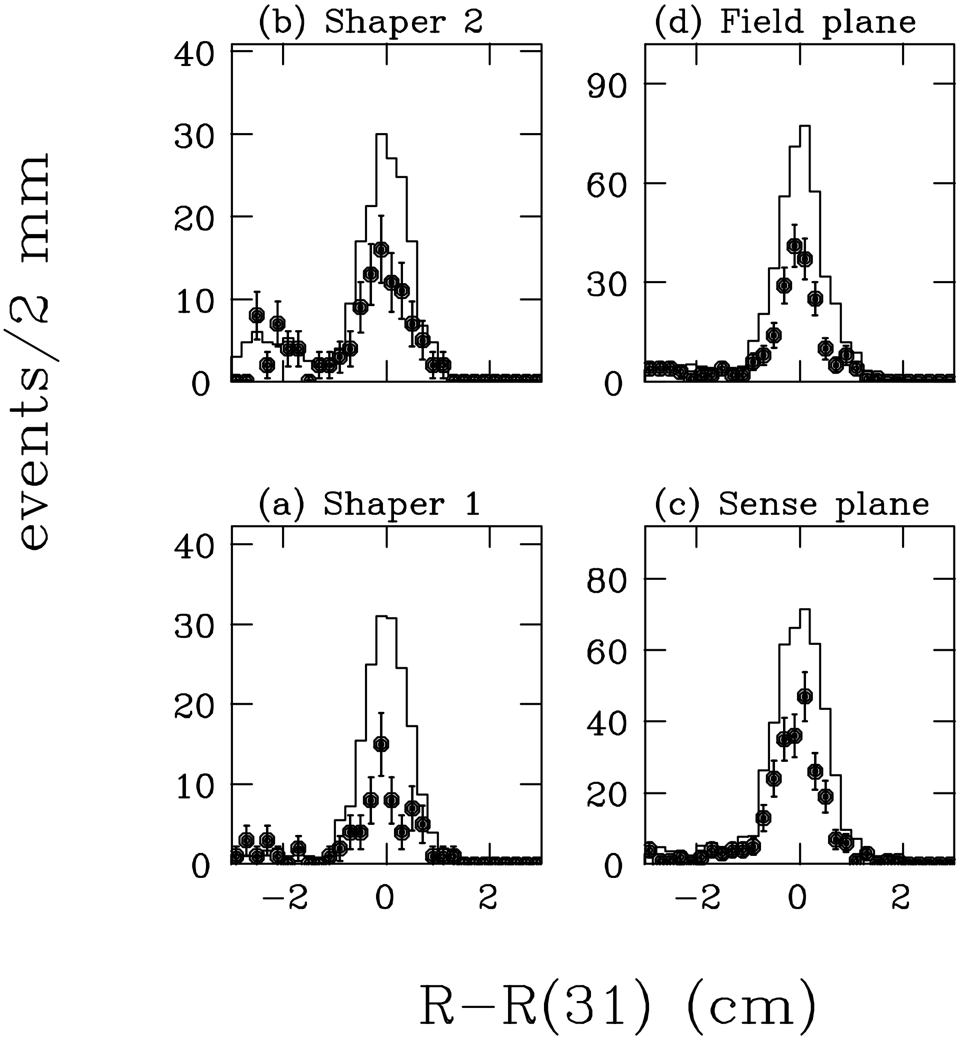

Figure(29): Comparison of data (points) and monte carlo (histogram) distributions in R-R(31), for conversions satisfying a $\pm$ 3 mrad. cut on $\Delta\phi$ for guard wire 31 in the sense, field, and shaper planes.

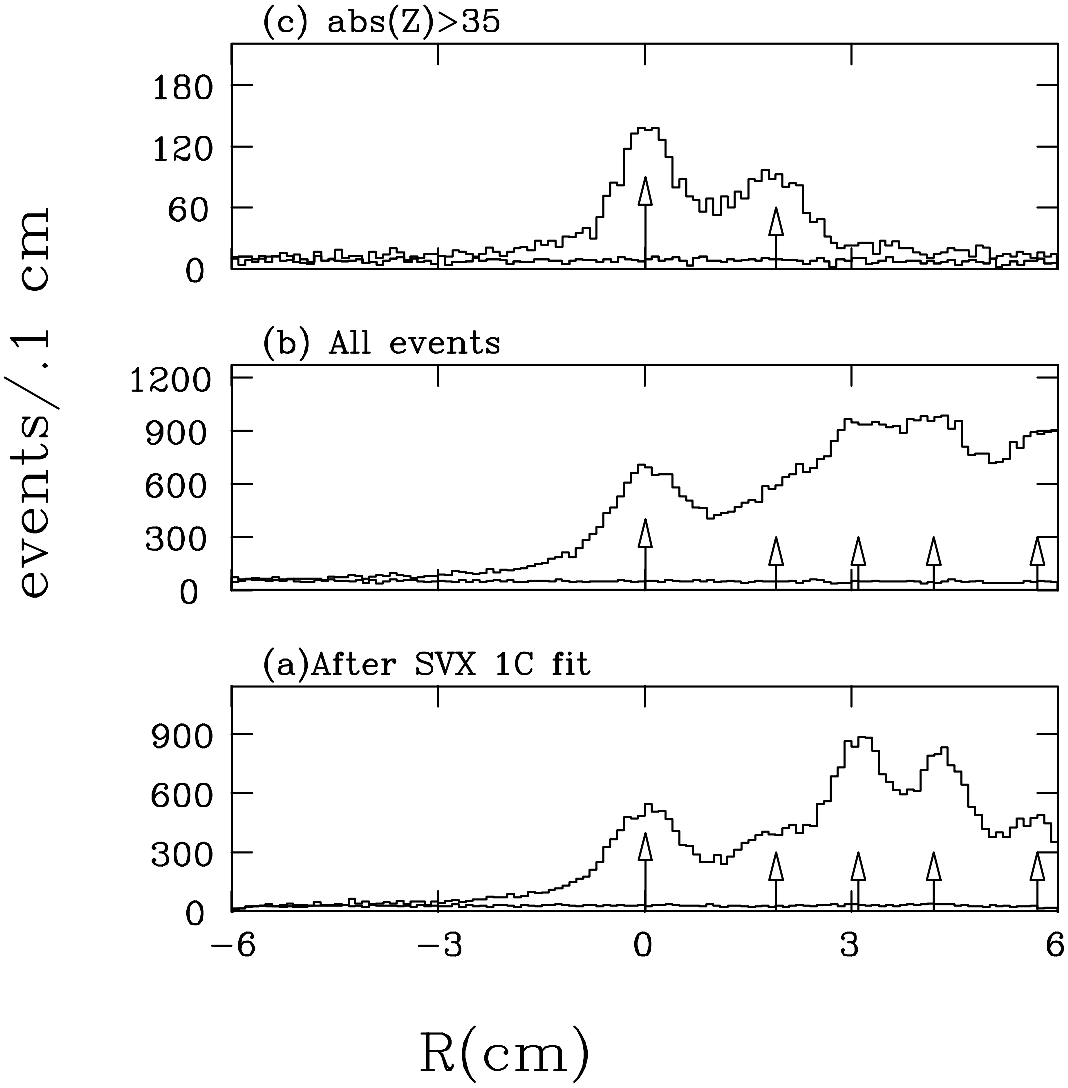

Figure(30a,b,c): Blowup of R-distributions near the origin, after a 1C fit using the SVX impact parameters (a), and using only the CTC track information (b,c). The lower traces show the estimated fake backgrounds. The arrows indicate expected structures: (left to right), Dalitz pairs, beampipe, SVX ladders 0,1,2. To illuminate the beampipe, (c) shows all pairs with abs(Z)$\geq$ 35 cm.

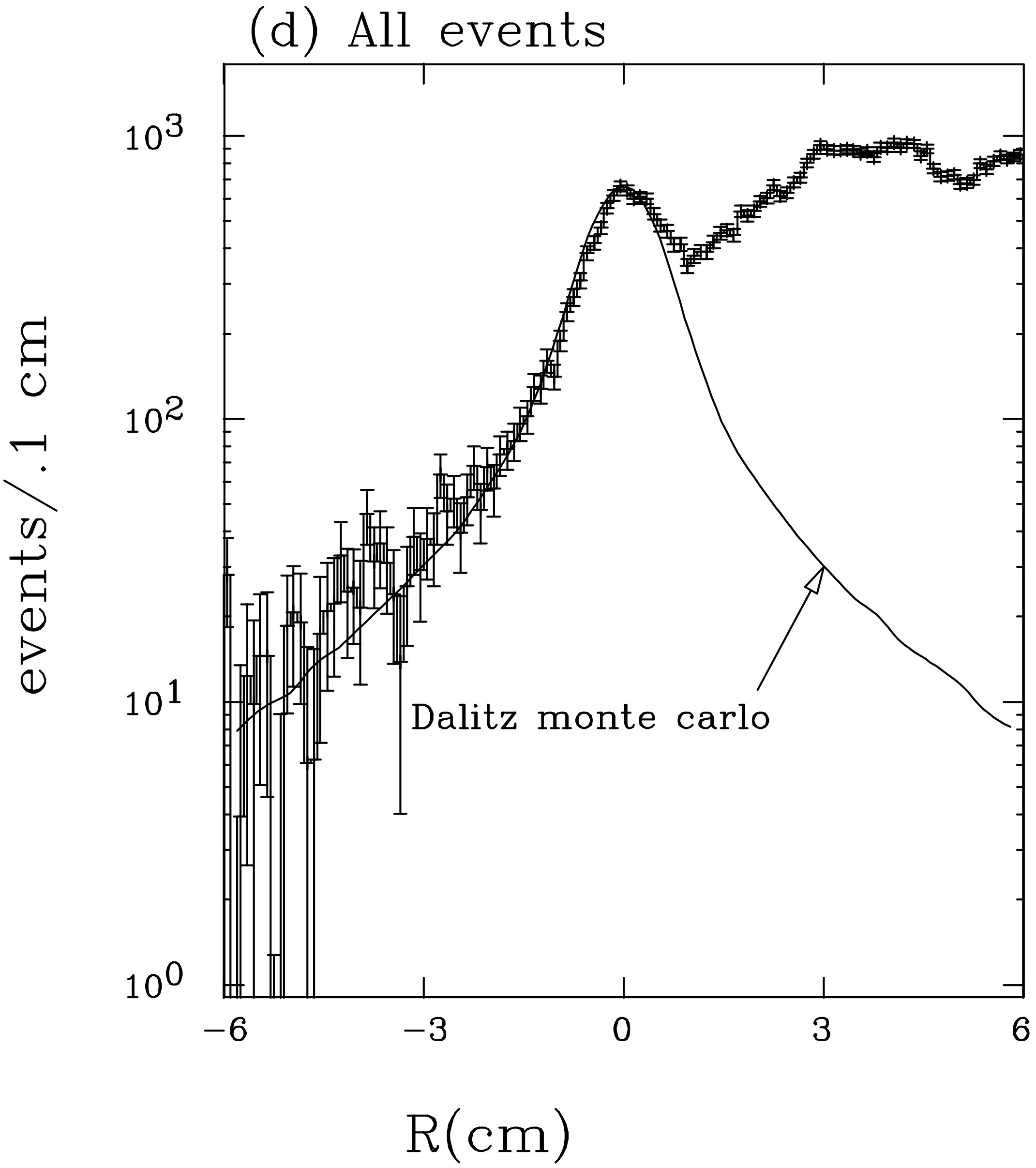

Figure(30d): all CTC track pairs from (30b) on a log scale, after background subtraction, together with a monte carlo prediction for the Dalitz contribution.

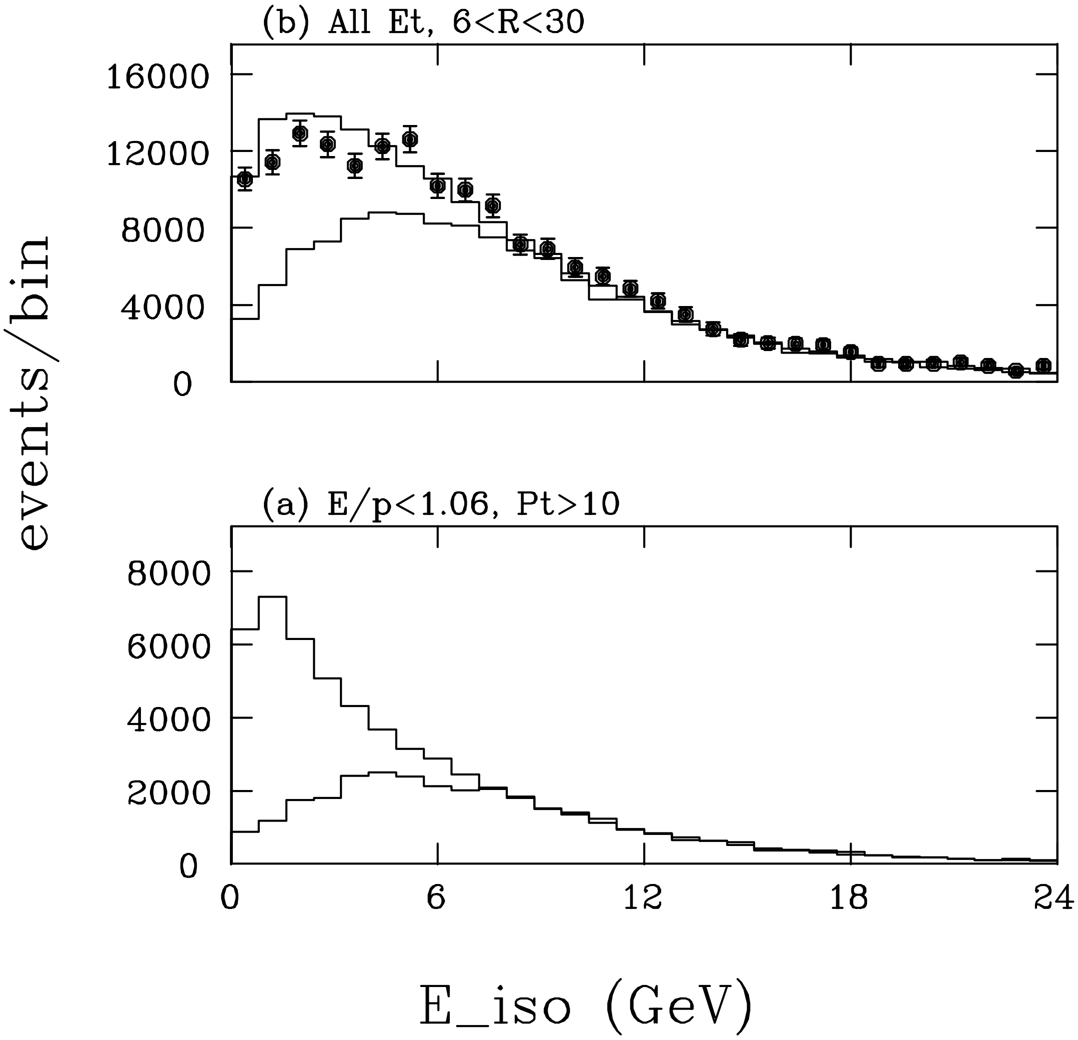

Figure(31): Isolation distributions for all events (upper histogram), and fake conversions (lower histogram), (a) for events with $E/p \leq 1.06$ and $p_T \geq 10$, and (b) all events. The histograms are for conversions in $6 \leq \mathrm{R} \leq 30$ cm; the solid points in (b) are for Dalitz pairs.

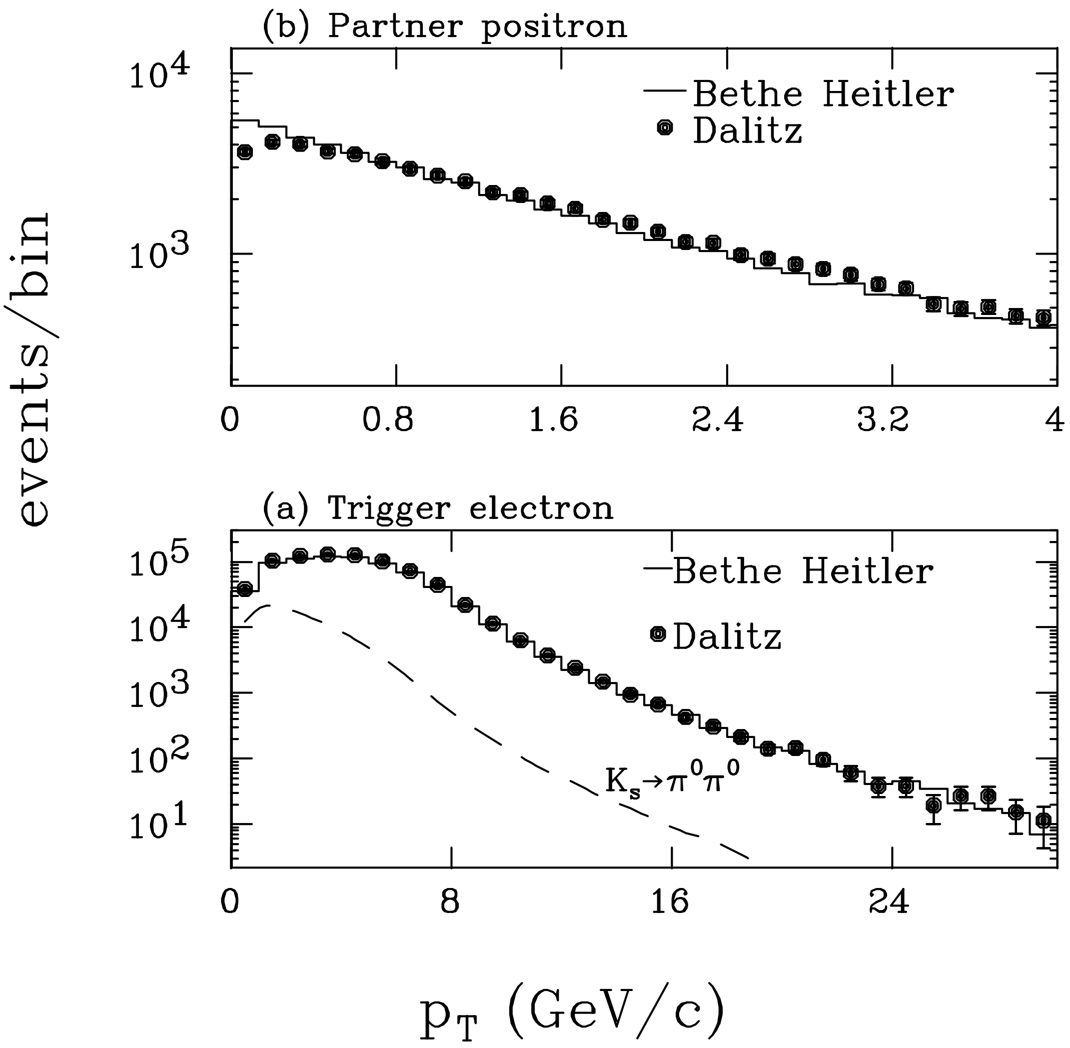

Figure(32): p_T distribution for trigger electron (a), and partner positron (b) from a monte carlo simulation of π^0 production. The points are for Dalitz decays, the histogram for Bethe-Heitler conversions. The dashed line in (a) shows the expected contribution from K_s decays.

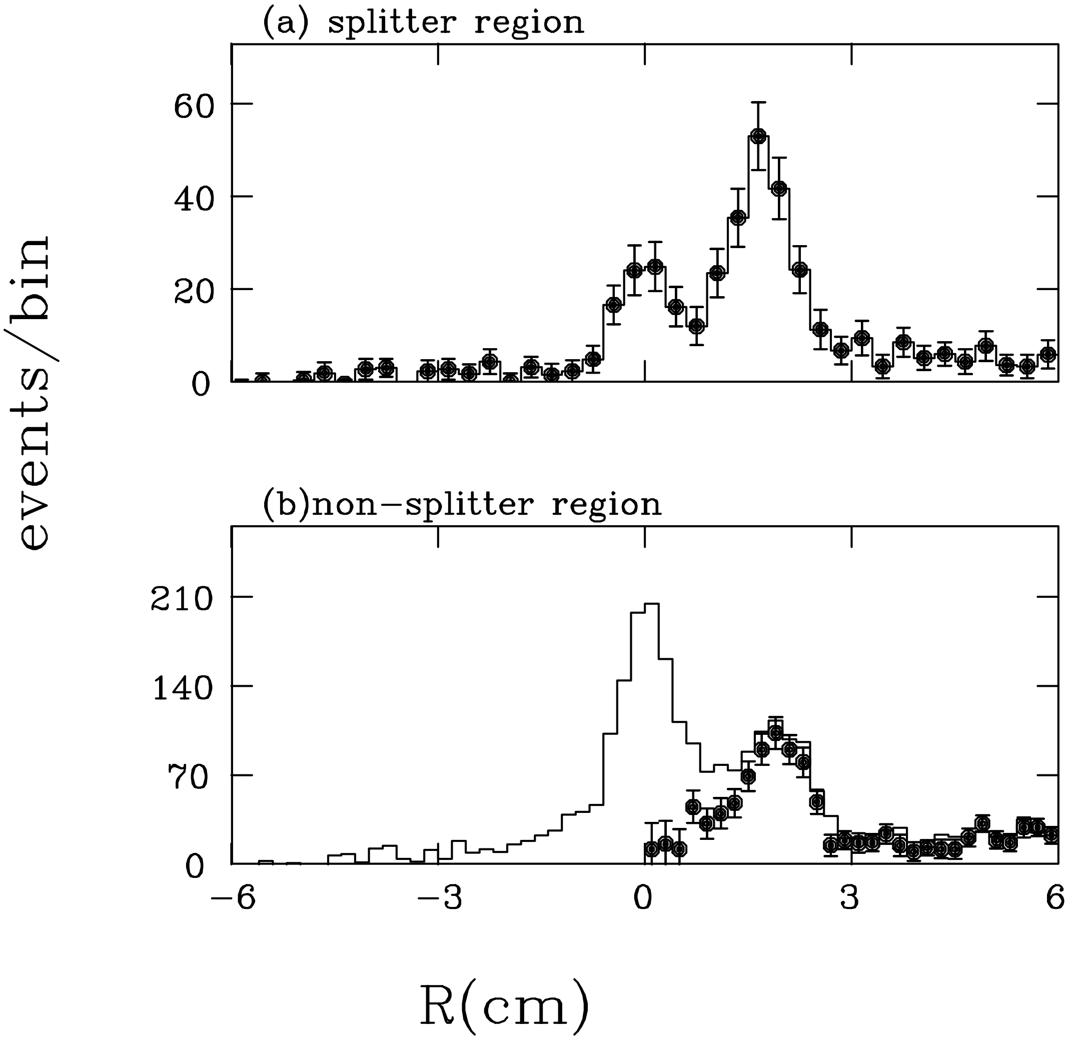

Figure(33): R-distributions for abs(Z)>35 cm., (a) for ϕ=198±17deg ("splitter region"), and (b) ϕ <175,ϕ >221deg; the points in (b) are Dalitz-subtracted, using the R<0 events, folded about R=0.

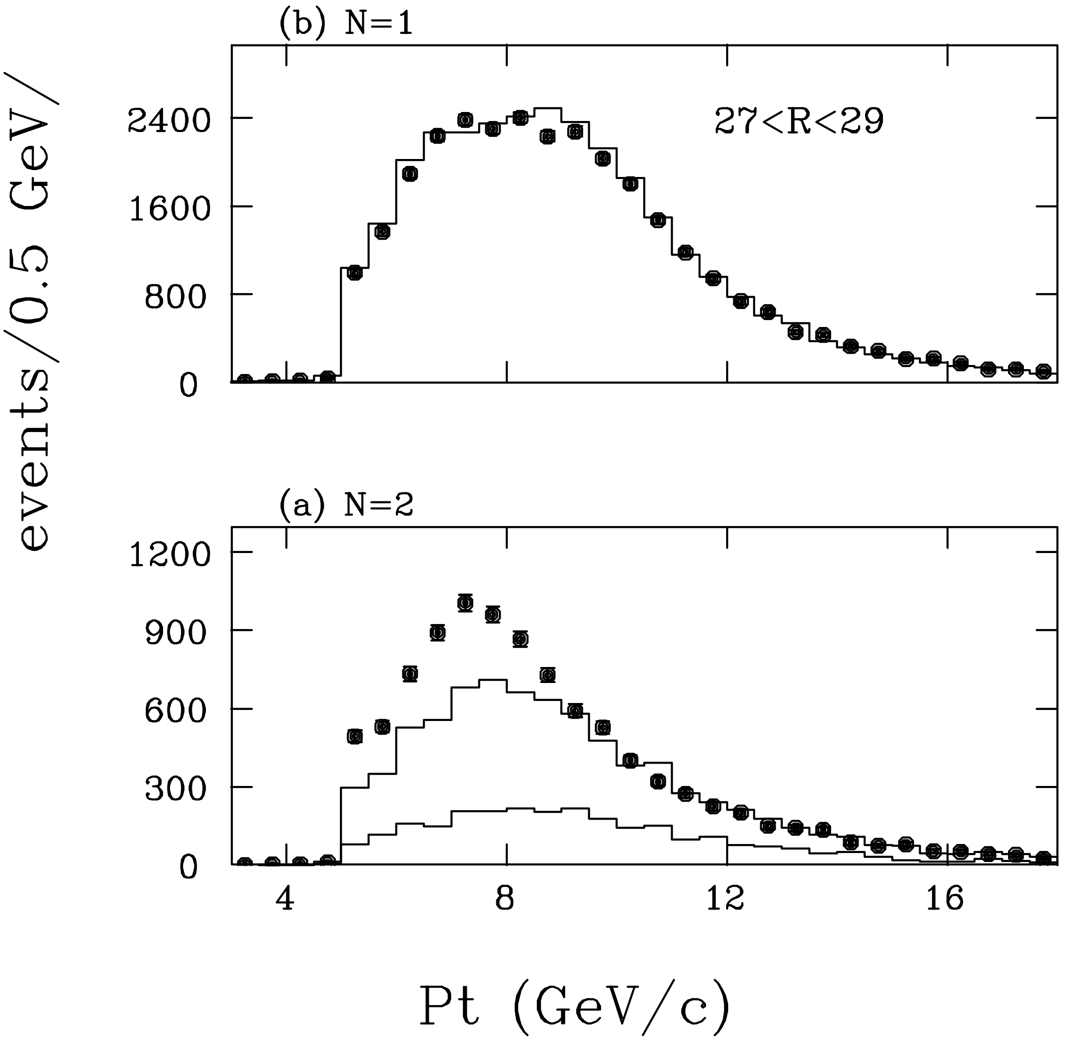

Figure(34): p_T distribution for (a) N=2 and (b) N=1 trigger electrons in the CTC can region (points); the upper histogram is the prediction based on extrapolation of observed rates in the SVX region ($2 \leq R \leq 7$ cm). The lower histogram in (a) is the contribution from N=1 pairs in the SVX that would satisfy N=2 at the CTC can radius.

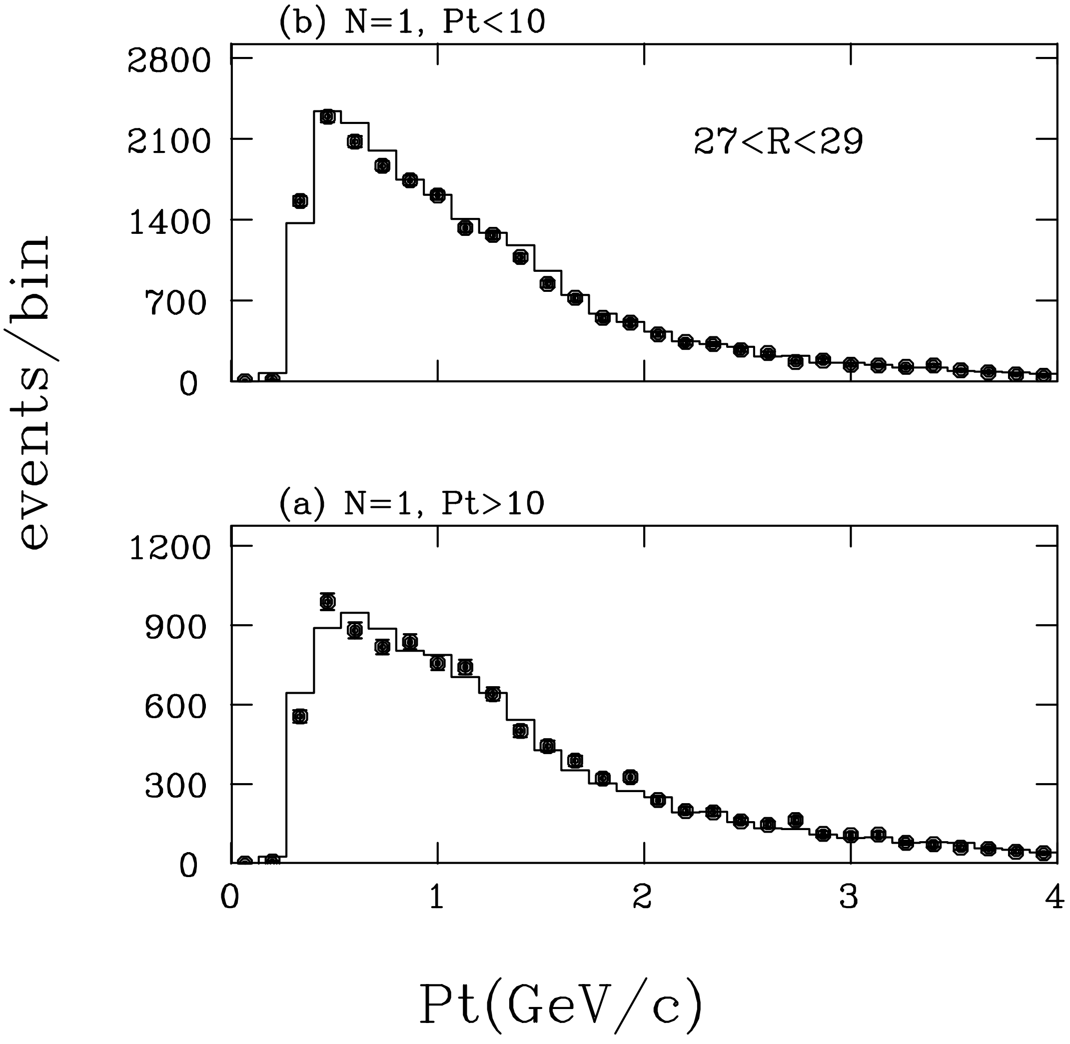

Figure(35): Low p_T partner spectra for N=1 events in the CTC can region, for trigger p_T above (a) and below (b) 10 GeV/c; the histograms are predicted spectra based on extrapolation from observed rates in the SVX region.

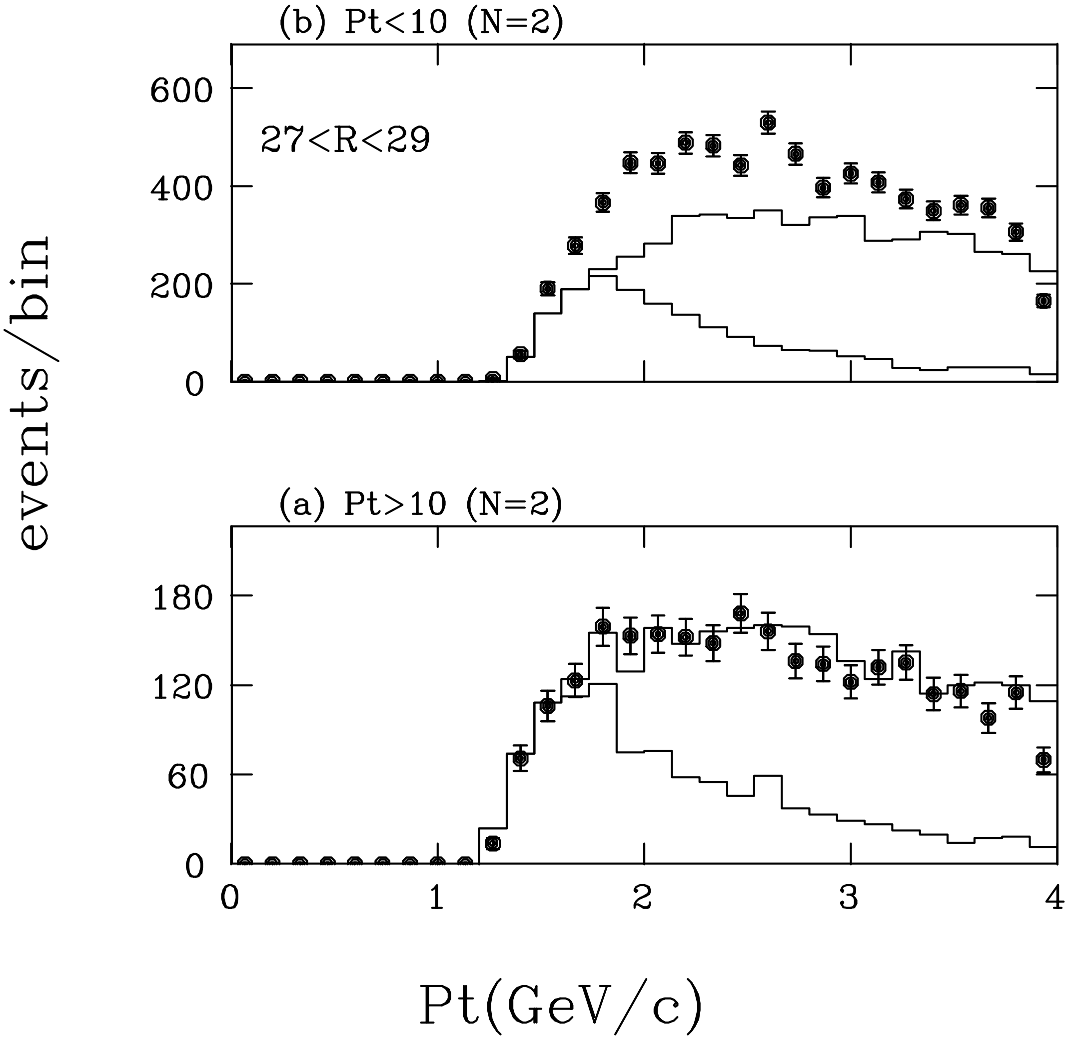

Figure(36): Low p_T partner spectra for N=2 events in the CTC can region, for trigger p_T above (a) and below (b) 10 GeV/c. The upper histograms are predictions from extrapolation of observed rates in the SVX region; the lower histograms are contributions from N=1 pairs in the SVX region.

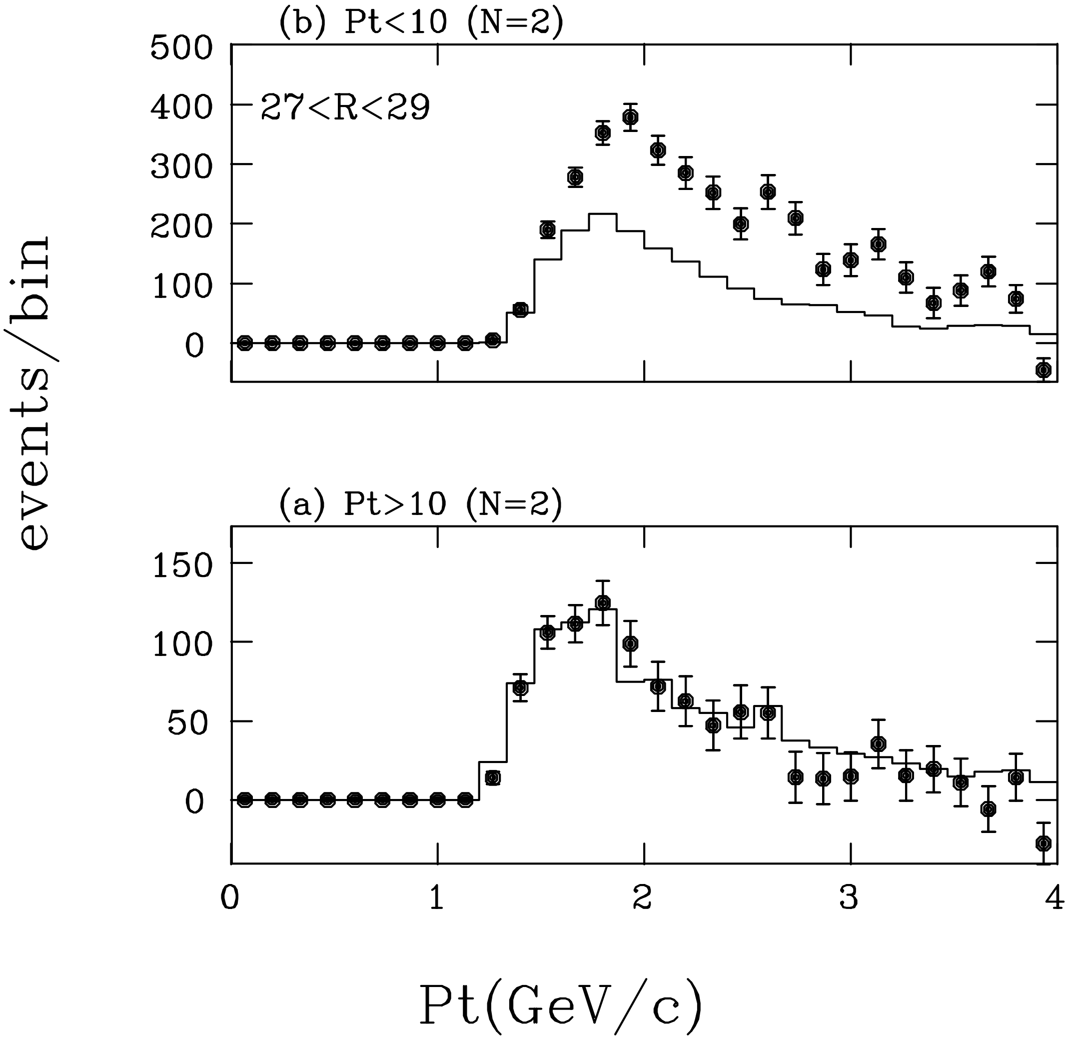

Figure(37): Low p_T partner spectra for N=2 events in the CTC can region, for trigger p_T above (a) and below (b) 10 GeV/c; the predicted contribution from N=2 pairs observed in the SVX region is subtracted. The histogram shows the expected contribution from N=1 pairs in the SVX region that satisfy N=2 at the CTC can radius.

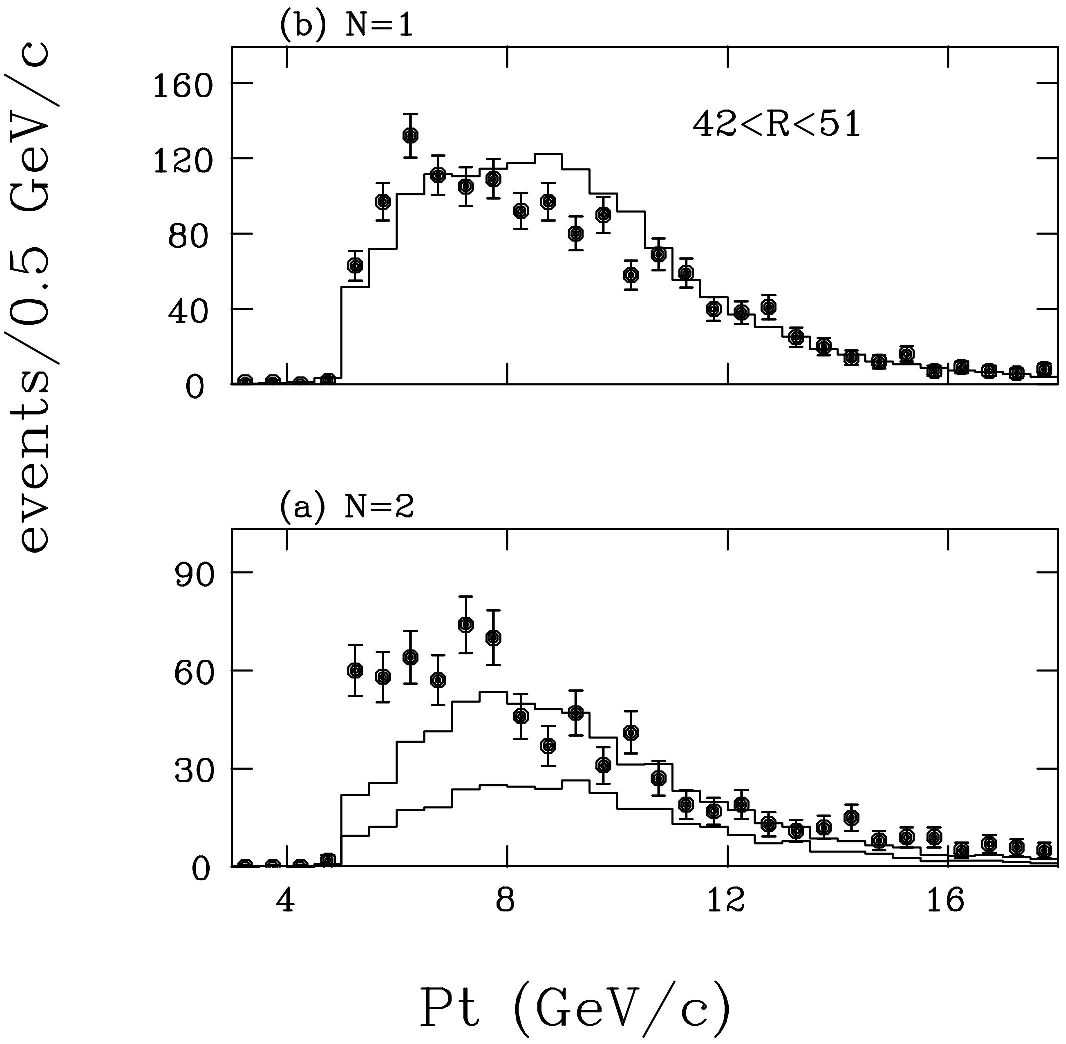

Figure(38): p_T distributions for (a) N=2 and (b) N=1 trigger electrons, for events in SL1 ($42 \leq R \leq 51$ cm.). Histograms are analogous to those in fig. (34).

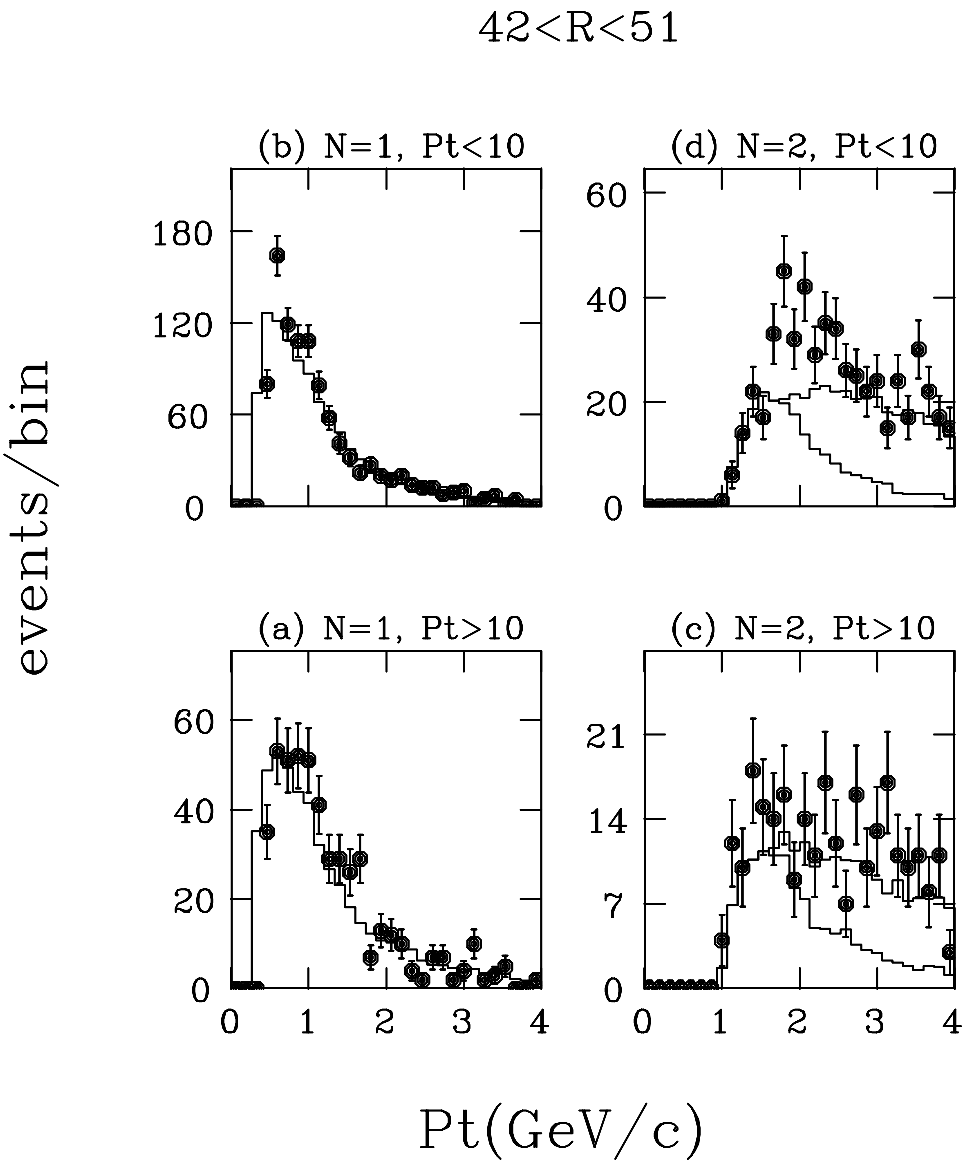

Figure(39): Low-p_T partner distributions for N=1 and N=2, sliced on trigger p_T above (a,c) and below (b,d) 10 GeV/c, for events in SL1. The upper histograms are predictions based on extrapolation from the SVX region; the lower histograms in (c) and (d) are the expected contributions from N=1 pairs in the SVX region that would satisfy N=2 in SL1.

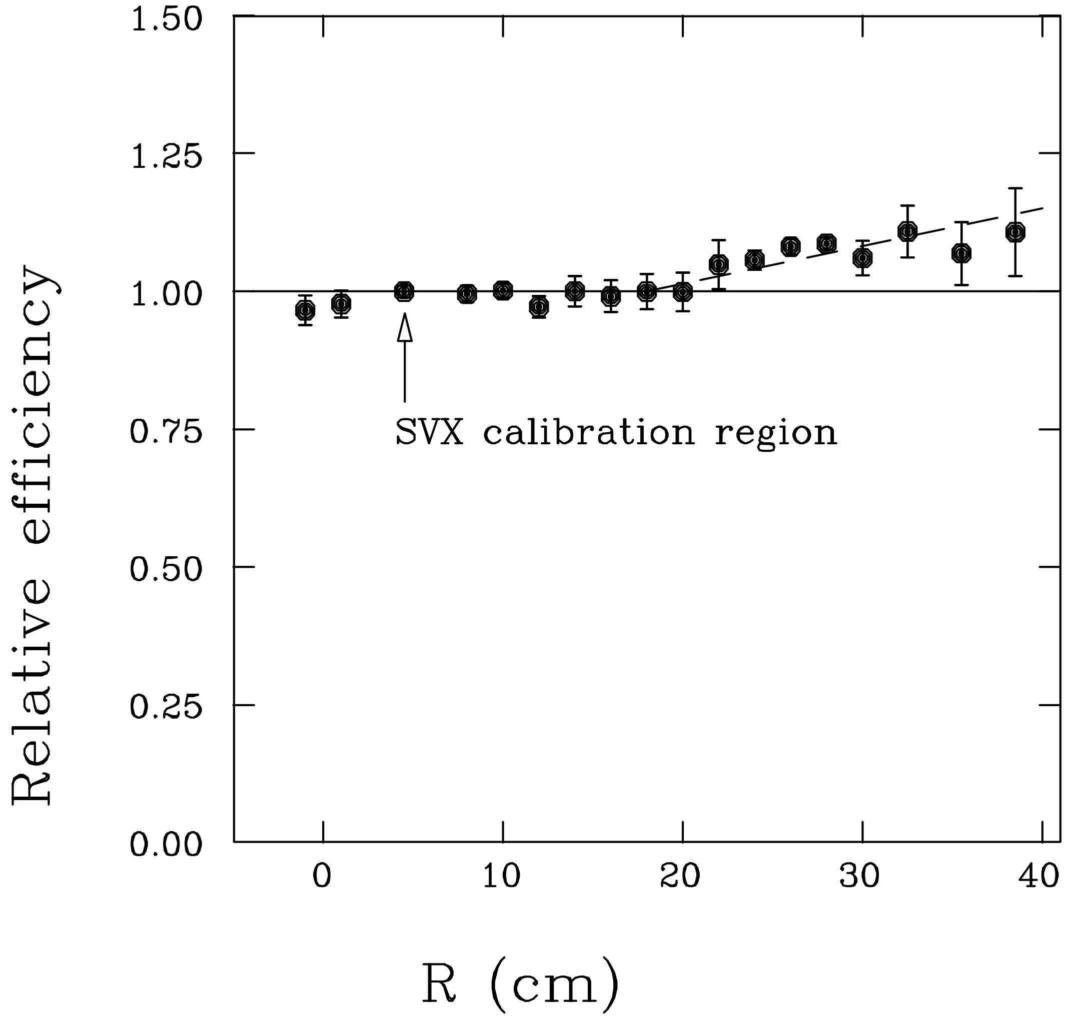

Figure(40): Relative efficiency versus R, based on extrapolation of the observed N=1 and N=2 rates in the SVX region (arrow in figure.) The dashed curve is the *ansatz* used to parametrize efficiency versus R.

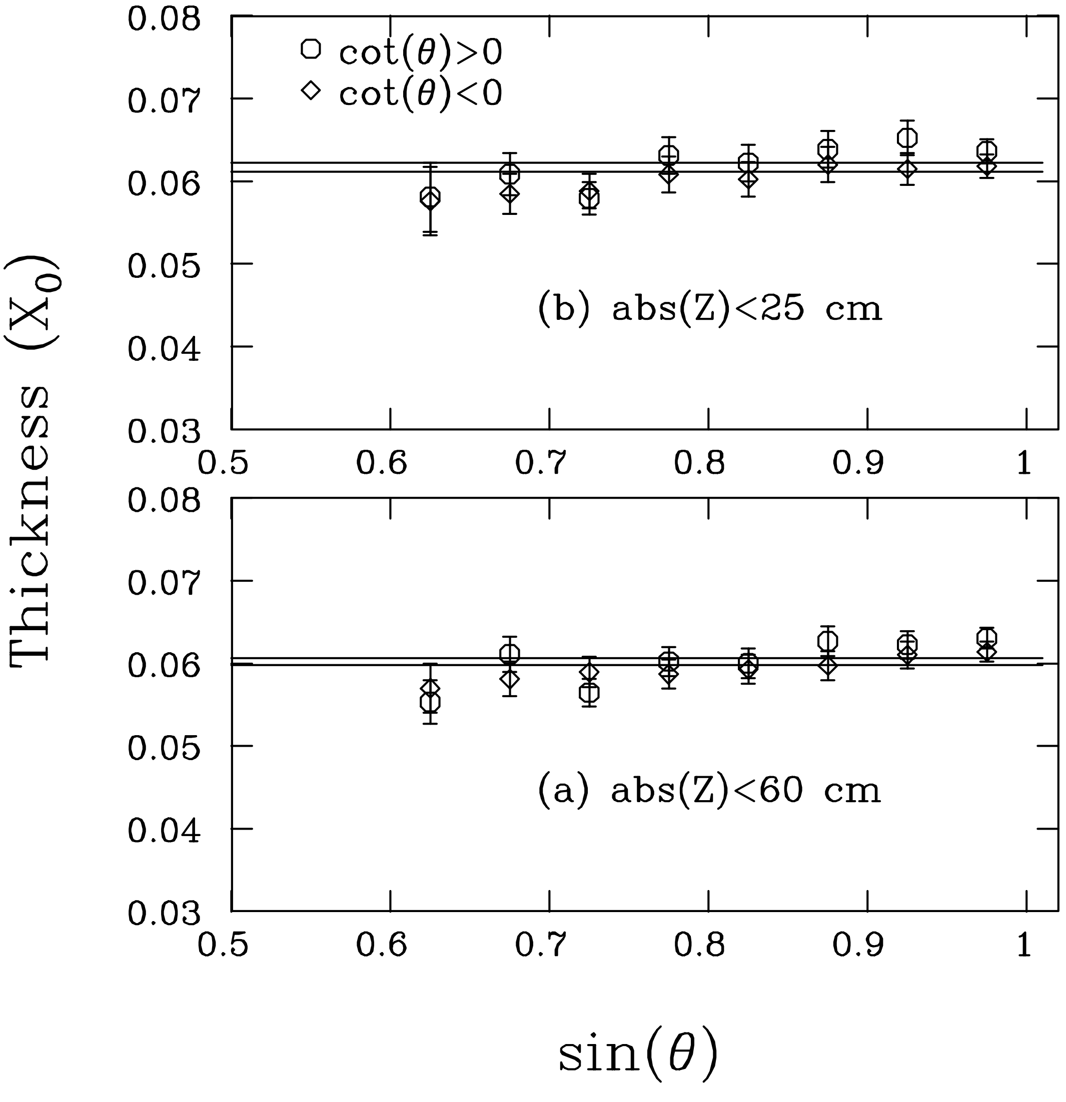

Figure(41): Transverse thickness of external material in R $\leq$ 31 cm, versus $\sin(\theta)$, for two cuts on Z_{vertex}; positive and negative $\cot(\theta)$ are plotted separately, and the overall averages are shown as bands.

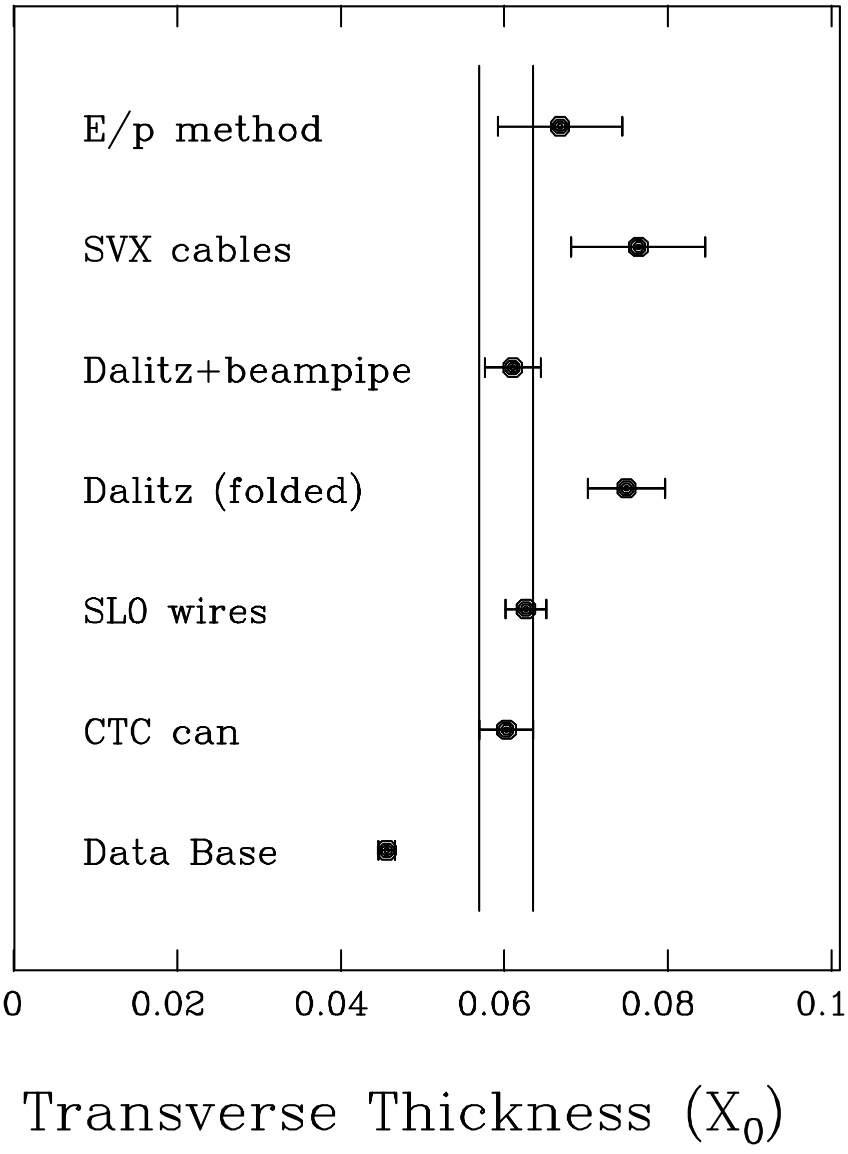

Figure(42): Estimated total tranverse thickness, for R $\leq$ 31 cm., using CTC can, CTC guard wire, SVX cable, folded-Dalitz, and Dalitz plus beampipe calibrations described in the text (corrected for relative efficiencies.) Also shown is the calibration based on the E/p method (scaled by $\sin(\theta)$ and with half of CTC material subtracted), and corresponding estimate from the CDF database.